Hydrologically-driven gravitational instability approached from various objects, time and space scales

Grégory Bièvre

Université Grenoble Alpes

Observatoire des Sciences de l'Univers de Grenoble

Institut des Sciences de la Terre

École Doctorale Sciences de la Terre, de l'Environnement et des Planètes

Mémoire en vue d'obtenir l'

Habilitation à Diriger des Recherches

présenté par

Grégory Bièvre

Hydrologically-driven gravitational instability
approached from various objects, time and space scales

Soutenue publiquement le 13 juin 2022

Jury :

Stéphanie Gautier	Université Montpellier II	Rapportrice
Frédéric Nguyen	Université de Liège	Rapporteur
Myriam Schmutz	Institut Polytechnique de Bordeaux	Rapportrice
Ludovic Bodet	Sorbonne Université	Examinateur
Anne Socquet	Université Grenoble Alpes	Examinatrice

ISTerre
Institut des Sciences de la Terre

OSUG
Observatoire des Sciences de l'Univers de Grenoble

UGA
Université Grenoble Alpes

Table of Contents

1 Introduction

The first tens of metres below the surface present a high degree of heterogeneity and complexity because of the geological history (interaction between the geological bedrock and the quaternary formations including, in places, glacial processes during the last million years) and because of the interaction between varying processes at the atmosphere/subsurface interface, such as weathering, gravitational processes, water flow and infiltration. This is also the scale at which societies interact with the subsurface: infrastructures and land use, resource exploration (mining, water, etc.) or protection. Growing urbanization then requires efficient tools to characterize and monitor natural or anthropogenic structures subject to hazards and to understand the physical mechanisms that affect them. Among the different prospecting tools and compared to geotechnical techniques, geophysical methods offer the advantage of being fast, non-invasive, and integrative from a spatial and volumetric point of view. On one hand, they appear suitable to characterize the subsurface (geometry) and monitor processes operating at depth (e.g. water content). On the other hand, they provide geophysical parameters that are indirectly related to ground properties, and not straightforward for the engineering community. As such, they need to be calibrated using direct observations originating from geotechnical and geological prospecting. The combination of these two approaches allows, in favourable conditions, to image the subsurface in 2D to 4D.

During the past 10 years and combining these two approaches (geophysical methods calibrated with geotechnical measurements), I mainly worked on two distinct objects which might appear far away from each other at first glance, and which are hydrologically-driven slow-moving landslides (SML) and earth dams subject to water leakage leading to internal erosion. However, these structures present similarities such as a high degree of geological, geotechnical, geometrical and topographical complexity, the occurrence of water infiltration leading to the presence of water tables possibly leading to failure. These two kinds of structures receive growing attention from the geotechnical academic community since the late 1960s and geophysical methods were reported relatively soon after (Fig 1.1). However, geophysical methods were in both cases increasingly used starting from the 2000s. This can be linked to technical developments, mainly in computing science which allowed the processing of large amounts of data along with the development of 2D to 4D inversion algorithms (see Jongmans & Garambois, 2007, for landslides).

My research activity during this period concerned the characterization and monitoring of these structures combining geotechnical (in the very broad sense) and geophysical methods. The scientific questions leading my activity were: what is the role of lithological heterogeneity on the control of landslide activity? What is the role of environmental parameters on landslide activity? Are there any geophysical parameters that could image or monitor this variability? Is there any geophysical parameter that could monitor landslide evolution from damaging to failure?

To answer these questions, I adopted a multi-disciplinary approach. It required collaborating with many specialists in various domains such as mineralogy and hydro-geochesmistry (IS-

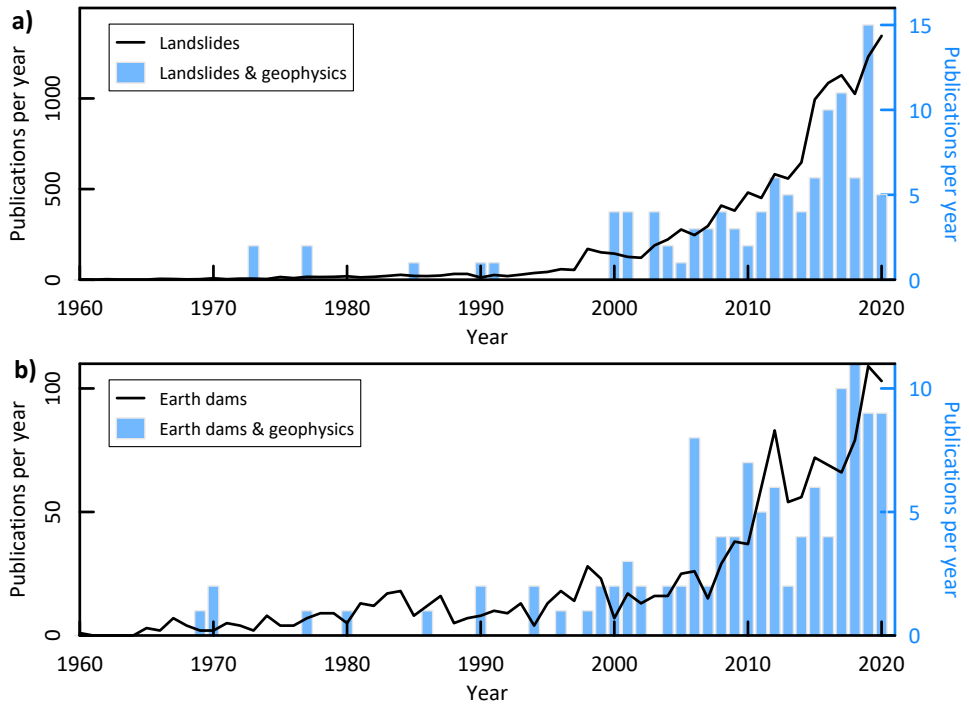

Figure 1.1 – Number of publications in English since 1960 about **a)** landslides and geophysics and **b)** earth dams and geophysics (the susceptibility of earth dams to earthquakes was excluded). Source: web of science, August 2021.

Terre), hydrogeology (Univ. Franche-Comté), soil and fluid mechanics (3S-R Grenoble, INRAe Grenoble, CEREMA Lyon, Notre-Dame University-Louaizé in Lebanon), quaternary geology (ISterre), remote sensing (Univ. Lausanne, ISTerre), subsurface geophysics (ISTerre, Univ. Sophia-Antipolis, INRAe Lyon), seismology (ISTerre), geophysical inversion (LIAG Hanover, Univ. Gustave Eiffel, INRAe Lyon) and numerical modelling (ISTerre, IGE Grenoble). As it can be seen, I developed most of my collaborations with specialists/teams located at Université Grenoble Alpes.

I developed a multi-scale approach, from the micro-scale up to several millions of m^3 (Fig 1.2). My approach also encompasses a multi-temporal perspective, notably in the case of landslides. This mainly originates from my education as a geologist where the history of the supporting ground upon which natural or anthropogenic structures rely has to be considered for achieving a good understanding of the geotechnical context. I adopted this naturalistic ground-structure interaction approach in my career as an engineer for earth dam (Bièvre & Norgeot, 2005) or linear infrastructure studies (e.g. roads ; Bièvre, 2007a).

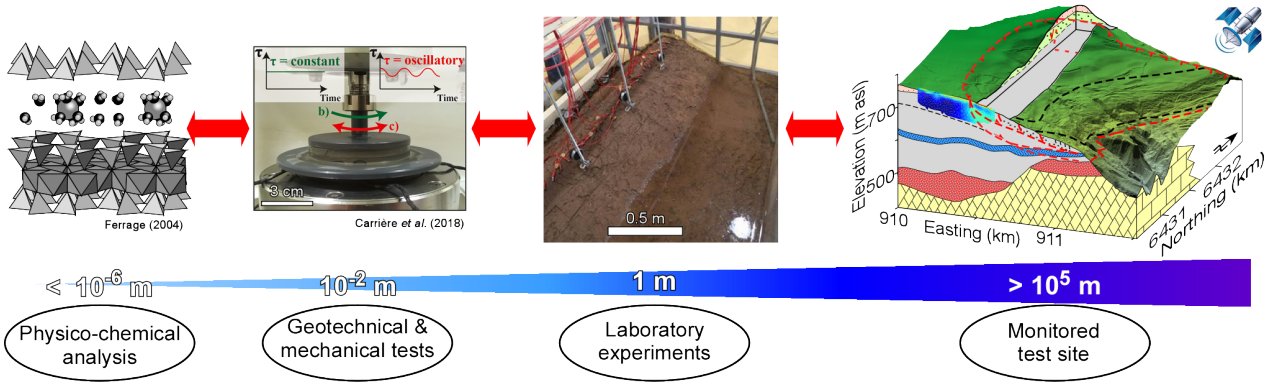

Figure 1.2 – Illustration of the different spatial scales adopted, from the micro-scale to the field scale through centimetre and metre scales.

The results presented in this manuscript were partially obtained through 3 PhD thesis (Carrière, 2016; Fiolleau, 2020; Maalouf, 2021), several Master internships and thanks to numerous local or national grants. This manuscript is a compilation and synthesis of 12 research papers for which I was either leading or actively participating, and which I consider as interesting contributions. I also chose not to expose some works I was involved in, which concern landslides (Arosio *et al.*, 2019; Colombero *et al.*, 2021) or earth dams (Fargier *et al.*, 2019), but for which I was not a leader. Some complementary and non-exposed works present original results about the combination of geophysical techniques and other methods, with application to the pre-Inca city of Tiwanaku (Vella *et al.*, in prep), the localization of forgotten municipal waste landfills (Bièvre *et al.*, in prep), or the imaging of an Oxfordian carbonate platform in Burgundy, France (Jorry & Bièvre, 2011).

The manuscript is organized in several chapters. The first chapter introduces the context of this manuscript and the scientific activity I conducted during the past ten years. Chapter two is devoted to hydrologically-driven slow-moving landslides and chapter three to earth dams subject to water leakage and internal erosion. Each of these two chapters is divided into two parts: first, a synthesis of my achievements is presented, and, second, some research perspectives are drawn for the next years. General conclusions and perspectives are drawn in chapter four.

2 Slow-moving landslides

2.1 Introduction

Most of my work dealing with gravitational instability concerns hydrologically-driven slow-moving landslides (SML). I recently co-authored a review paper that will be used in the following to describe these structures (Lacroix *et al.*, 2020b, and references herein). An excerpt from a paper in preparation (Jongmans *et al.*, in prep.) will also be used. Slow-moving landslides move downslope for months to decades (or even centuries to millenniums) at rates ranging from millimetres to several metres per year. As such, they rarely claim lives and offer the possibility to study in detail mechanisms affecting and controlling landslide evolution. However, SML can sometimes evolve into catastrophic failures with motions up to several m/s, causing widespread destruction and casualties. Slow-moving landslides occur in large numbers across the world in areas that typically have mechanically weak, clay-rich soil and rock, and high seasonal precipitation. Slow-moving landslides exhibit non-uniform spatial and temporal kinematic changes and tend to be deep-seated (> 3 m thick) with a complex subsurface hydrological system.

The parameters that influence slope stability are derived from equations originating from critical-state soil mechanics with a Mohr-Coulomb failure criterion (Terzaghi *et al.*, 1996). This criterion states that failure, or motion, will occur when the combination of shear and normal stresses acting on any point of a material reaches a threshold value that is controlled by some material properties (for example, cohesion and angle of internal friction). Stability is generally described with a factor of safety (FoS), which is calculated as the ratio between the resisting forces (shear strength τ_f) and the driving forces (shear stress τ) acting on a shear plane at the bottom interface between the landslide mass and the stable material. Stability is expected when $\mathrm{FoS} > 1$, whereas instability occurs when $\mathrm{FoS} < 1$. When $\mathrm{FoS} = 1$, stability is at the limit equilibrium. Landslide forcings act to decrease the FoS and either trigger the initial failure or induce the acceleration of already failed slopes.

A variety of internal and external factors are known to drive landslide dynamics (Fig 2.1), resulting in changes in the mechanical properties of the material and/or landslide acceleration or collapse. Internal and external forcings include upslope loading of the landslide from deposition of new material, changes in groundwater from rainfall or snowmelt, changes in the water level within lakes, reservoirs and rivers, particularly during impoundments, shaking from earthquakes, deforestation and debuttressing of the landslide toe from river erosion, man-made infrastructure or glacier retreat.

In the case of hydrologically-driven SML, hydrologically-induced strength changes primarily occur because of variations in pore-water pressure and, correspondingly, effective normal stress. As such, strength changes depend on the water-saturation level of the hillslope material. For example, when the material is not fully saturated, suction forces from capillary effects and clay swelling in the lateral shear surfaces can increase shear strength and help stabilize a hillslope. However, when the material is nearly or fully saturated, an increase in pore-water

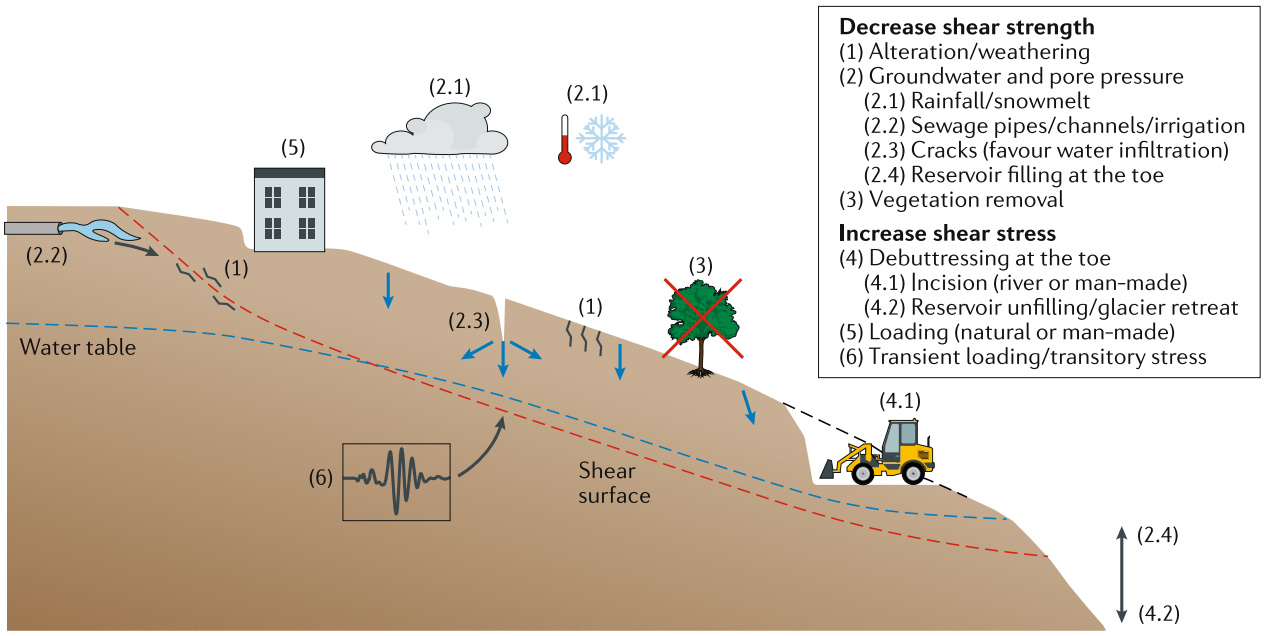

Figure 2.1 – Slow-Moving Landslide cross-section and forcing mechanisms (Lacroix *et al.*, 2020b).

pressure induces a loss of cohesion, along with a decrease of the effective normal stress and, consequently, causes a reduction in the shear strength of the landslide material (possibly leading to liquefaction). The magnitude of the resulting variations in shear strength depends on the drainage conditions of the slope. If the slope has "drained" conditions, water can flow out of the landslide mass before excess pore-water pressures develop. The opposite is true for "undrained" conditions, where a rapid increase of stress owing to a specific loading such as water infiltration, with respect to the time required for the water to be drained, in loose, nearly saturated fine-grained formations leads to the build-up of excess pore-water pressure and, subsequently, to a dramatic decrease of the effective normal stress.

The infiltration of water into a hillslope can have several origins (Fig 2.1). Rainfall and snowmelt and anthropogenic irrigation can infiltrate through the hillslope matrix (Fig 2.2a) or preferential flow paths, such as fissures and cracks generated by the landslide activity. Variations in atmospheric pressure, for example, atmospheric tides, can also cause vertical migration of the groundwater within the landslide. At the Slumgullion landslide, USA, daily variations in atmospheric pressure of less than 1 kPa lead to variations in landslide velocity from less than 1 mm.day^{-1} (higher atmospheric pressure) to more than 2-3 mm.day^{-1} (lower atmospheric pressure). Changes in the water level of a lake or reservoir (natural or man-made) at the hillslope toe can also generate variations in the groundwater levels within the landslide body and, therefore, impact landslide kinematics (Fig 2.2b).

The relationships between rainfall and/or snowmelt and landslide acceleration have been documented in many regions worldwide and indicate that the highest velocities are generally observed during periods of intense or long-lasting rainfall (such as wet seasons, monsoons and/or summer storms) and during periods of high snowmelt discharge (winter to spring). For example, the Slumgullion landslide, USA, attains its maximum velocities of $\sim$ 10 m.year^{-1} (170 % the average annual rate) during peak snowmelt. Furthermore, the Maca landslide, Peru, accommodates 90 % of its 1-10 m annual displacements within the five months of the rainy season. In the same way, but with a much lower magnitude, the Charlaix landslide, French western Alps, has slide velocities of 13-16 cm.year^{-1} from November to March and 0-2.5 cm.year^{-1} from April to October (this will be exposed in section 2.2.2.1). The direct relationship between rainfall and/or

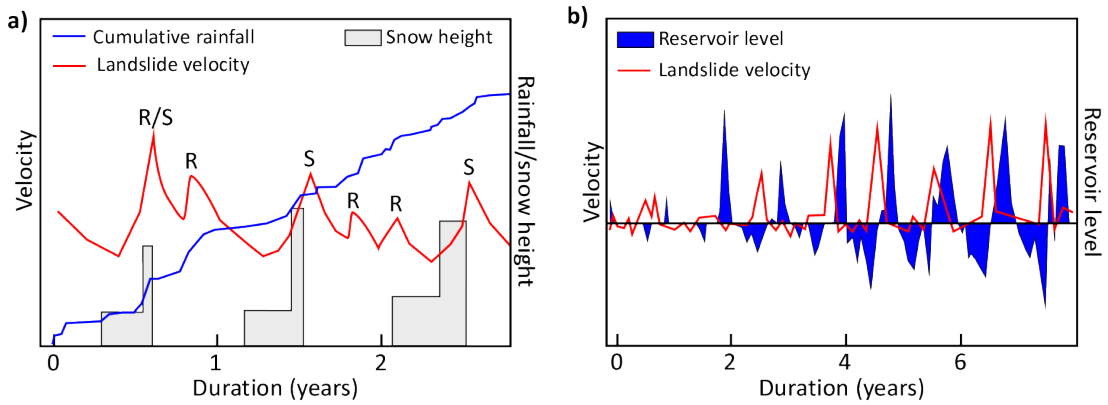

Figure 2.2 – Possible hydrological forcings for driving landslide acceleration (modified from Lacroix *et al.*, 2020b). **a)** Variations in pore pressure driven by rainfall and/or snowmelt (Coe *et al.*, 2003). R refers to rainfall forcing, S to snowmelt forcing and R/S to mixed forcings. **b)** Reservoir filling, which can also lead to variations in pore pressure (Zhou *et al.*, 2016).

snowmelt-induced water infiltration and landslide occurrence and acceleration led to the proposal of early-warning systems for shallow (generally no more than a few metres), catastrophic landslides based on regional-specific rainfall intensity and duration thresholds (e.g. Keefer *et al.*, 1987; Aleotti, 2004; Krøgli *et al.*, 2018). However, rainfall-based early-warning systems are not appropriate for deep-seated (thickness > 3 m), slow-moving landslides, owing to the increased complexity of their subsurface hydrological network relative to shallow catastrophic landslides (for which the early-warning systems were designed)

Water infiltration can also originate from man-made operations, such as irrigation for large-scale agriculture or personal use and from sewage and drainage systems (Fig 2.1). For instance, massive irrigation for farming in the desert of Tacama, South Peru, led to the reactivation of huge slow-moving landslides in the two distinct valleys of Siguas and Vitor (Lacroix *et al.*, 2020a). In the arid environment of the Tacama desert, a 20-year delay between the onset of irrigation and the initiation of landslide was observed, which was interpreted as the time needed to develop high pore-water pressures. Ultimately, migration of the Punillo Sur landslide generated displacements of ~ 300 m in 30 yr.

The complex processes explaining the transformation of initially rigid sliding blocks into flow-type movements, such as mudflows or earthflows, are still the subject of debate and research (Iverson, 2005; Van Asch *et al.*, 2009; Mainsant *et al.*, 2012a; Iverson & George, 2016; Berti *et al.*, 2018; Carrière *et al.*, 2018b). Two main rheological approaches are usually used to explain the solid-fluid transition usually in case of rainfall and/or snow melting. The elastoplastic two-phase approach considers that water infiltration induces a temporary increase in pore water pressure and reduces the frictional forces τ_f, likely to generate phases of acceleration (Fig 2.3a ; Picarelli *et al.*, 2004; Iverson, 2005; Iverson & George, 2016). In this case, earthflows remain in a plastic state even during a rapid motion (Keefer & Johnson, 1983; Coe *et al.*, 2003) and the flow-like behaviour results from the deformation along multiple internal shear surfaces (Fig 2.3b ; Iverson, 2005; Hungr *et al.*, 2014). The viscoplastic approach assumes that mass fluidization occurs when the shear stress exceeds a critical stress threshold τ_c depending on the water content (Fig 2.3c ; Mainsant *et al.*, 2012a; Carrière *et al.*, 2018b). The elastoplastic approach is applied for frictional material while the viscoplastic approach appears well suited to cohesive materials with a high water content (Coussot & Ancey, 1999; Ancey, 2007).

Using the classical Mohr-Coulomb failure criterion, the FoS of a homogeneous subsurface of length b (m) sliding along an inclined plane can be expressed as :

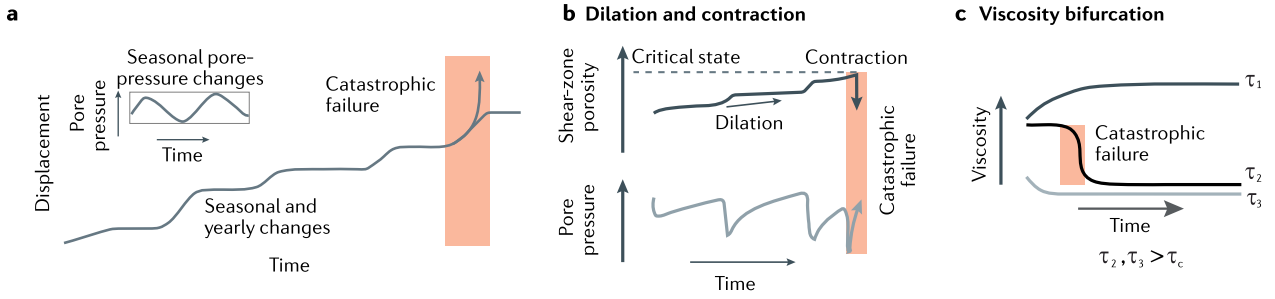

Figure 2.3 – Schematics of landslide displacement and their associated mechanisms during the transition from slow to fast motion (Lacroix *et al.*, 2020b). **a)** Time series of complex yearly and seasonal displacement and a transition to catastrophic failure. Inset shows an example of the precipitation-induced pore-water-pressure changes that drive the seasonal landslide motion. **b)** Dilatant strengthening and contraction weakening, represented by the shear-zone porosity and pore-water-pressure changes that result in slip events. Catastrophic failure occurs at the critical state line. **c)** Viscosity bifurcation time series, which displays a rapid reduction in viscosity when the stress exceeds the critical value τ_c. In all figures, the orange box highlights the transition from slow motion to catastrophic failure.

$$FoS = \frac{\tau_f}{\tau} = \frac{c' \cdot \dfrac{b}{\cos\alpha} + (W \cdot \cos\alpha - \dfrac{u \cdot b}{\cos\alpha}) \tan\varphi'}{W \cdot \sin\alpha} \tag{2.1}$$

where C' and φ' are the effective cohesion (Pa) and internal friction angle (°), respectively, α is the angle between the normal and tangential stress (°), W is the weight (N) and u is the pore pressure (Pa). Geotechnical techniques allow the determination of these parameters, which are necessary for landslide characterization and stability assessment. However, geophysical methods are also able to provide some of the required observations, such as the geometrical characteristics (surface extent, depth to the shear surface, lithological boundaries, etc.) and the pore pressure through the depth to the water table.

The pioneering application of surface geophysical techniques to landslide investigation dates back to the 1970s (Bogoslovsky & Ogilvy, 1973; Brooke, 1973; Bogoslovsky & Ogilvy, 1977). Subsequently, 1D investigations were conducted, especially in the French Alps (Caris & Van Asch, 1991) and also, more particularly, in the glaciolacustrine clays of the Trièves area (Antoine *et al.*, 1981; Giraud *et al.*, 1981). However, it was not until the early 2000s that emerged 2D, 3D and then 4D geophysical imaging techniques, which were then applied to landslides (see references in Jongmans & Garambois, 2007; Whiteley *et al.*, 2019) .

In Grenoble, this research theme was initiated in the mid-2000s by D Jongmans and S Garambois (Jongmans & Garambois, 2007). At that time, I was working in a "Laboratoire Régional des Ponts & Chaussées" as a geotechnical technician/engineer and was wishing to carry on with a PhD thesis in geophysics. This emerging theme of geophysical methods applied to landslides was then natural for a PhD topic. Thus, my thesis took place within the framework of the creation of an observatory on clayey landslides (MOUVARGI, 2006-2009), thanks to fundings from IFSTTAR and CETE de Lyon. This observatory was labelled by the CNRS in 2009 and then integrated into a National Observation Service (SNO in French) in 2009: the Multidisciplinary Observatory of Versant Instabilities (OMIV ; ano-omiv.cnrs.fr). This observatory aims at monitoring continusously several parameters (at least seismology, geodesy and hydrometeorology) with free access to the data. This observatory historically encompasses four sites in France: two rocky landslides (Séchilienne and La Clapière) and two landslides in clays/soft rocks (Super-Sauze and Avignonet). Since 2011, I am the scientific head of the Avignonet/Harmalière site (a few hundred metres East of Sinard in Fig 2.4) within this SNO. I am also working on other landslides, such as the Charlaix landslide located in similar Quaternary glacio-lacustrine clays

(CH in Fig 2.4, close to the city of La Mure) and the Pont-Bourquin landslide in the Valais Alps in Switzerland (PBL in Fig 2.4).

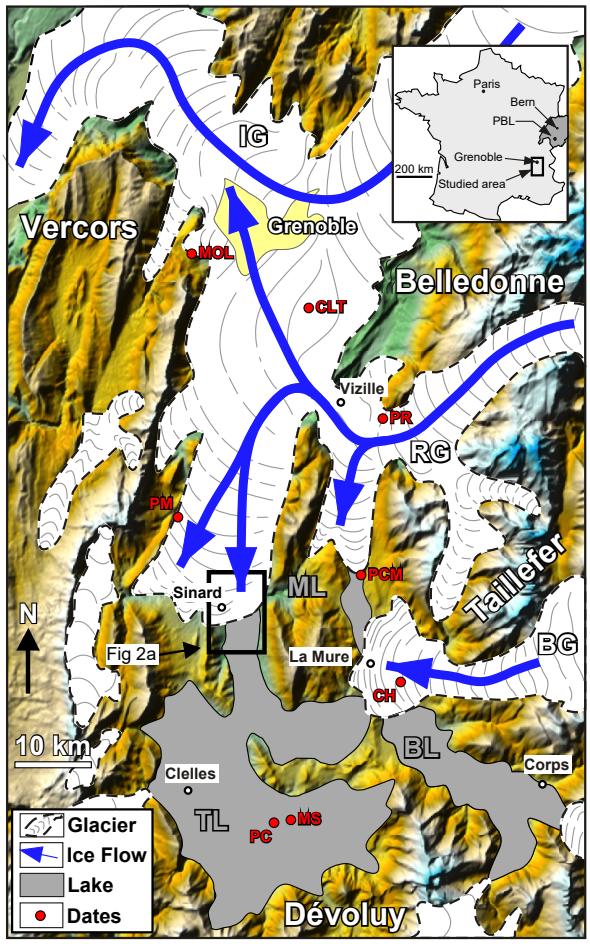

Figure 2.4 – Location of the Avignonet and Harmalière landslides and palaeogeographic situation during the Last Glacial Maximum (Bièvre & Crouzet, 2021, redrawn from Monjuvent, 1973 with ice flow from Coutterand, 2010). IG: Isère Glacier; RG: Romanche Glacier; BG: Bonne Glacier; TL: Trièves Lake; BL: Beaumont Lake; MOL: Mousterian lithics; CLT: Crey alluvial terrace; PR: polished rock; PM: Prélenfrey moraine; PCM: Pierre-Châtel moraine; CH: Charlaix laminated clays; MS: mollusc shells. The Pont-Bourquin landslide (PBL) is located in the insert.

2.2 Achievements

2.2.1 The role of lithological heterogeneity on the control of landslide activity

Although the role of lithology on landslide kinematics has been regularly pointed out at the watershed scale (among others Petley *et al.*, 2005; Corsini *et al.*, 2005; Coe *et al.*, 2009; Bièvre *et al.*, 2011; Travelletti *et al.*, 2013; Guerriero *et al.*, 2014), it has rarely been documented over a specific landslide. This section investigates the influence of lithological heterogeneity on the differential evolution of deformation observed in the Avignonet landslide. It is first evaluated at the scale of the whole landslide by combining geophysical, geodetic, remote sensing and hydrological data (section 2.2.1.1). Second, a focus is made on the southern part of the Avignonet landslide where numerous boreholes were available (section 2.2.1.2). Datings also allowed to evaluate the potential activity of the landslide since the last deglaciation a few tens of thousand years ago.

Landslides in the Trièves and Beaumont areas correspond to slow-moving landslides (Hungr *et al.*, 2014) with sliding velocities ranging between a few mm/yr to several tens of cm/yr. Velocity is higher between November and April, highlighting a precipitation-driven control (Van Asch *et al.*, 1996, 2009; Bièvre *et al.*, 2018b). These landslides generally correspond to earthslides with retrogression mechanisms at the headscarp (Hungr *et al.*, 2014). Some of them can evolve suddenly into earthflows, as it happened to the Harmalière landslide (H in Fig 2.5) in March 1981 and late June 2016, with measured displacements up to 50 m in 1 month (Lacroix *et al.*, 2018). From a granulometric point of view, the so-called laminated clays are clayey silts and exhibit a porosity $\phi \approx 40\,\%$. The phreatic water table is generally shallow (a few m deep, depending on the season) and the natural volumetric water content $\theta \approx$ 30-35 % (corresponding gravimetric water content $w \approx 20\,\%$) is close to the average Atterberg Liquid Limit LL of $\approx 40\,\%$ (Carrière *et al.*, 2018b). The laminated clays also have a narrow plasticity index $IP \approx$ 15-17 %, which explains the propensity of these landslides to accelerate and possibly turn into earthflows during rainy and snowy seasons. The landslides present several shear surfaces located at depths of generally 5 m, 10-15 m and 40-50 m (Jongmans *et al.*, 2009).

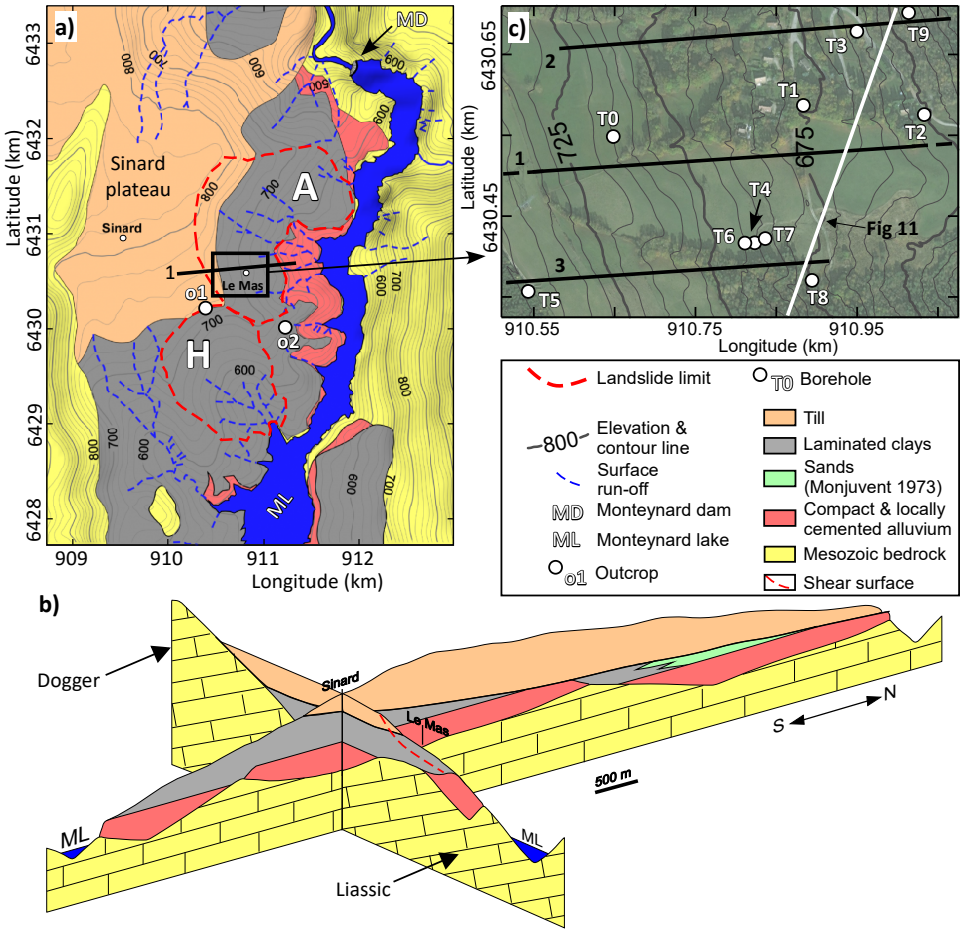

Figure 2.5 – Presentation of the study area (Bièvre & Crouzet, 2021). **a)** Geological map and location of the Avignonet (A) and Harmalière (H) landslides. MO: moraines; LC: laminated clays; S: sands; CA: compact alluvium; MB: Mesozoic bedrock. Map modified from Bièvre *et al.* (2016). **b)** Fence diagram showing the geometrical arrangement of the quaternary units. Red line : erosive surface. Geological cross-sections redrawn from Monjuvent (1978). **c)** Close-up on the southern part of the Avignonet landslide with the location of the boreholes.

2.2.1.1 The role of hydrogeological heterogeneity on landslide differential evolution

The combined interpretation of geodetic, morphological, electrical prospecting and hydrogeological data has brought new insight into the hydromechanical mechanism of the large clayey Avignonet landslide, which was thought to develop mainly in lacustrine laminated clays. 36 geodetic stations were measured twice a year between 1995 and 2005. Two permanent Global Navigation Satellite System (GNSS) stations were installed in 2007 within the frame of the OMIV observatory. Average annual horizontal velocities and associated standard deviations were calculated at these 38 geodetic stations. These punctual velocities were interpolated to produce a velocity contour map (Fig 2.6a). The figure indicates a predominant eastward motion, associated with an increase in velocity, from 0-1 cm/yr at the top of the landslide to more than 10 cm/yr in its lower part. A southward increase in velocity is also visible in the lower part of the landslide where an active zone with a velocity higher than 10 cm/yr was detected (Bièvre *et al.*, 2012).

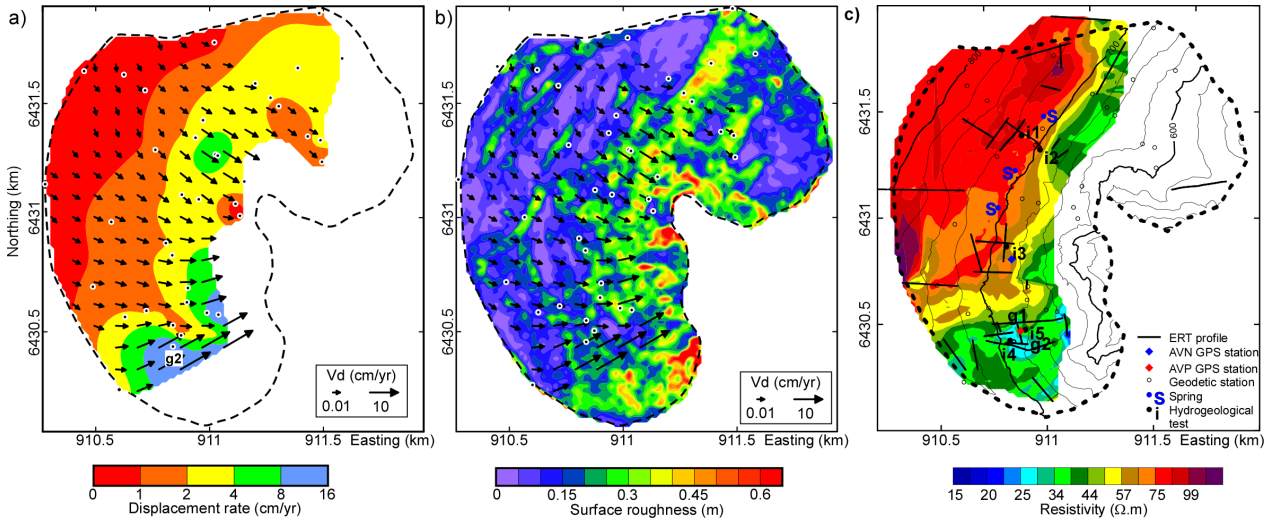

Figure 2.6 – Kinematics, morphological and geophysical analysis of the Avignonet landslide (modified from Bièvre *et al.*, 2016). **a)** Interpolated map of the horizontal mean annual velocity values derived from 38 geodetic stations (dots). Red rectangle: see text for details. **b)** Surface roughness map obtained from a LiDAR DTM acquired in 2006 (Knieß *et al.*, 2014). **c)** Resistivity at 10-m depth over the Avignonet landslide. The Resistivity map is underlain by topographic contour lines in black (one contour line each 25 m). The location of the ERT profiles is indicated.

Surface roughness, which represents the degree of elevation variation within an area, has been mapped from a 2 m-resolution Light Detection and Ranging (LiDAR) Digital Terrain Model (DTM ; where buildings and vegetation were removed) acquired in 2006 (Knieß *et al.*, 2014). The surface roughness map of the landslide (Fig 2.6b) shows that the roughness is generally low (< 0.2 m) in the upper (western) part of the landslide, except along some hectometre-size scarps, and is higher (from 0.25 to 0.6 m) in the lower part of the landslide and the gullies carved in the compact alluvium around the lake. Comparison of roughness and slide velocity maps indicate that, at first order, the higher the velocity, the higher the roughness. The performing of 31 2D electrical profiles, over several years and in varying seasons, all across the landslide and the interpolation of the resistivity at 10 m depth (to avoid seasonal variations ; Fig 2.7c) has detected the presence of a thick resistive ($> 75\,\Omega$.m) layer in its north-western more elevated part. This layer covers one-third of the landslide surface and overlies the laminated clays (15-50 Ω.m) at an elevation of about 700 m asl. This resistive layer was interpreted by Bièvre *et al.* (2016) as the lower part of the moraines capping the Sinard plateau, which could then be 50 m thicker than previously thought. Recent findings on the site (Bièvre & Crouzet, 2021) and the comparable Charlaix landslide (Bièvre *et al.*, 2018b), however, tend to interpret this layer as

coarse lacustrine deposits rather than till. Nevertheless, these coarse sediments (47 % silts and clays) have a higher hydraulic conductivity (hydrological test i1 in Fig 2.7 left with a saturated infiltration rate SIR of 1×10^{-4} m/s) than the underlying laminated clays (65 % silts and clays ; test i2 in Fig 2.7 left with a saturated infiltration rate of 3×10^{-6} m/s). They constitute an aquifer, as attested by the presence of several springs aligned along the lithological contact (S in Fig 2.6c). For tests i4 and i5, infiltration curves (Fig 2.7a) are curved, suggesting a double permeability (at the scales of both the matrix and the fissures) which prevents the determination of the hydraulic conductivity. SIR values of 4×10^{-5} m/s and 4×10^{6} m/s (4×10^{-5} m/s and 1×10^{-5} m/s) were computed at i4 (i5) for short and long times, respectively. These values are relatively high, particularly at site i5, where nearly 92 % of the soil is made of silts and clays. This apparent discrepancy probably results from the presence of numerous superficial fissures in this active zone (Bièvre *et al.*, 2012), which have increased the infiltration rates. Short-term higher values of SIR then probably correspond to the fissure permeability, while the long-term lower ones reflect water infiltration through both the fissures and the soil matrix.

Figure 2.7b presents the horizontal slide velocity measured at the geodetic stations as a function of gridded resistivity with a log-log scale. Horizontal error bars correspond to the 5.8 % RRMSE associated with the resistivity gridding process, while vertical error bars show the standard deviations of mean annual horizontal velocities, reflecting the seasonal and pluriannual velocity variations. Figure 2.7b shows that slide velocities regularly decrease as resistivity increases. The fitting of an exponential relationship (of the form $V_d = Ae^{B\rho}$; black dashed line in Fig 2.7b) gave the parameters A = 342 and B = -0.043. The coefficient of determination is 0.82. Although slide velocities are also controlled by other factors such as the geometry of the slip surface and the topography, the forces acting on the slide (among others the effect of pore pressure) and the geotechnical parameters (cohesion and friction angle ; Van Asch *et al.*, 2006), they appear here to be partially related to resistivity distribution and, consequently to grain size and hydraulic conductivity distribution.

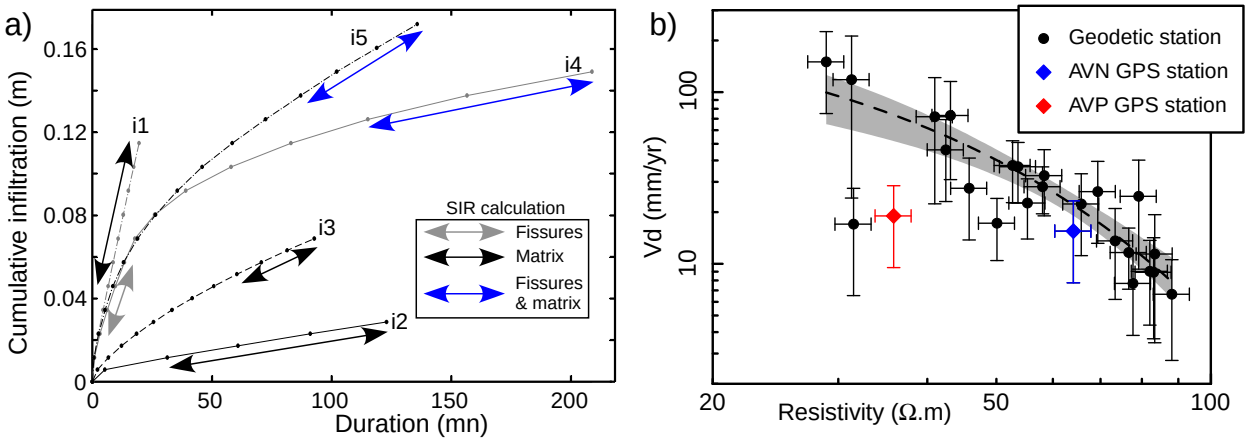

Figure 2.7 – Relationships between slide velocities, hydrogeological properties and resistivity on the Avignonet landslide (Bièvre *et al.*, 2016). **a)** Hydrogeological infiltration curves. Steady state infiltration rates SIR were deduced from the curve parts shown with double-arrowed lines. **b)** slide velocities Vd as a function of resistivity Ω at 10 m depth. The black dashed line and the grey stripe corresponds to the exponential law fit ($Vd = 342e^{-0.043\Omega}$) and to the 95 % confidence interval, respectively.

The main output of this study was to show that this lithological contact explains the main morphological features of the slope and controls the kinematics of the landslide. Both roughness and slide velocity values show a dramatic change at the elevation of the lithological boundary, with an increase of these two parameters downslope. The interpretation (Fig 2.8) is that the water in the upper aquifer discharges in the fissures initiated in the impervious clay layer, increasing pore water pressure and developing instability processes at different scales. The resulting slope

deformation is consistent with the observed increase in roughness below 700 m asl. The coarser grain size distribution and the greater hydraulic conductivity in the coarser sedimentary sequence at the top of the slide prevent high pore water pressure and induce surface deformation weaker than in the laminated clays outcropping downslope. The hydromechanical coupling, along with the landslide kinematics, then appears to be directly controlled by the Quaternary geological structure.

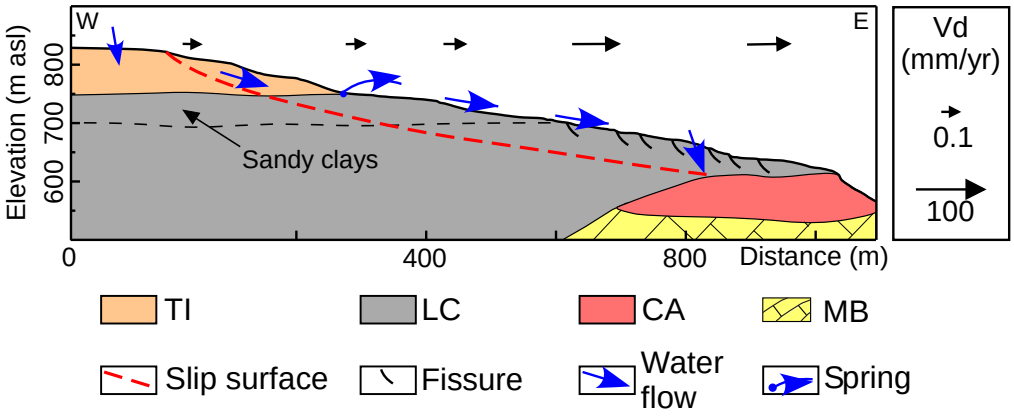

Figure 2.8 – Geological cross section (∼1 in Fig 2.5a for location) of the Avignonet landslide modified from Bièvre *et al.* (2016). The morainic colluvium is not represented. Black and blue arrows show the slide surface velocities (Vd) and the water flows, respectively. MB: Mesozoic bedrock ; CA: locally cemented alluvium ; LC: laminated clays ; TI: till.

This case study also illustrates how the initial understanding of a large landslide mechanism might be biased by the concentration of investigation in populated areas (or only close to infrastructures), here located in the southern clayey part of the slide. The study highlights the control of lithological variations on the landslide kinematics and the interest in using electrical resistivity tomography to map these variations in Quaternary sediments. The main outcome of this study is to highlight the need to apprehend the sedimentary history to better understand the observed present-day deformation pattern. However, it does not take into account the potential landslide activity since the deglaciation, a few tens of thousand years ago, and its influence on the development of further lithological heterogeneity within a landslide.

2.2.1.2 An insight into the development of lithological heterogeneity in a clayey landslide since the Last Glacial Maximum

The Avignonet site was chosen to be integrated in the OMIV observatory among other landslides in the Trièves area. Among other reasons, this is because numerous borehole and geotechnical data, as well as some literature, were available (Blanchet, 1988; Al Hayari *et al.*, 1990; Vuillermet, 1990; Giraud *et al.*, 1991). These direct data are mandatory to calibrate geophysical models. Geotechnical prospecting was also conducted during geophysical campaigns. As such, a lot of borehole data are presently available. A recent and close re-analysis of 10 of these boreholes revealed that the site is highly complex from a geological and geotechnical point of view (Bièvre & Crouzet, 2021).

The glaciolacustrine layers contain a very few per cent of organic matter, however sufficient enough to date the bulk sediment using ^{14}C. Chronological results are presented in Fig 2.9a. Lacustrine and till sediments were deposited on a paleoterrace issue from a former glaciation (i.e. the Riss glaciation older than 100 ka). An irregular trend is observed from the base to the top with ages between 40 and 50 ka at the bottom and between 30 and 40 ka at the top. They suggest a functioning of the lake during around 10 ka and with a sedimentation rate of

$\sim$1-1.5 cm/yr. These ages agree with previous findings (among others Lambert & Monjuvent, 1968; Monjuvent, 1973). Optically Simulated Luminescence (OSL) dates range between 20 and 50 ka and appear of little confidence, at least for the youngest age (20-30 ka). However, several outliers are visible in the figure. First, core T1 suggests ages younger by $\sim$5-10 ka for these lacustrine deposits (location of the borehole in Fig 2.5c). A shift of these samples towards the top by around 70 m (Fig 2.9b) sets these particular samples in agreement with the rest of the dates. This suggests that clay and till layers in the vicinity of T1 could have slid and are now located $\sim$70 m lower than their original position. This hypothesis will be discussed further. Finally, two other outliers with young ages compared to the sediments are observed. They correspond to plant remains found at outcrop in the neighbouring Harmalière landslide (Ly-2527) and 28.5 m depth in coring T4, both within lacustrine deposits. The young ages (500-515 yr cal BP for Ly-2527 and 265-310 or 145-215 yr cal BP for T4) suggest that they date reactivation phases.

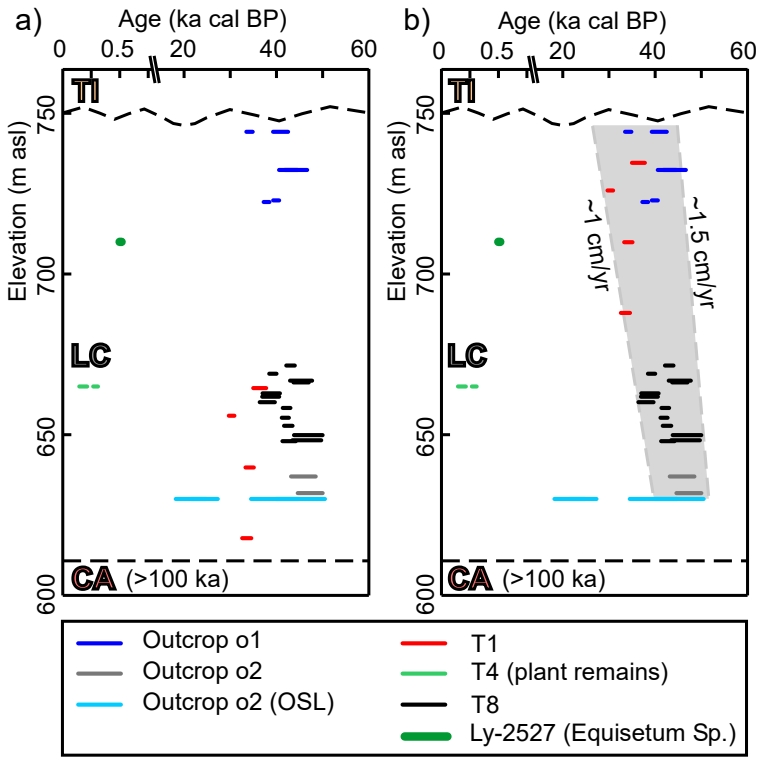

Figure 2.9 – ^{14}C dates (bulk sediment and plant remains) and OSL dates in the Avignonet area (Bièvre & Crouzet, 2021). LC: laminated clays; TI: till; CA: compact and cemented alluvium. **a)** Original data. **b)** The same with a 70 m upward shift of T1.

A re-analysis of the boreholes was conducted assuming the presence of palaeolandslides within the large Avignonet landslide, hypothesized from dating. Such structures have already been described in other sites (e.g. Jaboyedoff *et al.*, 2009, for the Pont-Bourquin landslide). Drilling Parameter Recording (DPR) from boreholes conducted to setup inclinometer tubes in the mid-1980s were digitized and combined to provide a strength parameter, namely the Somerton index Sd (Somerton, 1959), using the simplified relationship $Sd \approx Tp/\sqrt{Ar}$ proposed by Laudanski *et al.* (2013), from the advance rate Ar (m/h) and the thrust pressure Tp (bars). Figure 2.10a shows the original DPR of T0 with the raw data showing, notably, the addition of rods each 3 m. The data were low-pass filtered from these high-frequency events to compute Sd and results are shown in figure 2.10b along with measurements of the Undrained and Unconfined Shear Strength (USS) on core samples from T4 using a pocket vane shear test. The Somerton index (along with the drilling fluid pressure in Fig. 2.10a) allows the identification of different

lithological units such as the heterogeneous till, the laminated clays and a unit made of sand and gravel at the base of T0. The linear increase of strength in the laminated clays with depth (1.1 kPa/m) is in agreement with a sedimentary compaction trend (Bartetzko & Kopf, 2007) and suggests that these clays have been few remoulded by the landslide. In T4 (Fig 2.10b), lithological units were deduced directly from the analysis of core samples. The mechanical strength shows a progressive decrease from the surface down to 28.5 m and then a further increase down to the end of the coring. The presence of plant remains at 28.5 m and dated 145-214 or 267-309 yr cal BP (2σ range), along with the decrease in strength, suggests that the first 28.5 m of T4 are strongly remolded and underwent a slide during one of these periods. It is also notable that the lowest strengths are observed at the vicinity of the three identified shear surfaces.

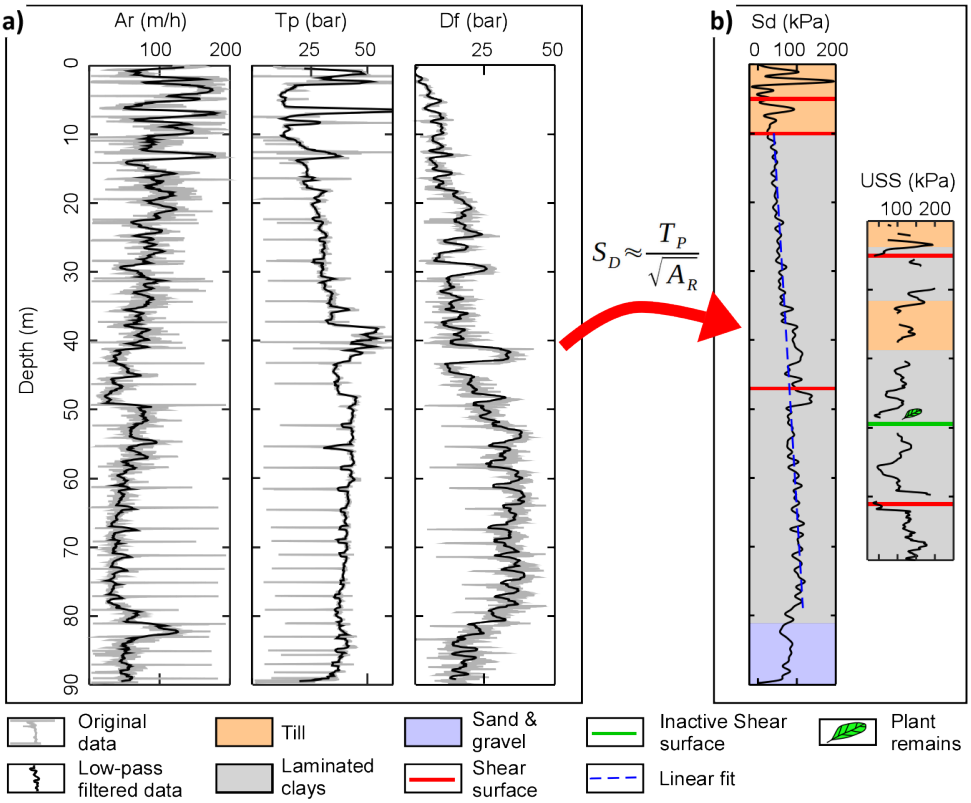

Figure 2.10 – Mechanical analysis of drillings. **a)** Digitized and filtered Drilling Parameter Recordings for T0. Ar: advance rate: Tp: thrust pressure; Df: drilling fluid pressure. **b)** Joint interpretation of mechanical parameters along T0, left, and coring T4, right, (location in Fig 2.5). Sd: Somerton index; *USS*: undrained shear strength. Modified from Bièvre & Crouzet (2021).

The same approach was used for the nine available boreholes. Interpretative geological cross-sections (not presented here) were built using outcrops, corings and lithological reconstruction from DPRs. They suggest a multi-phase activity of the southern part of the Avignonet landslide. A conceptual model of its evolution is presented in Fig 2.11. Figure 2.11a presents the Avignonet area during the Last Glacial Maximum, around 30-40 ka cal BP after chronological results, which was at the front of the Romanche glacier. Northward (retreat) and southward (advance) movements of the glacier (and of the shoreline of the paleolake) were induced by climatic oscillations and are illustrated by the lateral indentation between the lacustrine laminated clays and the till mixed with laminated clays. After the glacier definitive retreat, the date of which remains unknown but which occurred after 30-40 ka cal BP and left a subsequent thickness of till, the Drac river started to erode deeply into the soft till and clayey units (Fig 2.11b). This deep erosion was probably sufficient to allow the initiation of landslide. This is illustrated in Fig 2.11c where a massive landslide inducing a vertical motion of around 70 m, as suggested by

^{14}C ages in T1, at a time unknown, occurred on the northern side of the Avignonet landslide. This activation phase washed out a part of the fluvial layers observed between 625 and 635 m asl and explains their absence in T1. In terms of hydrogeology, the occurrence of a permeable fluvial alluvial layer at the bottom of T0 suggests that this layer drains water which is then trapped in the eastern part of the landslide. This trapped aquifer may have provided water able to help the landslide motion by lubricating the shear surface. After a period of erosion, and probable landslide activity, another well-documented landslide was activated in the southern part of the studied section in recent time. This is attested by ^{14}C age (145-215 or 265-310 yr cal BP with a 2σ range) on plant remains at 28.5 m depth in T4 (Fig 2.11d). This activation phase, which took place between AD 1640 and AD 1805 at the end of the Little Ice Age, is in agreement with another date in the nearby Harmalière landslide (Evin *et al.*, 1985). Stalks of *Equisteum sp.* found in clays suggest a reactivation phase 500-515 yr cal BP, i.e. at the beginning of the XIXth century. Finally, an unsourced local newspaper reported by Blanchet (1988) indicated a reactivation of the Avignonet landslide around AD 1850. All the results gained in this study support the high lithological variability induced by the geological history of the site during the deposition of the sediments and also because of the different landslide phases that occurred after the glacier retreat. This high variability induces a complex behaviour of the landslide.

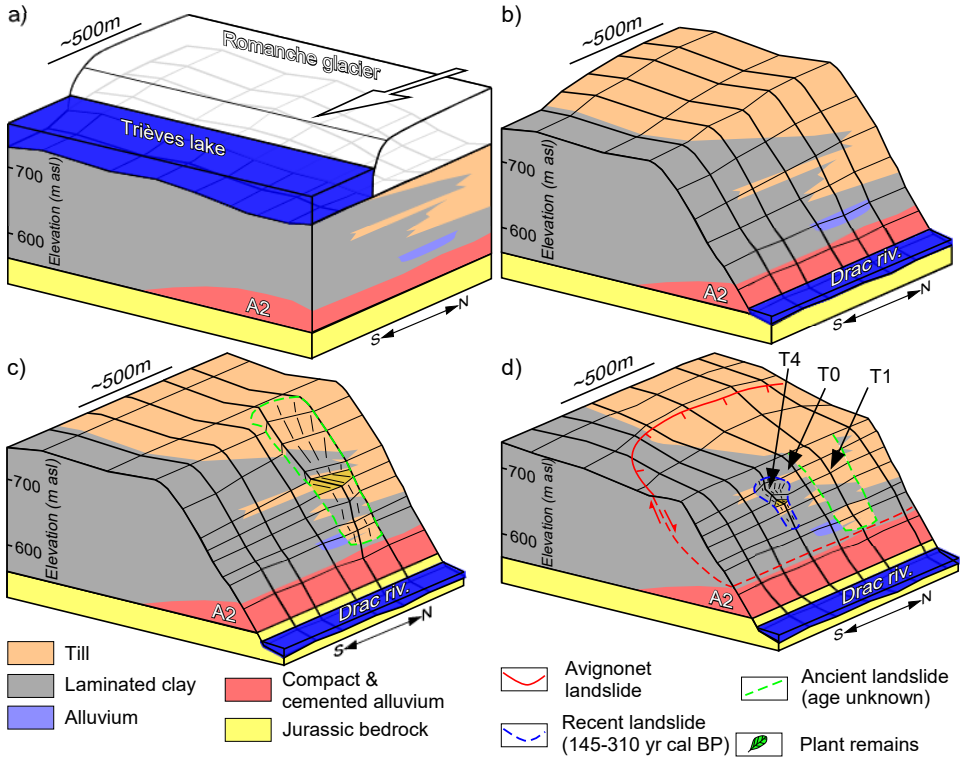

Figure 2.11 – Scenario of the evolution of the southern part of the Avignonet landslide (modified from Bièvre & Crouzet, 2021). **a)** Situation during the Last Glacial Maximum ; **b)** situation after the glacier definitive retreat ; **c)** 70 m downward movement of the northern part (timing unknown) ; **d)** 28 m downward movement at the end of the Little Ice Age and present-day situation. Boreholes are indicated along with the limits of the Avignonet landslide.

2.2.2 Seasonal and environmental factors controlling landslides

Slow-moving clayey earthslides frequently exhibit seasonal activity suggesting that deformation processes do not only depend on the slope and intrinsic geomechanical parameters. On the contrary, seasonal motion patterns are frequently observed with acceleration during the wet season and deceleration during the dry season (Iverson & Major, 1987; Van Genuchten, 1989; Van Asch *et al.*, 1996; Handwerger *et al.*, 2013; Lacroix *et al.*, 2020b, and recent references

herein). Within landslides, it is mainly the phreatic water table that is monitored. However, in the case of deep-seated landslides (>3 m depth) made of heterogeneous lithological units and with several slip surfaces, the characterization of the phreatic water table does not allow to relate satisfactorily the activity of the landslide with environmental parameters such as rainfall and subsequent water infiltration at depth. Section 2.2.2.1 presents a study conducted in the French Alps to analyze the seasonal fluctuations of both landslide kinematic and hydrometeorological parameters at surface and depth.

In the case of landslides moving several m/yr, it is however difficult to set instruments in the moving mass to monitor the evolution of physical parameters such as the water table and its relationship with landslide kinematics. Section 2.2.2.2 presents how geophysical parameters were used to evidence periodic and reversible variations controlled by seasonal environmental parameters.

2.2.2.1 Preferential water infiltration in clayey earthslides

A study conducted on the Charlaix landslide (CH in Fig 2.4 for location and detailed view in Fig 2.12) in the Beaumont area presents a seasonal analysis of water infiltration within this slow-moving clayey landslide (Bièvre *et al.*, 2018b).

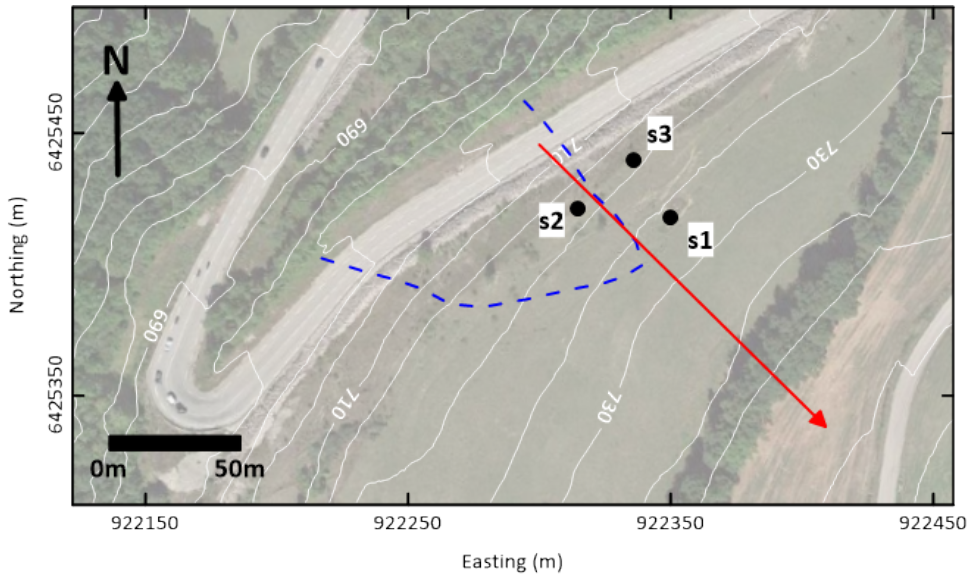

Figure 2.12 – Location of the Charlaix landslide and of the experiments. s1: seismic station. s2 and s3: seismic and GNSS stations. Blue dashed line: main sliding area. Red arrow: location of the profile shown in Fig 2.16.

The landslide is situated within laminated, glacio-lacustrine clays similar to those in the Trièves area. The conceptual model for water infiltration in these clays was developed in the 1990s (Nieuwenhuis, 1991; Vuillermet *et al.*, 1994; Van Asch *et al.*, 1996) and is presented in figure 2.13. It was developed for explaining the triggering effect of the snowmelt and precipitation on the clay slopes of the Trièves and Beaumont areas. Water first infiltrates in the permeable colluvial cover and generates a perched ground water table in this layer, which directly responds to rainfalls. This water mass feeds the open fissures that can be caused by desiccation during dry periods and/or by gravitational deformation. The major landslide-generated fissures are connected to the slip surfaces existing at different depths and this fissure system drains in a downslope direction through the silt laminae and the locally interbedded sand layers. Because of the pressure head maintained by the perched water in the fissures, one may expect that slip surfaces are following silt and/or sand interfaces. This model is supported by geomorphological observations and geotechnical drillings on several landslides indicating a translational movement

in most part with a rotational component in the upper part. Vertical flows in the laminated clays can be neglected because of the very low permeability perpendicular to the bedding planes ($\sim 10^{-10}$ m/s). Permeability parallel to these planes ($\sim 10^{-8}$ to 5×10^{-9} m/s) is a little lower than in silt ($\sim 4 \times 10^{-8}$ m/s). The role of the imbricated fissure system then appears predominant for vertical water infiltration and landslide triggering (see section 2.2.1.1).

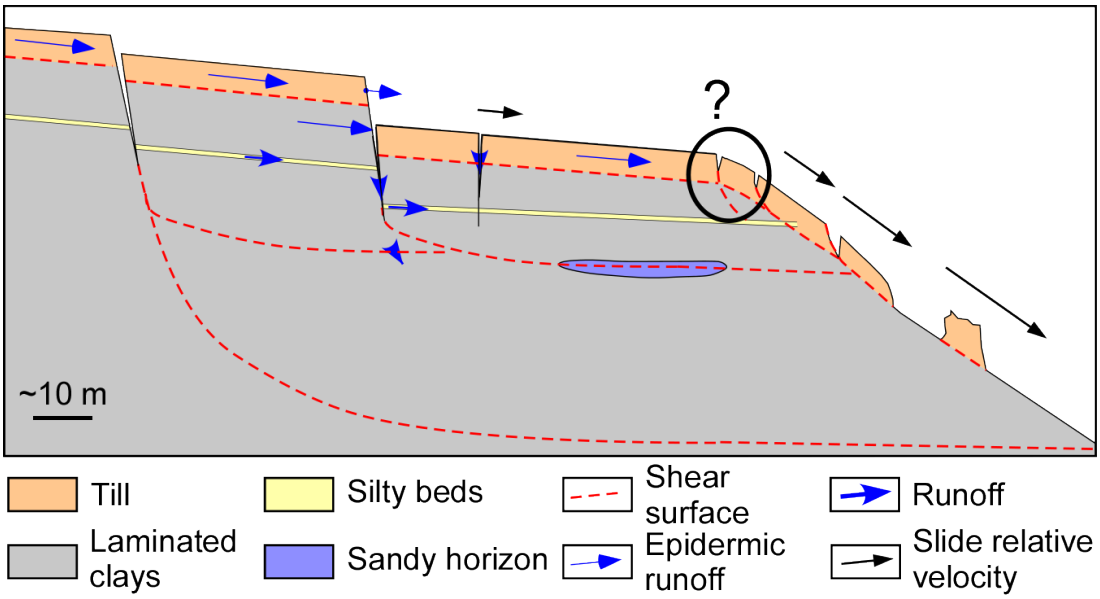

Figure 2.13 – Conceptual framework for the development of landslides and water infiltration within fissured laminated clays. Modified from Van Asch *et al.* (1984) and Bièvre *et al.* (2012).

An extensive geophysical (electromagnetic induction mapping, electrical resistivity tomography, seismic refraction tomography, surface wave inversion) geotechnical (coring, drilling, inclinometer), hydrogeological (piezometer) and geodetic survey was performed between 2010 and 2017. This landslide showed two main sliding zones with motions up to 10 to 15 cm/yr. Following remediation works achieved in 2009, one specific zone over the two previously sliding continued to exhibit motions of the same order of magnitude. The objective of this study was to establish a geological and geotechnical model and to understand the seasonal variations of displacement rates observed in situ. Geological and geophysical results showed that the site is complex with a heterogeneous vertical and lateral arrangement of lithological layers, which were deposited in a paraglacial environment comparable to Avignonet. A thick (20 to 30 m at least) permeable reservoir uphill (made of moraines and coarse-grained lacustrine and deltaic deposits), furthermore connected to the upper part of the landslide zone, was evidenced. Geotechnical prospecting (inclinometers ; Figs 2.14a and 2.14b) showed the presence of 4 main shear surfaces at depths of 4-5, 12, 15 and 30 m with more than 75 % of the deformation being accommodated within the first 12 m below ground surface. Surface (GNSS) and underground (from inclinometers ; Figs 2.14c and 2.14d) kinematics revealed a strong seasonality of the deformation with almost no displacement during dry seasons (April to October) and motions up to 16 cm/yr during wet seasons (November to March). Simplified stability computations taking into account the shallowest shear surface only and variable water table levels (highest in the wet season) showed a decrease of the safety factor during the wet season, with reduced global stability. This result is in agreement with surface and underground deformation observations which revealed higher velocity during these periods.

From geophysical and geological prospecting, it was hypothesized that a semi-permeable reservoir exists uphill and which could feed the landslide zone with a significant amount of water. The drainage of water from this reservoir to the upper part of the landslide zone would be favoured by the presence of a permeable channel. However, no increase related to a water flux from

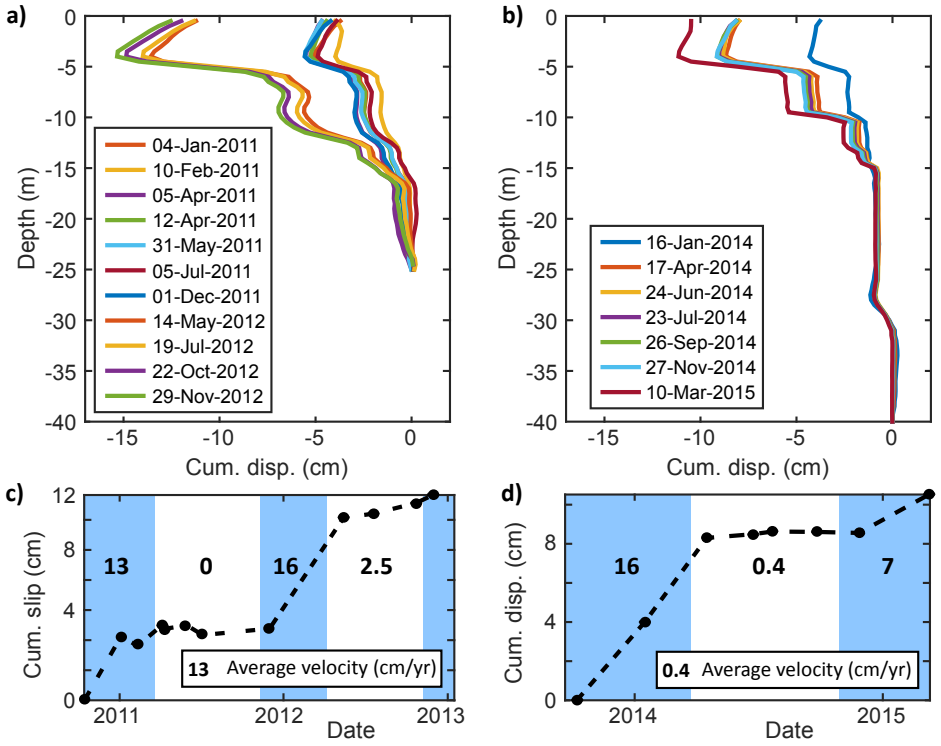

Figure 2.14 – Inclinometer results at the Charlaix landslide (Bièvre *et al.*, 2018b). Inclinometers are located close to s1 in Fig 2.12Data for **a)** i1 and **b)** i2. **c)** and **d)** Extraction of cumulative displacements at 4 m and 5 m depth for i1 and i2, respectively. The blue and white bands correspond to the autumn-winter season (November to March) and to the spring-summer season (April to October), respectively. Values inside the graphs correspond to the average velocity, in cm/yr, of each period.

this reservoir could be evidenced from the analysis of piezometric time series of the phreatic water table.

Further hydrogeological monitoring was conducted during four years between late 2012 and late 2016 to characterize the evolution of two water tables. The first is the phreatic water table located at around 7 m depth and the second is deeper (around 12 m depth) and located immediately above a shear surface. The cross-correlation of piezometer time series with effective rainfall showed that the deepest water table reacts twice faster to effective rainfall than the phreatic water table (Fig 2.15). This confirms the role of fissures and shear surfaces as preferential infiltration paths for rainfall from the surface down to 12 m at least in this work. Previous works, using notably geophysical methods, came to similar conclusions but with investigations limited to the very first metres below ground to focus on water infiltration at the surface (Bièvre *et al.*, 2012; Travelletti & Malet, 2012). Deeper investigations would tend to decrease the resolution of geophysical methods and of the target to be imaged. On the contrary, geophysical or hydrogeological measurements conducted in boreholes do not suffer from this resolution issue and can detect water infiltration paths in fissured media (Bièvre *et al.*, 2012; Lofi *et al.*, 2012). Overall, these results confirm the conceptual model for water infiltration in these quaternary clays (Nieuwenhuis, 1991; Vuillermet *et al.*, 1994; Van Asch *et al.*, 1996; Bièvre *et al.*, 2012; van der Spek *et al.*, 2013), and extend it with direct observations on deeper water tables, which had not been conducted before.

Furthermore, the seasonal cross-correlation of the same time series reveals a globally similar behaviour of the phreatic water table in summer and winter. Infiltrated rainwater reaches the water table within a few days (5 to 6 days) and is stored for a few tens of days (around 20 days) before the water is drained out of the aquifer. On the contrary, the second water table

showed a very contrasted seasonal behaviour. In winter, it behaves similarly to the phreatic water table but, in summer, it acts as a drainage structure with no significant effect of rainfall on the water table six days after a rain event. Nevertheless, the hydrogeological analysis of the time series showed that the two water tables are both sensitive to rainfall. This implies that water infiltration within the ground affects both reservoirs even if lags are observed. These new observations and analyses bring insight into the mechanisms of water infiltration at depth within clayey landslides and confirm the role of fissures connected to shear surfaces as preferential infiltration paths.

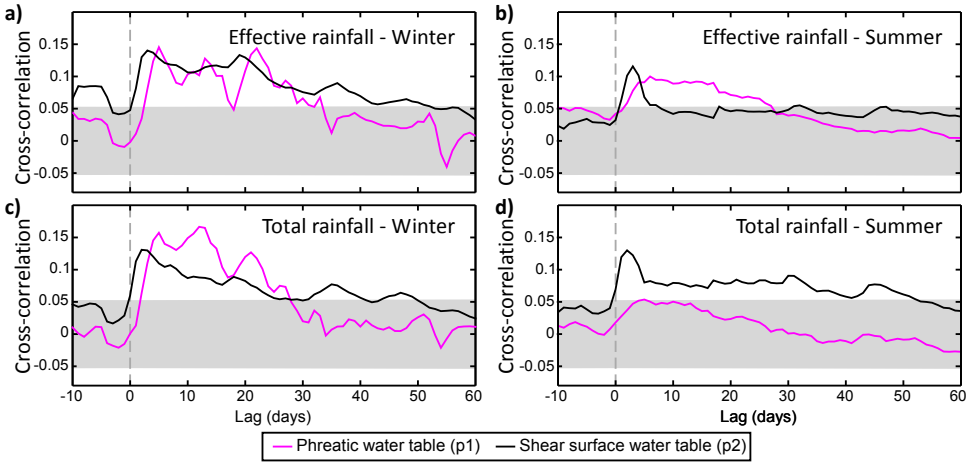

Figure 2.15 – Seasonal cross-correlation of water table and rainfall on the Charlaix lanslide (Bièvre *et al.*, 2018b). **a)** and **b)** Cross-correlation of water tables and effective rainfall in winter and summer, respectively. **c)** and **d)** Cross-correlation of water tables and total rainfall in winter and summer, respectively. Grey stripes represent the 95 % confidence interval.

However, despite the original observations conducted in this work, several issues remain to understand the relationships between water infiltration and landslide activity. First, the balance between run-off and infiltration is required to establish more robust correlations. It would allow discriminating the quantity of water infiltrating into the ground and reaching both water tables. Second, the impact of pore pressure increase on deformation, especially at the vicinity of shear surfaces, still needs to be assessed. Joint monitoring of these two parameters would allow to quantitatively evaluate the physical phenomenon leading to landslide acceleration. The experimental monitoring of these parameters at depths of several metres within active landslides remains challenging. This point will be discussed in section 2.3.2.2.

Table 2.1 – Hydraulic properties measured on the Charlaix landslide and comparison with the Avignonet landslide (Bièvre *et al.*, 2012; van der Spek *et al.*, 2013; Bièvre *et al.*, 2016). IR: infiltration rate; SIR: saturated infiltration rate after Beerkan tests.

Unit	IR (x10^{-5} m/s)		SIR (x10^{-5} m/s)	
	Charlaix	Avignonet	Charlaix	Avignonet
Moraines	1.48	2.7	1	1
Laminated clays			0.57	0.3
Along fractures	7.7	5		4

2.2.2.2 Influence of seasonal environmental parameters on clayey mudflows

Following the occurrence of an earthflow/mudflow of a few thousand cubic meters at the toe of the Pont-Bourquin Landslide (Swiss Alps ; location in Fig 2.17a) in late August 2010 and the sharp drop of 7 % in shear-wave relative velocity dV/V that was measured up to seven

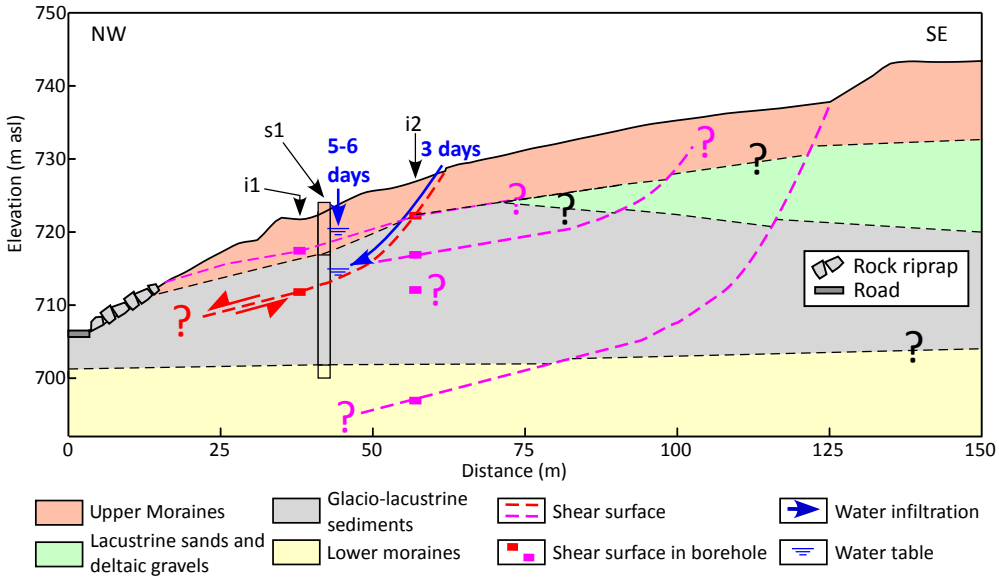

Figure 2.16 – Synthetic geological and geotechnical cross-section and conceptual model for water infiltration in the Charlaix landslide (Bièvre *et al.*, 2018b). The shear surface in red corresponds to the shear surface above which the deepest water table is studied in this work.

days before that event (Mainsant *et al.*, 2012b), two monitoring systems made of three pairs of geophones (1a-b to 3a-b) and 36 electrodes were installed across the transportation and accumulation zones of the landslide (location in Fig 2.17a). These works were conducted within the frame of a PhD (Carrière, 2016).

The seismic monitoring system allowed daily relative changes in seismic velocity to be measured for a period of 4.5 years between late October 2011 and mid-March 2016. Cross-correlations were conducted for pairs of seismometers investigating across the landslide (1a-1b, 2a-2b and 3a-3b). No dramatic drop of the seismic velocity was observed during this period, consistently with the lack of significant landslide acceleration or earthflow/mudflow event. Slow-motion however occurred, as shown by the geodetic target tracking (slide velocity of 1 to 5 m/yr) and the elevation variations in the transportation and accumulation zones, reaching -2.5 m and 2.5 m in 4.5 years, respectively. During the quiet period after the August 2010 event, the seismic velocity time series show periodic and reversible variations in a range -2 % to 2 % (Fig 2.18a), suggesting a probable influence of seasonal parameters.

The three seismic time series were cross-correlated with daily environmental time series (temperature and rainfall, shown in Figs. 2.18b and 2.18c, respectively). In the long term (yearly scale), dV/V variations are mainly driven by the temperature with relatively short delays varying from 30 days below the main secondary scarp (MSS) to 50 days at the top of the accumulation zone. These lag values indicate that the shallow layer (2 m or less) controls the dV/V variations, explaining the faster response in the fractured zone just below the MSS. In the short term, the rigidity variations (measured by the parameter dV/V) are weakly correlated to rainfall, exhibiting a small decrease in dV/V with a delay of a few days (2 to 5), in contrast with the displacement rate that almost instantaneously responds to the rainfall.

Although no acceleration and fluid-like motion occurred during the studied period, the continuous monitoring of dV/V has proved to be a robust method for getting information at depth, with no data gap even in snow conditions, in contrast to extensometer data. The seasonal reversible seismic velocity variations turned out to be in a range lower than the drop observed before the August 2010 earthflow/mudflow, highlighting the interest in incorporating the dV/V technique in monitoring systems.

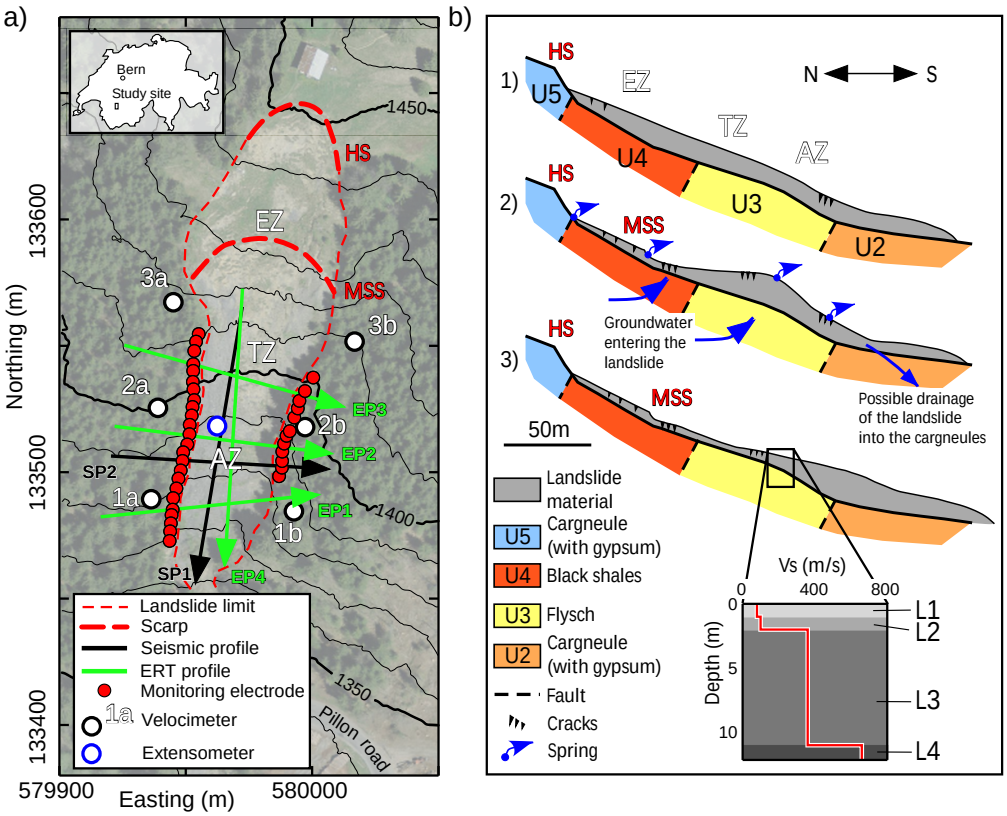

Figure 2.17 – The Pont-Bourquin Landslide. **a)** Location of the study site and of the instruments on the slope. Coordinates are metric and expressed in the Swiss Grid format. HS: main headscarp; MSS: main secondary scarp; EZ: erosion zone; TZ: transport zone; AZ: accumulation zone. **b)** Conceptual evolution model of PBL showing 3 stages : 1) stable state, 2) landslide in the EZ with transportation of material to the AZ, 3) triggering of a debris flow in the AZ after heavy rainfall. The Vs profile with the different interpreted units (L1 to L4) in the accumulation zone is shown (adapted from Mainsant *et al.*, 2012b). Figure from Bièvre *et al.* (2021).

In parallel with the seismic monitoring, electrical resistivity monitoring was also tested on the site. Results in the past decade have shown the potential of this technique to monitor water infiltration from the surface into unstable and/or fissured slopes (Krzeminska *et al.*, 2009; Bièvre *et al.*, 2012; Travelletti *et al.*, 2012; Uhlemann *et al.*, 2017). Apparent resistivity (ρ_a) is measured using 2 current-injecting electrodes (labelled A and B) and 2 further electrodes (labelled M and N) to measure the induced voltage (Telford *et al.*, 1990). The apparent resistivity ρ_a (Ω·m) is computed using equation 2.2 :

$$\rho_a = K \cdot R = \frac{2\pi}{\frac{1}{AM} - \frac{1}{BM} - \frac{1}{AN} + \frac{1}{BN}} \cdot \frac{V_{MN}}{I_{AB}} \tag{2.2}$$

where K is the geometric factor (m), R is the electrical resistance (Ω), V_{MN} is the voltage (V) measured between electrodes M and N and I_{AB} is the electric current (A) measured between electrodes A and B. When the method is appropriated to site conditions, i.e. with a resistivity contrast sufficient enough between the landslide and the undisturbed ground, inversion of apparent resistivity provides 2D and 3D images of the geological setting and of the landslide geometry (Chambers *et al.*, 2011; Travelletti & Malet, 2012; Bièvre *et al.*, 2018b; Crawford & Bryson, 2018). When measurements are repeated over time, the method allows monitoring changes in resistivity $\Delta\rho$ (Travelletti & Malet, 2012; Uhlemann *et al.*, 2017) by measuring changes in the ground resistance ΔR (cf. equation 2.3).

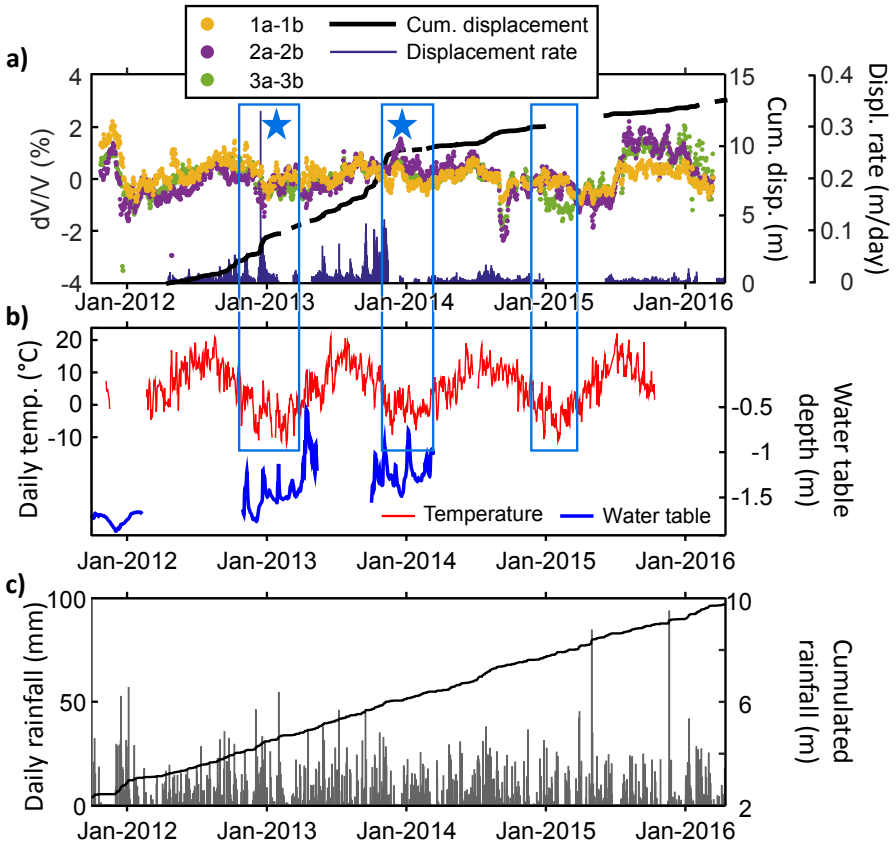

Figure 2.18 – Seismic, kinematics and environmental time series at the PBL (Bièvre *et al.*, 2018a). **a)** Seismic velocity (dots) derived from the three pairs of sensors (1a-1b, 2a-2b, and 3a-3b) and extensometer data (black line and blue bars). The two blue stars denote the two dV/V peaks that could result from icing effect during the main freezing periods (blue rectangles). **b)** Water table (blue curve) and daily temperature (red curve). **c)** Daily rainfall (grey bars) and cumulated rainfall (black curve).

$$\Delta\rho = K \cdot \Delta R \tag{2.3}$$

Resistivity can be related to water content and be used to monitor hydrological changes in the sub-surface (Bièvre *et al.*, 2012; Travelletti *et al.*, 2012). Quantitative relationships between resistivity and water content have been established using empirical relationships calibrated in the laboratory (Waxman & Smits, 1968; Yeh *et al.*, 2002; Chambers *et al.*, 2014; Uhlemann *et al.*, 2017). However, electrodes located on the sliding mass move relatively to each other. This induces a change in the geometric factor (ΔK) that was used by Wilkinson *et al.* (2010, 2015) to retrieve electrode displacement at the surface by measuring resistivity variation ($\Delta\rho$). This hypothesis implicitly assumes that the variation in apparent resistivity is related to a change in geometric factor and not to a modification of the ground porosity and/or water content and, consequently, ground resistance (ΔR; equation 2.4).

$$\Delta\rho = \Delta K \cdot R \tag{2.4}$$

This potential pitfall was overcome by Uhlemann *et al.* (2015) who geodetically monitored a subset of the installed electrodes to reconstruct the geometry of all the electrodes before inverting a 3D dataset. Finally, recent works also showed the possibility to process in time-lapse data with *ad hoc* topography and mesh (and, consequently, geometric factors) for each

time sequence (Whiteley *et al.*, 2020) even when the landslide is active. Measuring resistivity in the field is generally quick and efficient. However, the need to determine electrode location for each measurement requires the addition of high-resolution geodetic monitoring systems, increasing the cost of the monitoring setup.

This research was motivated by the difficulty of setting up geophysical instruments on landslides that move over several m/year and that can evolve in mudflows, such as the Pont Bourquin landslide (PBL) in Switzerland. Due to the interest in obtaining both seismic velocity and electrical resistivity variations on the same site, 36 electrodes were deployed on either side of the unstable zone. The objective was twofold: test the capacity of an installation with external electrodes to detect resistivity variations in the landslide, and compare the changes in velocity and resistivity to get a better insight into the PBL behaviour. The main changes in apparent resistivity are expected to come mainly from surface water infiltration. Unlike V_S, laboratory experiments have indeed not shown any significant change in electrical resistivity at the solid-fluid transition (Carrière *et al.*, 2018a, see section 2.2.3.2). In the case of the occurrence of mudflow, the fluidization at the base of the landslide will probably not induce any change in resistivity. The study first focused on obtaining a detailed 3D electrical image of the landslide. In a second step, the capacity of the resistivity method with such a setup (electrodes located outside the unstable zone) to detect resistivity variations in the landslide mass was numerically evaluated. Finally, the time series of resistivity and seismic velocity (235 days) are compared and interpreted in light of the environmental parameters.

Results of the 3D inversion of 2D profiles EP1 to EP4 are presented in Figs 2.19a (3D image) and 2.19b (1D resistivity curves extracted from the 3D model). The inversion process converged after a few iterations with $\chi^2 \sim 1$ and RRMSE $\sim 10\,\%$. The landslide body is well detected with a low resistivity of 75-80 Ω m, while the resistivity of the bedrock is slightly higher in the accumulation zone (150-170 Ω m) than in the transport zone (120 Ω m). This variation is probably due to the difference in bedrock lithology, with the presence of flysch in the accumulation zone and the predominance of black shales in the transport zone (Fig 2.17b). The landslide presents an average thickness of 10 m (Fig 2.19b) in agreement with the shear-wave velocity (Vs) profile of Mainsant *et al.* (2012b) located at the intersection between EP2 and EP4 and shown in the same figure. The volume of the landslide imaged below the main secondary scarp is $22.5 \times 10^3\,\mathrm{m}^3$.

The time-series analysis was conducted splitting the landslide body into four zones (the two transport zone TZ and accumulation zone AZ, at two depth ranges 0-5 m and 5-11 m). As similar results were obtained for AZ and TZ, only results of the accumulation zone will be further presented. Environmental and displacement time series are shown in Fig 2.20a, while the resistivity time series of each zone (AZ 0-5 m and AZ 5-11 m) are presented in Fig 2.20b. Fig 2.20b also shows the time series of surface wave velocity variations (dV/V) in the range 8-12 Hz (sensitive to changes from the surface down to around 10 m) reported by Bièvre *et al.* (2018a). At the seasonal scale, the two time series of resistivity and dV/V show a similar evolution. The values decrease from February 2015 and reach a minimum in May, and then increase until the end of November. These observations indicate lower resistivity in winter and spring, in relationship with a shallower water table and a higher water content in the vadose zone during these seasons. On a shorter time scale, time series show rapid responses of both geophysical parameters to rainfall. This is highlighted by the blue and red arrows in Fig 10b which exhibit a decrease in resistivity and seismic velocity following precipitation events. However, it is observed that small precipitation events (< 15 mm per day) in winter and spring induce a drop in dV/V but not in resistivity (green arrows in Fig 2.20b). In addition, drops in resistivity appear to be greater in summer and autumn (red arrows) than in winter and spring (blue arrows). This could be related to widely open cracks in summer and autumn (Bièvre *et al.*, 2018a) that favour water infiltration following precipitation. Longer time series, however, are

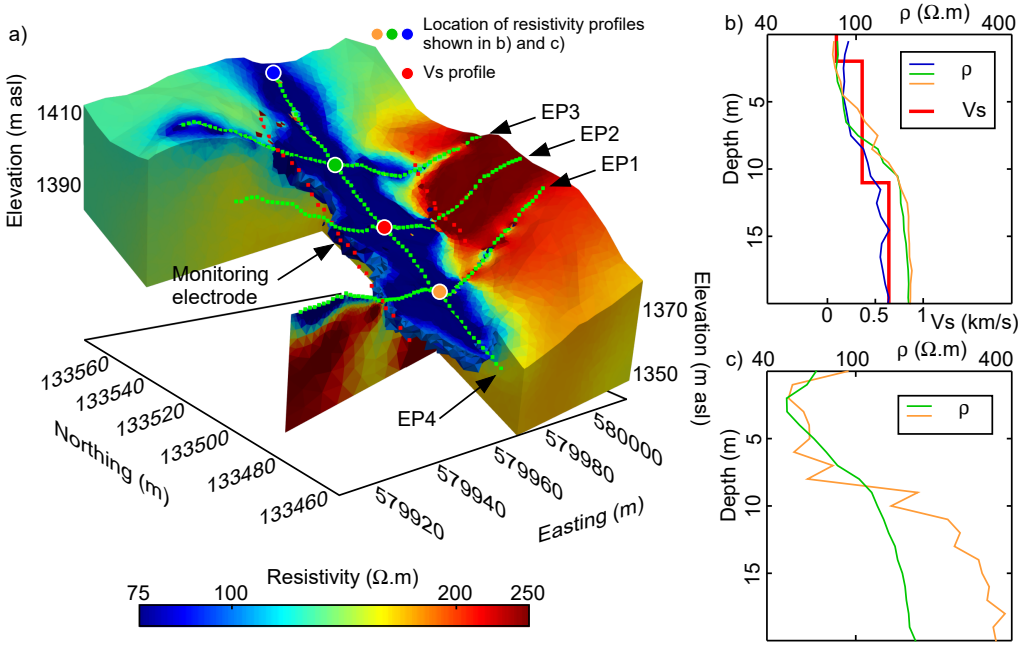

Figure 2.19 – 3D ERT on the Pont-Bourquin landslide (Bièvre *et al.*, 2021). **a)** 3D image of the PBL below the Main Secondary Scarp ($\chi^2 \sim 1$ and RRMSE $\sim 10\,\%$. **b)** 1D resistivity-depth curves extracted from the 3D model and comparison with the shear-wave velocity (Vs) profile from Mainsant *et al.* (2012b). The colours of the curves refer to their location in Fig 2.19a. **c)** Same as previous but with curves originating from the transverse 2D profiles.

required to confirm this observation and hypothesis. However, this observation is in agreement with findings of Merritt *et al.* (2018) on the Hollin Hill clayey landslide in England. They observed increases in temperature-corrected electrical resistance during summer periods. This increase was interpreted as resulting from desiccation and cracking. Intense periods of rainfall were followed by rapid drops of electrical resistance that were interpreted as caused by the annealing of cracks and the increase of soil water content in the very shallow subsurface.

At the seasonal scale, resistivity and dV/V time series are significantly (cc values between 0.75 and 0.85) and positively correlated with temperature (Fig 2.20c) with lags of 50 days ($\rho_{0-5\,m}$), 60 days (dV/V) and 70 days ($\rho_{5-11\,m}$). Merritt *et al.* (2018) observed similar lags (~ 1.5 month) with temperature-uncorrected electrical resistance (median depth of investigation of around 1.9 m). In this work, the increase of temperature-corrected resistivity is attributed to a decrease in water content, which is itself caused by an increase in temperature (and, hence, by an increase in evaporation). The similar lags suggest that, in the present study, resistivity is mainly sensitive to variations at a shallow depth.

Time series were then high-pass filtered (corresponding threshold of 30 days) to focus on short-term effects and cross-correlated with precipitation. The curves (Fig 2.20d) show a negative correlation with a rapid reaction of resistivity ($\rho_{0-5\,m}$ and $\rho_{5-11\,m}$) to precipitation. The correlation coefficient cc is maximum for a lag of 1 day, with a further rapid increase and no significant effect for durations greater than 3 days after precipitation. The comparable reaction of each depth range to precipitation underlines to the low ability of the monitoring system to localize resistivity changes at depth. It confirms numerical results and indicates that resistivity measurements in this work provide information that must be considered global at the scale of the landslide.

The cross-correlation of unfiltered resistivity with dV/V is presented in Fig 2.20e. All curves exhibit a maximum cc (0.8-0.85 for the 2 resistivity curves) for a lag of 0 days, miming auto-correlation curves. This highlights a high similarity between resistivity and dV/V curves, which

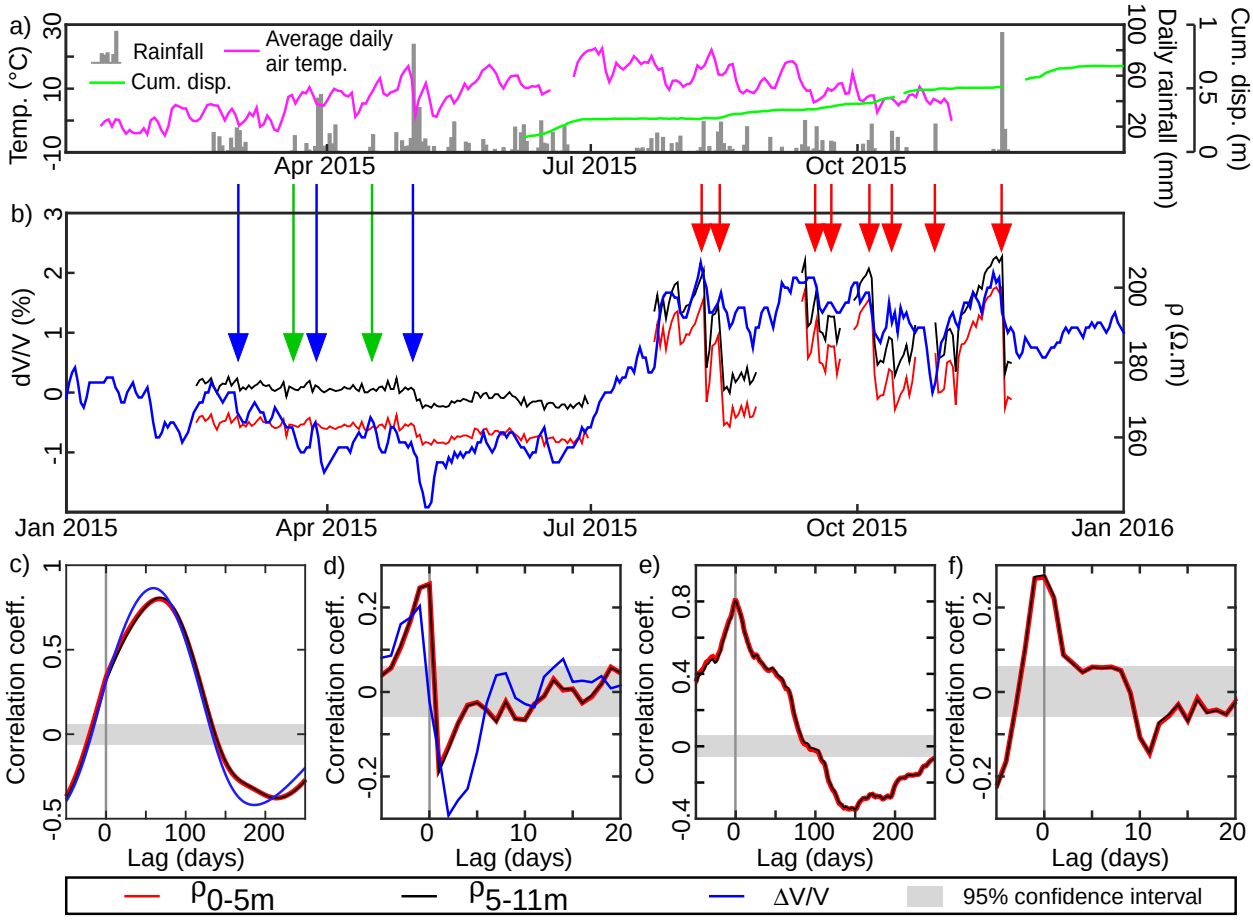

Figure 2.20 – Resistivity, seismic velocity and rainfall time series analysis (Bièvre *et al.*, 2021). **a)** Average daily air temperature, daily precipitation and daily cumulative displacement. **b)** Resistivity and relative seismic velocity time series. Red, green and blue arrows indicate precipitation-related events. Green arrows indicate small rain events (<15 mm) followed by a drop of seismic velocity but no change in resistivity. Blue (resp. red) arrows indicate small (resp. pronounced) drops of seismic velocity and resistivity in winter and spring (resp. summer and autumn). **c)** Correlograms of unfiltered resistivity and seismic velocity with temperature. **d)** Correlograms of high-pass filtered (corresponding period of 30 days) time series of resistivity and seicmic velocity with precipitation. **e)** Correlograms of unfiltered resistivity with seismic velocity in the two zones. **f)** Correlograms of high-pass filtered (corresponding period of 30 days) resistivity with seismic velocity.

is visible on the time series in Fig 2.20b. These results suggest that these 2 geophysical parameters react simultaneously to environmental forcing at the seasonal scale. The same analysis was conducted with high-pass filtered time series (corresponding period of 30 days) to study the correlation for short-term events. Results (Fig 2.20f) show moderate but significant ($cc = 0.2$ to 0.3) positive peaks of correlation at no lag with a subsequent rapid decrease to non-significant values for lags greater than 2 days. These results indicate a similar reaction of both geophysical parameters with decreases in resistivity and seismic velocity rapidly following short-term events such as precipitation. Once again, this can be observed on time series (arrows in Fig 2.20b). Finally, these results suggest that the geophysical parameters are better correlated at the seasonal scale than at the short-term scale.

This analysis shows a similar reaction of the two geophysical parameters to both seasonal and short-term environmental parameter variations, suggesting a common control factor. On a seasonal scale, the increase in resistivity and dV/V in spring and summer suggests a decrease in water content and an increase in rigidity in the superficial layer, resulting from the continuous increase in temperature. In autumn and winter, there is an inverse relationship with the constant drop in temperature. In the short term, precipitation generates a decrease in resis-

tivity and seismic velocity due to the infiltration of water into the ground, but with different behaviour depending on the season. In summer and autumn, rainfall is immediately followed by a significant drop in resistivity, while in winter and spring, only heavy rainfall or snowmelt causes a decrease in resistivity. This could be interpreted as the result of cracks much more wide open in summer and autumn because of shrinkage, and thus favouring water infiltration at depth, as already suggested on other landslides (Bièvre *et al.*, 2012; Travelletti & Malet, 2012; Merritt *et al.*, 2018). The behaviour is illustrated in Figs 2.21a and 2.21b for winter/spring (limited infiltration through cracks) and summer/autumn (higher amount of infiltration through cracks), respectively.

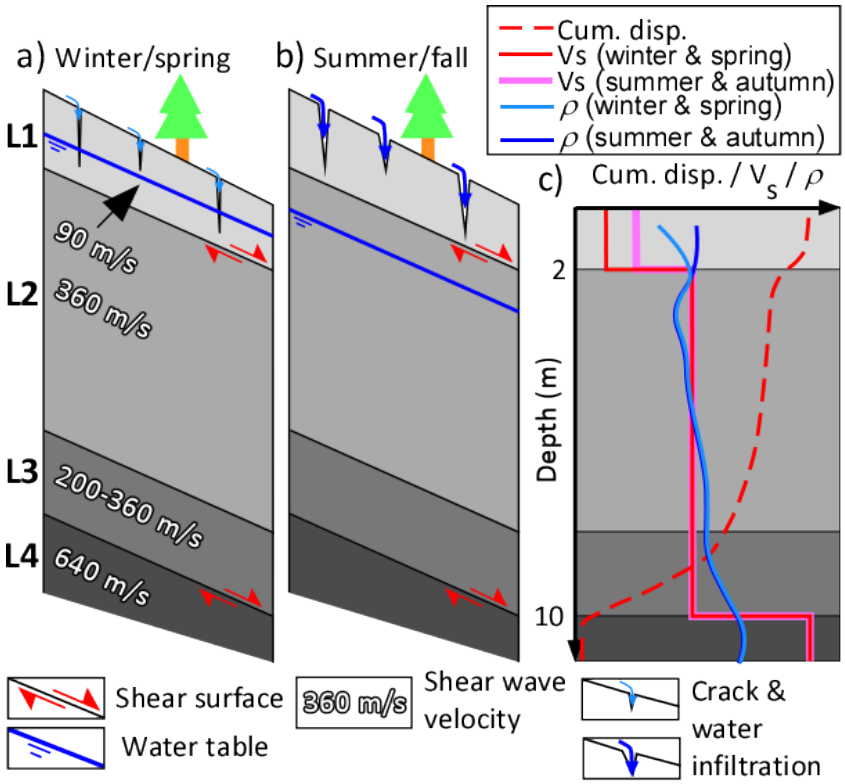

Figure 2.21 – Slope deformation model of the Pont-Bourquin Landslide (Bièvre *et al.*, 2021). **a)** Sketch in winter and spring with a shallow water table and clogged fissures. **b)** Sketch in summer and autumn with a deeper water table and widely open cracks allowing rapid water infiltration. **c)** Measured geophysical parameters (V_S, ρ) and conceptual cumulative displacement profile (cum. disp.).

To conclude this section, the Pont-Bourquin landslide was monitored using a setup with electrodes located in the stable zone was used to detect resistivity variations in the landslide, similarly to what was done previously with seismic sensors to reveal velocity variations dV/V. An extensive numerical study using the 3D landslide electrical model was performed to test the sensitivity of the measurements to resistivity changes in the landslide. It turned out that these changes are detected by the external electrodes but cannot be spatially localized, even though the structure of the landslide is well known. The results of the time-lapse experiment of 235 days conducted with that setup show that dV/V and resistivity time series have a similar shape and are therefore driven by the same environmental parameters. At the seasonal scale, dV/V and resistivity are positively correlated to temperature with no lag, suggesting a seasonal water content variation predominantly controlled by temperature. On a scale of a few days, dV/V and resistivity are moderately and negatively correlated to rainfall with time lags of a few days, indicating rapid infiltration of water into the ground. The drops of resistivity following rainfall appear stronger in summer and autumn, suggesting a higher amount of infiltration through more widely open fissures and cracks because of shrinkage. Regardless of the time scale, most of the geophysical variations measured during this experiment therefore probably come from

water content changes in the upper layer. Although laboratory experiments indicate that the electrical resistivity does not vary during clay fluidization, the evolution of electrical resistivity before and during a mudflow such as the August 2010 event that generates a precursory drop of 7 % in dV/V remains an open question.

2.2.3 Geophysical parameters precursory to rupture

A decade ago, it was shown that shear-wave velocity Vs is a geophysical parameter sensitive to clay deformation (Renalier *et al.*, 2010b,a; Mainsant *et al.*, 2012b) and it has been confirmed ever since (Larose *et al.*, 2015a; Mainsant *et al.*, 2015; Berti *et al.*, 2018; Bièvre *et al.*, 2018a; Fiolleau *et al.*, 2020; Bièvre *et al.*, 2021; Le Breton *et al.*, 2021; Berti *et al.*, 2022). The questions leading the works exposed hereafter concern the potential of other geophysical parameters (seismic, electrical) to detect significant variations precursory to rupture or fluidization in the laboratory and the field.

Section 2.2.3.2 investigates in the laboratory the evolution of Vs and electrical resistivity ρ, along with mechanical parameters, during fluidization beyond the liquid limit. In section 2.2.3.3, multiple seismic parameters complimentary to Vs (number of seismic events, seismic energy, resonance frequency) are analyzed during the rupture of a clay block that occurred on the Harmalière landslide in late 2016.

2.2.3.1 Preamble on geophysical parameters used for clayey landslide characterization

Geophysical methods have been used for several decades to characterize fine-grained landslides. Among the different techniques, 2D imaging using P-waves, S-waves and electrical resistivity is the most commonly used. Figure 2.22 presents an illustration of such images acquired in the Avignonet landslide. Profiles are located along the same line, in the bottom part of the landslide. A borehole with an inclinometer was also set to calibrate geophysical methods. Two main shear surfaces were observed at depths of 5 and 15 m. The electrical resistivity tomography (64 electrodes each metre, Wenner configuration, 651 measurements) is presented in figure 2.22a. It shows alternations of low resistivity ($\rho < 50\,\Omega$.m, laminated clays) and higher resistivity horizons ($\rho > 50\,\Omega$.m, more or less saturated moraines). However, no interface is evidenced that could correspond to a shear surface. As such, electrical resistivity appears suited to detect lithological and/or water content variations.

For P-wave velocity (Fig 2.22b ; 24 vertical geophones each 2.5 m, 24 sources and 585 first break picks), the image shows a low-velocity layer ($Vp < 600$ m/s, unsaturated moraines) over the first 2 to 3 m below surface. The base of this horizon is parallel to the ground surface and the unit below shows a velocity greater than 1500 m/s (saturated moraines and laminated clays). No interface is evidenced at 5 or 15 m depth. In this case, P-wave velocity variation is attributed to the presence of a water table.

The S-wave velocity tomogram is presented in figure 2.22c. It was conducted with 24 horizontal geophones regularly spread each 2.5 m. 13 sources provided 272 first break picks. The image shows 3 main units. From the surface down to 5 m depth, Vs is around 150 m/s. The base of this unit is parallel to the ground surface. The underlying unit has a velocity of around 250-300 ms ; its base is sub-horizontal and located at an elevation of around 675 m. Finally, the lowermost unit has a velocity of around 450 ms. There is a good agreement between the Vs layering and the location of the 2 shear surfaces at depth. In this case, Vs appears suited to locate shear surfaces.

Finally, figure 2.22d presents the evolution of Vs at 10 m depth as a function of the distance

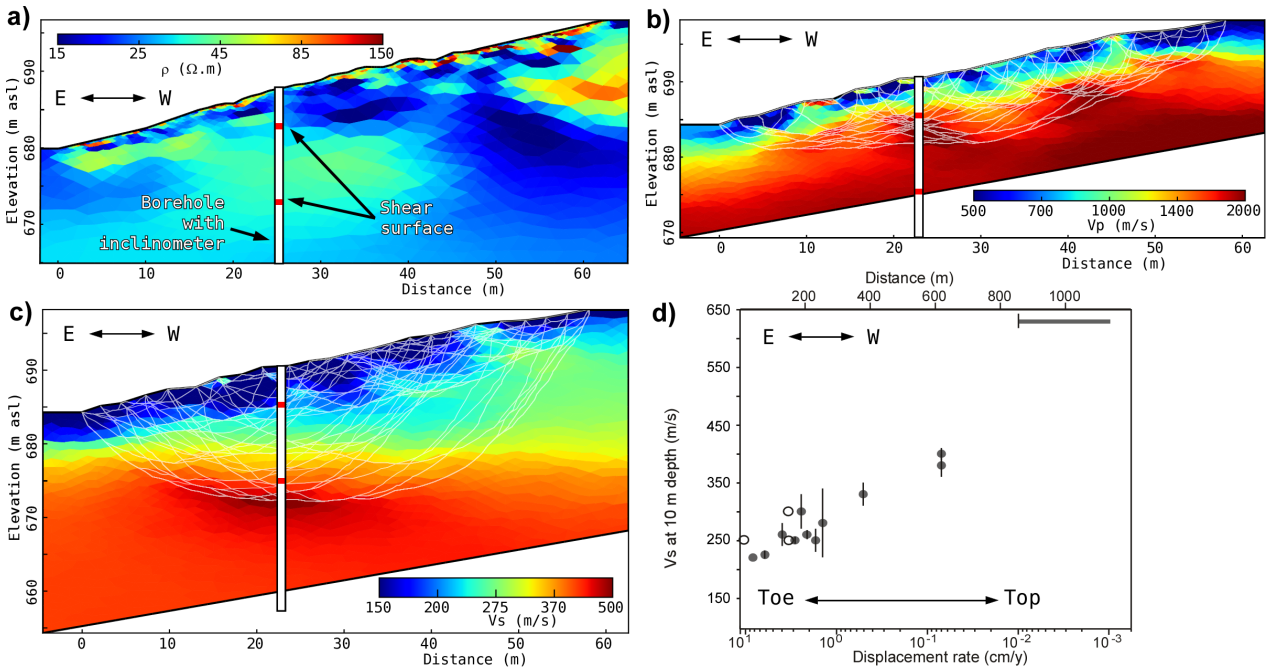

Figure 2.22 – Spatial evolution of geophysical parameters in the Avignonet landslide. **a)** Electrical resistivity tomography. **b)** P-wave travel-time tomography. **c)** S-wave travel-time tomography. All inversions ended with satisfactory results ($\chi^2 \approx 1$ and RRMSE $< 5\,\%$). **d)** Evolution of shear-wave velocity values in the Avignonet landslide (with error bars) as a function of displacement rates at a depth of 10 m, and of distance from the toe (left) to the top of the landslide (right). Data are from surface-wave inversion and SH refraction studies. The point outside the landslide (Vs = 630 m/s) exhibits no measurable displacement and is represented as a thick line with a maximum displacement rate of 0.01 cm/year (figure modified from Renalier *et al.* (2010a)).

along the landslide and the displacement rate measured at the surface. The graph shows that the highest the displacement rate (and, hence, the disruption of the fine-grained sediments), the lowest the shear-wave velocity. These results were confirmed in laboratory experiments (Renalier *et al.*, 2010a) and suggest that Vs is a suitable proxy to evaluate the degree of disruption in fine-grained landslides.

2.2.3.2 Laboratory characterization of the solid-fluid transition

In addition to field measurements, numerous rheometric experiments were carried out in the laboratory (collaboration with G Chambon, INRAe Grenoble). Standard Creep (SCr) tests allow determining the critical shear stress τ_c (Pa) above which the tested soil behaves like a fluid, and also the critical shear rate γ_c (s^{-1}) below which the material cannot flow. This critical shear rate is associated with an abrupt viscosity drop (or bifurcation) at the solid-fluid transition, potentially leading to catastrophic fluidization. Oscillatory Creep (SCr) tests allow determining the associated drop in elastic shear modulus G (Pa) during the solid-fluid transition. Thus, the shear wave velocity V_S (m/s) is indirectly evaluated during these tests, using the relationship $V_s = (G/\rho)^{1/2}$, where ρ is the unit weight. These tests were conducted using soil samples from several European landslides susceptible to fluidization and which are presented in Carrière *et al.* (2018a,b).

The classical apparatus used for these tests was modified to further measure electrical parameters (resistivity and induced polarization). An example is presented in Fig 2.23 with laminated clays from the Harmalière landslide and for 2 water contents w of 57 % (Fig 2.23a) and 73.7 % (Fig 2.23b). The results show a significant drop in V_S (and fluidization of the soil sample) for tests for which the applied shear stress is above τ_c, while no change is observed when the applied shear stress is below τ_c. On the contrary, electrical resistivity shows no change (and

induced polarization revealed to be not usable). These tests were conducted on soil samples from 5 landslides (Harmalière, Pont-Bourquin, Holin-Hill, Super-Sauze and Char d'Osset). Results were similar for all the tested soils, with a drop of V_S and no resistivity change at the solid-fluid transition. However, these a priori surprising results can be explained using Archie's relationship modified to account for the presence of clays (Archie, 1942). All tested soils obey a common relationship (Fig 2.24a) with satisfactory statistics. A similar fit was tried using the Waxman-Smits relationship (Waxman & Smits, 1968) but it failed (Fig 2.24a). The good fit of a unique Archie's law to the experimental data for water contents higher than the liquid limit suggests that the phenomenon controlling the electrical conduction is the diffusion of ions in the pore fluid and that the Waxman–Smits model accounting for the surface conductivity is little adapted at these high water contents. The absence of bulk resistivity change at the solid-fluid transition then suggests that the cementation exponent m does not vary and that the average tortuosity of the particles remains the same (Carrière *et al.*, 2018a).

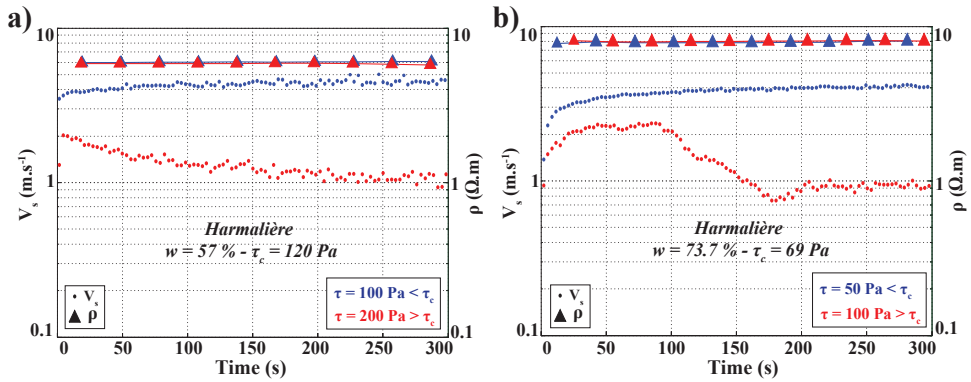

Figure 2.23 – Vs and ρ versus time measured during Oscillatory Creep (OCr) tests on Harmalière samples for two water contents **a)** $w = 57\,\%$, and **b)** $w = 73.7\,\%$. Blue points represent V_S values recorded during an OCr test for which the applied shear stress was below the critical shear stress τ_c. Corresponding resistivity measurements are blue triangles. Equally, red points and triangles correspond to V_S and ρ values recorded during an OCr test for which the applied shear stress was above the critical shear stress τ_c. Whereas the crossing of τ_c corresponds to a drop in V_S, no change of resistivity is recorded between solid and fluid state. Figure from Carrière *et al.* (2018a).

The rheometrical tests were extended to soils originating from 6 European landslides in various contexts (different ages, lithologies and morphologies ; Carrière *et al.*, 2018b). The results showed again a significant drop in G and γ_c when the applied shear stress is above the critical shear stress τ_c. The plot of τ_c as a function of the excess of w from the Atterberg Liquid Limit LL shows a common behaviour of all the tested soils (Fig 2.24). The value of the critical shear stress (the threshold of the solid-fluid transition) seems to be a function of $w - LL$. In other words, this threshold could be evaluated for any landslide using a limited, and easy to determine, set of geotechnical parameters: the stress, the liquid limit LL and the water content.

This approach was extended and was part of S Fiolleau's PhD thesis (Fiolleau, 2020). The strategy notably aimed at sampling different locations along the Harmalière landslide: are there different rheomechanical characteristics depending on the position along the slide (*versus* sliding)? Does the water in the soil, with variable geochemical characteristics during a season, influence the evolution of the environmental characteristics ? However, it was not possible to complete this work during the PhD and it is still ongoing.

2.2.3.3 Seismic characterization of a clay-block rupture

In late June 2016, the Harmalière clayey landslide (located 30 km south of the city of Grenoble, French Alps) was dramatically reactivated at the headscarp after a 35 yr-long period of continuous but limited activity. Two seismometers (HAR0 and HAR1 ; Fig 2.25) were installed at the

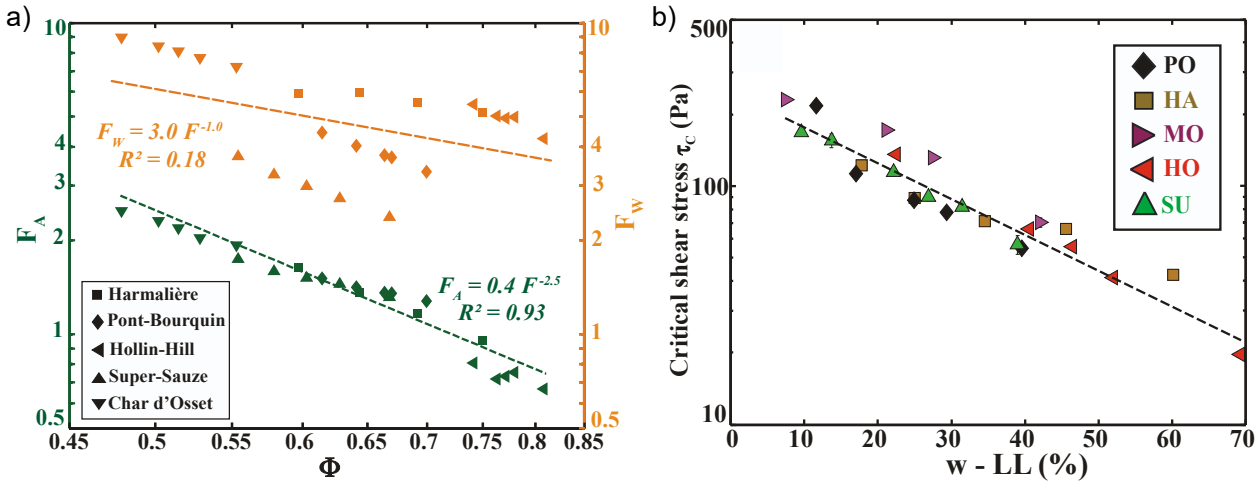

Figure 2.24 – Synthesis of laboratory experiments. **a)** Evolution of Archie and Waxman formation factors F_A (in green) and F_W (in orange), respectiely, against porosity. A law of the type $F = a \cdot \phi^{-m}$ is fitted on both datasets by taking into account all clay soils. Values of a and m coefficients are evaluated at 0.44 and 2.5 for Archie's law, and 3.0 and 1.0 for Waxman–Smits law. Determination coefficients of 0.93 and 0.18 are found for Archie's law and Waxman–Smits law, respectively. Figure from Carrière *et al.* (2018a). **b)** Variation of the critical shear stress τ_c measured during rheometric creep tests with the deviation of w from the Atterberg liquid limit, $w - LL$. The exponential law $\tau_c = 246.7\mathrm{e}^{-0.034(w-LL)}$ fits the data with a determination coefficient of 0.9. Figure from Carrière *et al.* (2018b).

rear of the main headscarp in August 2016, on both sides of a developing fracture delineating a block with a volume of a few hundred cubic metres. For 4 months, they continuously recorded seismic ambient vibrations and microearthquakes until the block broke. Five seismic parameters were derived from the monitoring: the cumulative number of microearthquakes (CNe), the seismic energy (SE), the block resonance frequency (f_B), the relative variation in Rayleigh wave velocity (dV/V) deduced from noise cross-correlations between the two sensors and the associated correlation coefficient (CC).

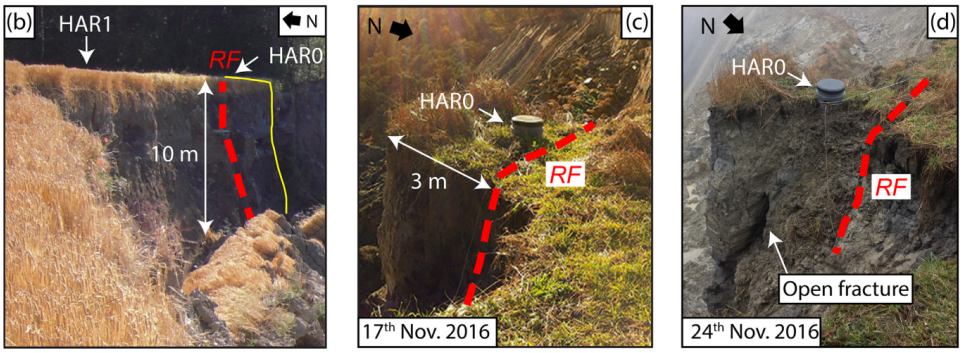

Figure 2.25 – Experimental setup at the headscarp of the Harmalière landslide (figure from Fiolleau *et al.*, 2020). **b)** West looking photograph of the headscarp and the slid block. The block position before sliding and the rear fracture (RF) are shown with yellow and dashed red lines, respectively. HAR0 and HAR1: seismic sensors. **c)** and **d)** East-looking photographs showing the clay block equipped with seismic sensor HAR0, on November 17th and 24th, respectively.

Despite the results being complex, they suggest the following sequence of events. At the beginning of the monitoring period, the block was already partially decoupled from the clay mass by a rear fracture, as attested by in situ observations and the measurement of a resonance frequency with a bending mode. The upper part of the fracture may be filled by air or soft clay, depending on weather conditions (dry or wet). Since the resonance frequency f_B did not decrease during the monitoring period, it is assumed that the block remained attached to the

stable cliff by a clay bridge, in agreement with the results of a numerical modelling experiment. Until October 13, the steady seismic activity indicated a continuous mechanical degradation along the headscarp, generating microruptures. The block remained stable and no significant variations in dV/V and CC, or decrease in f_B, were recorded, suggesting little or no variations in the medium between sensors and in the block characteristics (internal rigidity, fracture depth, contact rigidity). After a 70 mm rainfall on October 13–14, the upper medium between stations changed, as evidenced by the dV/V fluctuations and the CC decrease for the highest frequencies considered in the study (around 10 Hz). This medium change also affected the HN0/HN1 ratio amplitude (ratio of North components of stations HAR0 and HAR1), suggesting that it occurred in the block or at the contact between the block and the rear clayey mass. In contrast, the seismic activity remained steady, indicating that the block was still stable.

On October 25, the seismic activity increased after high precipitations (22 mm) that also caused low variations in dV/V and a significant drop in CC (< 0.5). This time is interpreted as the start of the block sliding process. After this date, each subsequent rainfall induced amplified variations of CNe, dV/V and CC until rupture, but seismic energy (SE) did not increase significantly until after November 22. This increase of the seismic energy could result from the sliding of the neighbouring blocks and/or the deepening of the lower fracture at depth, as suggested in the November 24 photo (Fig 2.25d). The general trend of f_B does not seem to be affected by these processes, but it should be noted that rainfalls generally coincide with increases in f_B with a much larger amplitude than those observed in the preceding period. However, the high number of seismic events may also influence the determination of f_B values, due to the shift of spectral energy to a higher frequency during events. On November 25, the drop in f_B indicates a major change at the interface between the block and the soil mass that occurred one hour before collapse. It can be interpreted as the onset of final block destabilization.

Of particular interest are the strong f_B variations with rainfalls observed during the monitoring period. For three rainfalls (20/08/2016, 17/09/2016 and 01/10/2016), f_B increases for about 2–3 days. At first sight, such observations are unexpected, since an increase in water content should increase density and decrease shear modulus, both yielding a reduction of f_B and V_S (Voisin *et al.*, 2016). However, f_B is negatively correlated to temperature and rainfalls that lower temperature can cause increases in fB. However, it is unlikely that such strong variations are generated solely by thermal effects. One possible explanation is that rainfalls temporarily change the contact between the block and the mass, that is that the fracture could close and re-open with the precipitation-induced swelling and shrinking of the clay in the upper medium. On November 6, a sharp increase in f_B was concomitant to an increase in seismic activity. A detailed analysis of the data points out that the microseismicity initiation and the f_B increase precedes the day's rainfall, highlighting the effect of seismic events on f_B. Finally, seismic energy increased considerably a few days before the block slipped and appears to be a robust precursor to the rupture.

In conclusion, this study has shown the value of seismic monitoring for tracking ruptures in clayey landslides. Unlike unstable rock columns (Lévy *et al.*, 2010), no precursory decrease in natural frequency was observable over the few weeks preceding rupture, probably due to the presence of a shallow clay bridge. In contrast, the seismic activity and energy, the Rayleigh wave velocity variations dV/V and the correlation coefficient CC showed precursory patterns that could be exploited. In particular, the progressive decrease in CC from high to low frequency is remarkable. However, as highlighted by different authors (Hilloulin *et al.*, 2014; Larose *et al.*, 2015b), the correlation coefficient can be influenced by various factors, and its robustness for monitoring purposes needs to be further investigated. Reversible variations in seismic parameters (f_B, dV/V and CC) appear to be complex and are not fully understood at this stage, like the increase in f_B with temperature. An interpretation of these effects and the understanding

of the rupture mechanism would require the measurement of hydraulic data at different depths and specific laboratory tests investigating the thermomechanical behaviour of the clay.

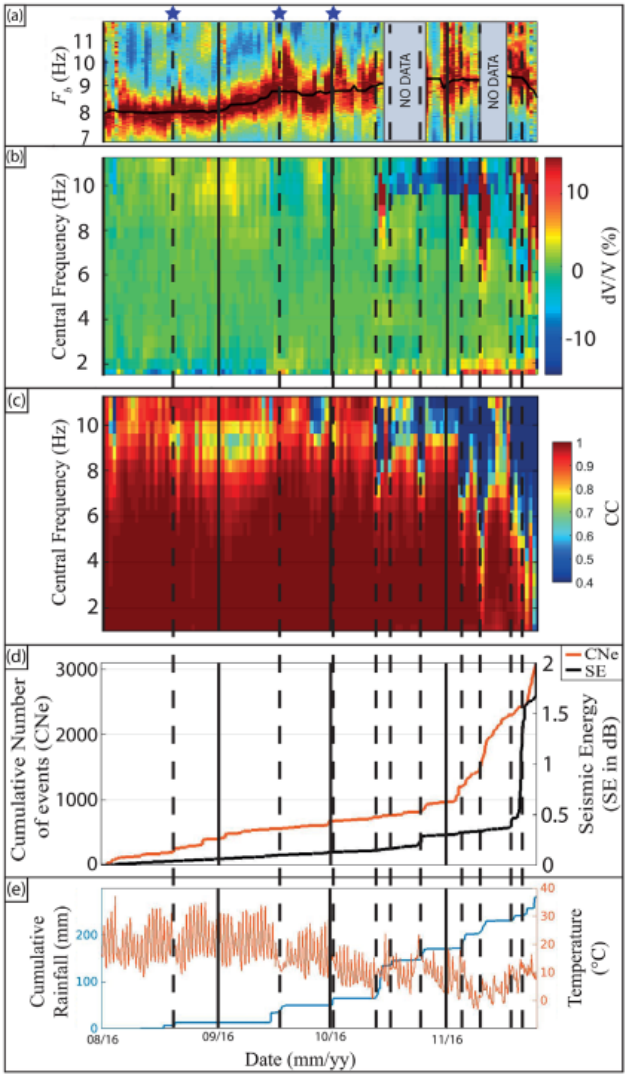

Figure 2.26 – Summary figure showing the evolution of the five seismic parameters studied at the headscarp of the Harmalière landslide (Fiolleau *et al.*, 2020). **a)** Normalized HN0/HN1 ratio analysis zoomed in the frequency band 7–12 Hz. The stars show the precipitation events that coincide with increases in resonance frequency f_B. **b)** Rayleigh wave velocity variation (dV/V) between 1 and 12 Hz. **c)** Correlation coefficient (CC). **d)** Cumulative number of microearthquakes (CNe, red curve) and the cumulative seismic energy (SE, black curve). **e)** Temperature and cumulative rainfall. The dashed black lines highlight the main rain events.

2.3 Perspectives

In the short and mid-term, my perspectives of research on landslides fit those of team GRE, which were recently defined for the period 2020-2024. The main questions concern the dynamics of damaging and rupture in landslides: which processes and mechanisms? which proxies? and which monitoring systems? In the following, these points are exposed separately but it should be noted that they are intricate.

2.3.1 Which imaging approaches?

Slow-moving landslides can be up to more than several km^2 in surface and thus generally prevent performing 3D ERT tomography to image the entire structure with a satisfactory resolution.

Recent applications and developments have shown the ability of ERT to image such structures in 3D to provide a global image of the geological setting (Lajaunie *et al.*, 2019) and 4D to monitor the evolution with time (Uhlemann *et al.*, 2017; Bièvre *et al.*, 2021). However, and due to the relatively low number of sensors considering the surfaces to be investigated, this approach appears not suited to detect layers some metres-thick over areas several hundreds to thousands of m^2. Moreover, landslides often exhibit complex topography along with difficulty to access some parts, e.g. densely vegetated or strongly disrupted, which prevent from conducting resistivity measurements using classical techniques by deploying electrodes and cables in the field.

There are several ways to overcome this issue. First, individual inverted profiles can be represented in 3D under the form of fence diagrams (Bichler *et al.*, 2004; Schmutz *et al.*, 2009). Second, it is possible to perform 2D measurements and gather them into a full 3D inversion (Udphuay *et al.*, 2011; Bièvre *et al.*, 2021). Such an example is presented in figure 2.27a, where 8 individual 2D profiles were gathered to perform a 3D inversion over the Charlaix landslide (details on the study site can be found in Bièvre *et al.*, 2018b). The different horizons are made of laminated clays ($\rho < 50\,\Omega$.m) or coarser deposits (moraines, lacustrine sand and gravels ; see Fig. 2.16) with resistivity $> 150\,\Omega$.m. These values are retrieved along individual 2D profiles (Fig. 2.27b). However, where no measurements are available, the resistivity is around 80-100 Ω.m (in green in Fig. 2.27a), which does not correspond to any known horizon on site. It corresponds actually to the average apparent resistivity that was used as a starting value in the homogeneous model for inversion.

One possibility to add constraint is to obtain resistivity data where it is not possible to perform classical resistivity measurements (such as Vertical Electrical Sounding or imaging). This can be achieved using Electromagnetic Induction (EMI) prospecting. These two methods are classically employed together in environmental, geotechnical and landslide studies (Meric *et al.*, 2005; Poisson *et al.*, 2009; Schmutz *et al.*, 2009; Dumont *et al.*, 2017). Using versatile codes such as the pyGIMLI package (Rücker *et al.*, 2017) allows combining methods (e.g. direct-current resistivity and frequency-domain electromagnetics) and incorporating point data (e.g. borehole) into a single inversion. This work was initiated very recently (late 2021) and is conducted in collaboration with T. Günther from LIAG Hannover, Germany.

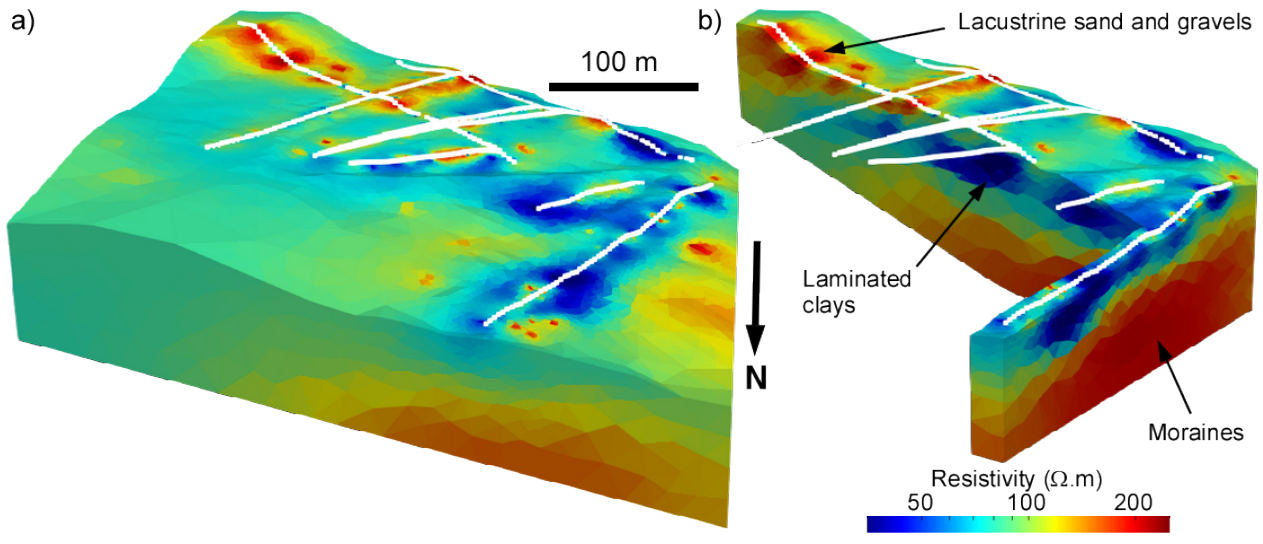

Figure 2.27 – 3D ERT image of the Charlaix landslide using a combination of 8, 2D profiles. White dots denote electrodes. **a)** 3D image. **b)** 3D image clipped along selected 2D profiles.

2.3.2 Which processes and mechanisms?

2.3.2.1 Reversible and irreversible deformations

In the case of gravitational instabilities, recent results at ISTerre have identified, particularly through continuous seismic measurements at several sites, reversible (elastic) and irreversible (plastic, damage, rupture) deformations (Mainsant *et al.*, 2012b; Bièvre *et al.*, 2018a; Fiolleau *et al.*, 2020; Colombero *et al.*, 2021). Elastic deformations show a strong dependence on external environmental forcing (temperature, rain and snowmelt). However, depending on the structures studied (instabilities in rocks, soils and soft rocks), geophysical responses to forcing can be reversed (Colombero *et al.*, 2021). This variability in geophysical response (site-specific?) is not yet understood. It will be investigated using the many time series available, ongoing experiments (observatory data, projects with instrumentation over several years ; cf. sections 2.3.2.2 and 2.3.4) but also controlled laboratory experiments and numerical simulation.

In addition, ongoing work shows that it is extremely complex to deconvolve the seismic time series of these elastic effects to keep only the information on the mechanical evolution of the studied structure. One of my objectives will be to develop mathematical processing techniques (signal processing, Artificial Intelligence) to deconvolve time series from these seasonal components. It will require collaborations with other researchers, notably specialized in signal processing. Also, a particular attention should be paid to the influence of this environmental forcing on the response of the studied structures (natural and/or anthropogenic) in the context of climate change (e.g. through long observatory/monitoring time series).

Finally, it was also sought to understand the mechanisms of the solid-fluid transition (sliding that evolves into flowing). To date, results have mainly focused on changes beyond the liquid limit (LL). In the future, my aim is to understand the mechanisms at work around LL and in particular to better characterize and monitor physical changes from the solid phase to fluidization. This component will require a multidisciplinary approach (among which both soil and fluid mechanics) and a particular attention will be paid to the interactions between subsurface fluids and existing minerals. It will also be necessary to develop original geophysical characterizing and monitoring approaches (seismic, electrical and/or electromagnetic; cf. section 2.3.4).

Since around ten years, it has been shown that shear-wave velocity Vs is a relevant parameter to monitor the evolution of clay stiffness (Renalier *et al.*, 2010a; Mainsant *et al.*, 2012b, 2015; Berti *et al.*, 2018, 2022) and the influence of seasonal parameters on its variation (Larose *et al.*, 2015a; Bièvre *et al.*, 2018a, 2021; Le Breton *et al.*, 2021). In the next few years, I would like to investigate the potential control of reversible deformation on the development of damaging, possibly up to failure. Several seismic, along with hydrometeorologic and displacement time-series originating from clayey landslides are available (e.g. OMIV time-series on the Avignonet landslide date back to more than 15 years) and some of them recorded failures (on the Harmalière landslide). Apart from investigating velocity variations from cross-correlation, the potential of intra-correlation, analysing the variation of surface wave ellipticity, will be evaluated using these available time-series. One can also consider using deep-learning techniques to detect tiny events associated with early stages of damaging. The detection of precursory events in seismic time series has been achieved using the correlation of reference events with continuous time series (template matching; Helmstetter & Garambois, 2010; Poli, 2017), or by Artificial Intelligence (AI) tools such as the Random Forest approach (Provost *et al.*, 2017; Wenner *et al.*, 2021), or clustering seismic signals with unsupervised deep learning (Seydoux *et al.*, 2020). These tools could help looking for low-amplitude signals in continuous seismic time series recorded on landslides.

For the spatial characterization *in situ*, a collaboration with team Waves & Structures (ISTerre,

P Roux and S Garambois) in the frame of project RESOLVE allowed to deploy 100 seismic sensors during 1 month in June 2021 and the spatial evolution with time of various parameters (e.g. Vs, dV/V) will be analyzed in parallel with environmental parameters (see section 2.3.4.2).

2.3.2.2 Control of the dynamics

On the Charlaix landslide, recent results showed a fast infiltration of water into the ground, with a faster reaction of the water table situated at 12 m depth above a shear surface compared to the phreatic water table at 7 m depth (Bièvre *et al.*, 2018b, section 2.2.2.1). A project granted by région Auvergne-Rhône-Alpes and Europe (POIA MLA3 ; PI CEREMA Lyon) allowed, among other, to set continuous instruments in the Charlaix landslide. Displacements down to 30 m depth are presently continuously monitored in 3D using rods equipped with accelerometers each 0.5 m. This system is completed by several piezometers set at different depths. A seismic and geodetic network made of 3 velocimeters and 3 GNSS stations was installed in Spring 2021 for 2 years (stations S1 to S3 in Fig 2.12). It will monitor the evolution of dV/V (changes in rigidity) and correlation coefficients (changes in coherency) in different frequency ranges (i.e. at different depths). Notably, it will now be possible to make detailed correlations between water infiltration and displacements at depth. More precisely, it will be possible to confirm previous results suggesting that water infiltrates more rapidly at depth (Bièvre *et al.*, 2018b) and to evaluate the influence of this infiltration on displacements at different depth ranges. Finally, these calibrated and direct data will also allow evaluating the ability of seismic noise cross-correlations to detect velocity changes that can effectively be attributed to hydromechanical changes within the landslide: is it possible to detect differential velocity variations as a function of depth?

Preliminary results are presented hereafter, with the location of the stations shown in Fig 2.28a. GNSS stations S3 and S2 (Figs 2.28b and 2.28c, respectively) show that S3 does not move, while S2, which is located inside the most active zone, experienced a planimetric displacement of $\sim$6.5 cm towards north-west in 2021. The location of the stations appears then suited to study the evolution of geophysical parameters inside (S2) and immediately outside (S1 and S3) the most active zone.

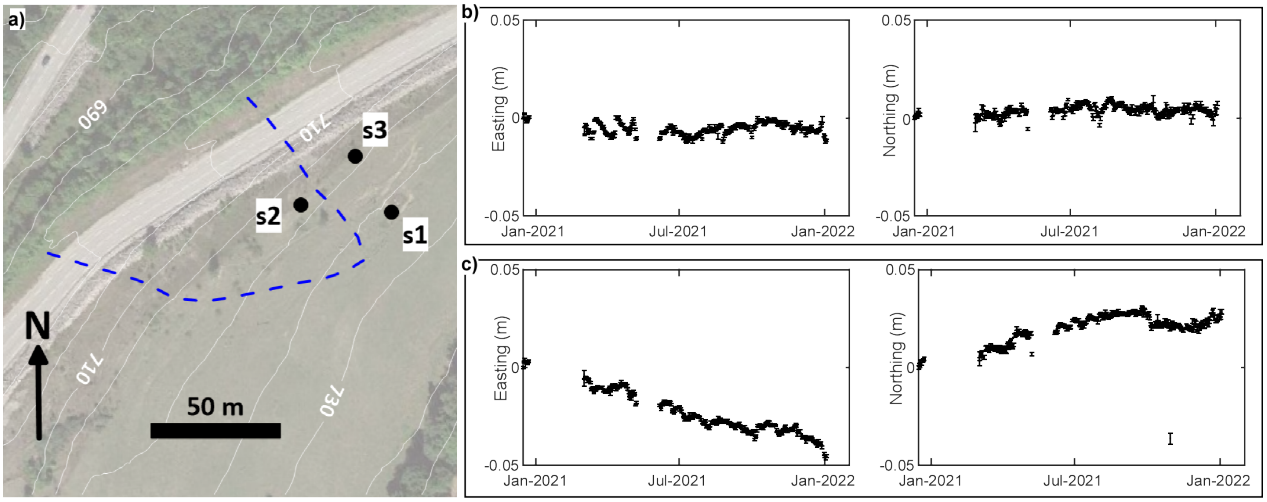

Figure 2.28 – Continuous GNSS measurements on the Charlaix landslide. **a)** Location of GNSS and seismic stations S1 to S3. GNSS times-series of stations **b)** S3 and **c)** S2.

Figure 2.29 shows daily correlograms of pairs S1-S3 (left) and S1-S2 (right). Daily seismic time series of vertical components were whitened, filtered (Butterworth filter in the range 4-15 Hz), and then cross-correlated with reference to station S1. Very briefly, both correlograms

show consistent phases since the beginning with strong amplitudes for negative lags (*i.e.* waves propagating from S2 and S3 to S1). For S1-S2, coefficients of correlation are lower (not visible in the figure since they were normalized for identifying phases), suggesting a lower coherency than for S1-S3. This is in agreement with previous observations suggesting that S2 is located in an active zone enduring deformation. In the future, these seismic time-series will be translated into dV/V time series and compared to hydrometeorological and deformation time series measured at the surface but also at depth. The interest of other seismic parameters for landslide monitoring, such as Rayleigh wave ellipticity (from intra-correlation) and H/V variations with time will also be explored.

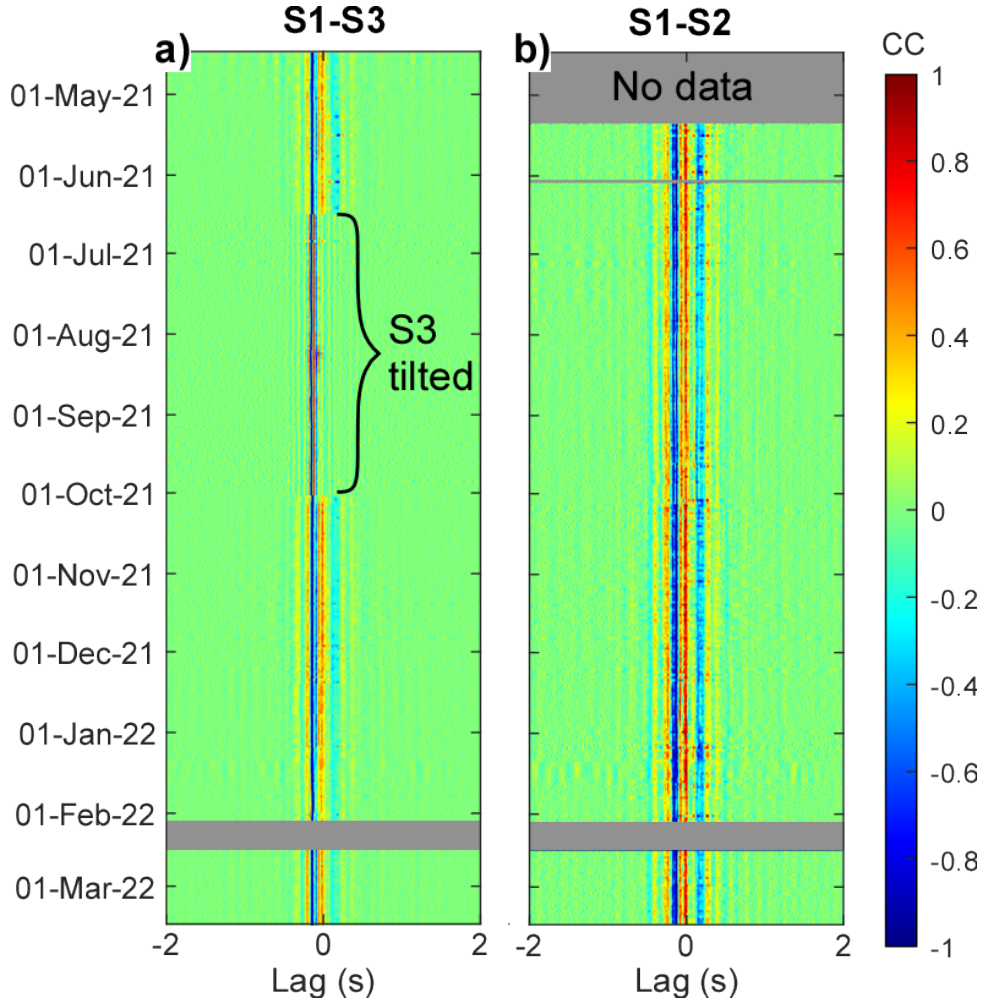

Figure 2.29 – Daily normalized correlograms of Charlaix seismic stations (vertical component). **a)** S1-S3 **b)** S1-S2.

2.3.3 Which proxies?

In the last decade, *in situ* instrumentation efforts have provided several multi-parameter time series (geophysics, displacements, etc.) until failure (e.g. Mainsant *et al.*, 2012b; Fiolleau *et al.*, 2020). These unique data show the existence of several asynchronous precursory seismic parameters (a few weeks to a few hours): microseismicity, resonance frequency, variation in surface wave velocity and correlation coefficient (Fiolleau *et al.*, 2020). In the future, I would like to focus in particular on the physical understanding of the temporal hierarchization/succession of these precursors and their relationship to the damage and disruption phases. The ultimate objective will be to be able to propose the use of all these parameters and a controlled instrumentation methodology for the monitoring of instability with stakes. To carry out this research,

high-quality time series until failure (not necessarily long or with many sensors) or without failure but with progressive damaging will be necessary.

2.3.4 Which monitoring systems?

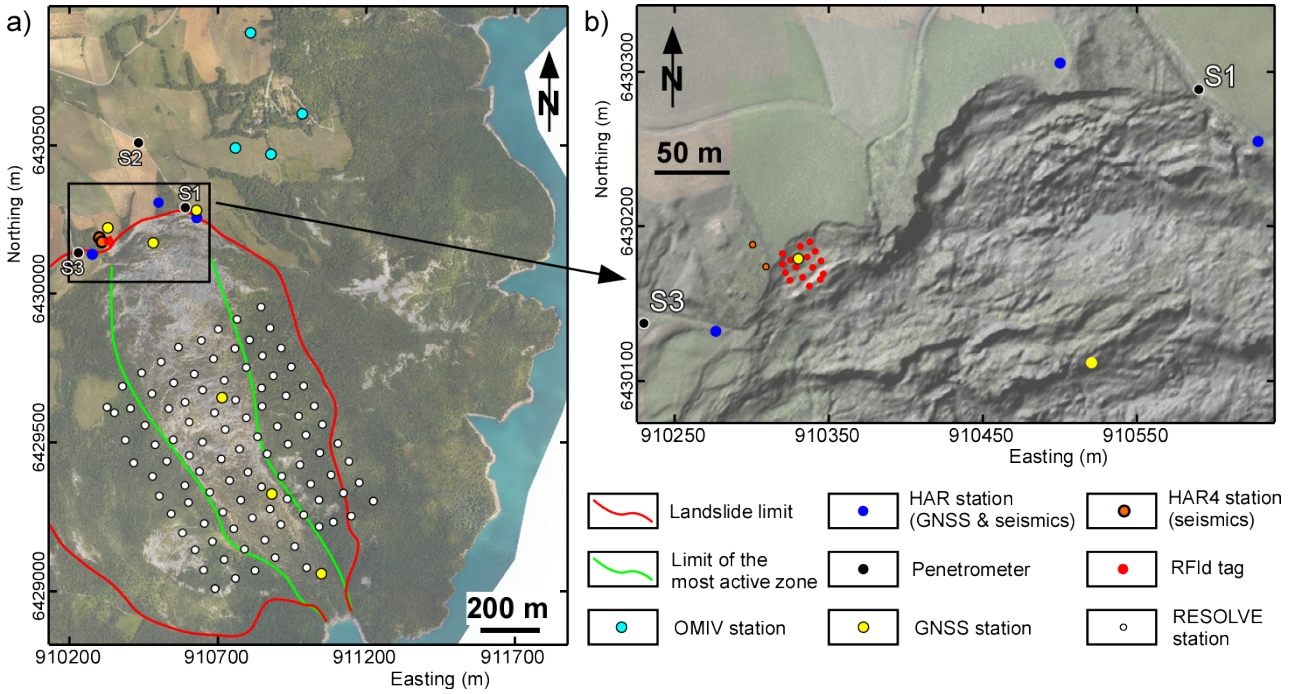

Figure 2.30 – Location of experiments on the Harmalière and Avignonet landslides. **a)** General view of the sensors deployed over the two landslides. **b)** Close-up on the headscarp of the Harmalière landslide.

2.3.4.1 Continuous monotoring of electrical resistivity and induced polarization

During the last decade, works carried out at ISTerre have shown the possibility of detecting geophysical signals precursory to the fluidization of the Pont-Bourquin landslide and its evolution into a flow (Mainsant *et al.*, 2012b, 2015), or to the rupture of a clay block within the Harmalière landslide (Fiolleau *et al.*, 2020). Similarly, temporal monitoring of these unstable masses showed a periodic and reversible influence of environmental parameters on geophysical parameters such as shear-wave velocity V_S and electrical resistivity ρ (Bièvre *et al.*, 2018a, 2021). These methods thus appear suitable for monitoring these sliding masses, and more particularly to try to understand the initiation of degradation up to failure. Internationally, the electrical monitoring of such structures is carried out exhaustively, notably by the British Geological Survey on the Hollin Hill clay flow-slide in northern England. The results of 4-year monitoring of the electrical resistance (Merritt *et al.*, 2018) or the water content deduced from the resistivity (Uhlemann *et al.*, 2017) highlights the hydrological control of the landslide activity, accordingly to similar results obtained at the Pont-Bourquin site (Bièvre *et al.*, 2018a, 2021). Moreover, recent studies by other teams have shown that induced polarization, measurable at the same time as resistivity, provides additional information to resistivity for the interpretation of water infiltration and circulation mechanisms in landslides (Gallistl *et al.*, 2018; Revil *et al.*, 2020).

The Harmalière landslide has been continuously instrumented since its reactivation in late June 2016 ($\sim 1 \times 10^6\,\mathrm{m}^3$). This earthslide is immediately adjacent to the Avignonet landslide, instrumented since 2006 as part of the multidisciplinary observatory on versant instabilities (OMIV). The instrumentation is shown in figure 2.30. Three GNSS and seismic stations have been positioned at the rear of the headscarp (blue dots labelled "HAR station"). Six "low-cost"

GNSS stations have since been added (yellow dots labelled "GNSS station"), 4 of which are in the landslide. This instrumentation completes the one in place since 2006 on the Avignonet landslide ("OMIV station" in figure 2.30a).

On the Harmalière landslide, an INSU-Tellus project in 2019 allowed to identify, characterize and instrument a horizon with weak mechanical characteristics located immediately behind the headscarp. Reconnaissance works included penetrometer tests at three locations (S1 to S3 in Figure 2.30a). All the tests detected a horizon showing weak mechanical resistance to penetration Rd (< 5 MPa) between 2.5 and 5.5 m depth (Fig 2.31). However, only the tests immediately behind the headscarp (S1 and S3) showed low to null values (illustrated by Rd values of 0.1 MPa). Measurements at S1 and S3 were repeated at different seasons. Results show that this particular horizon changes with time (location at depth and also its mechanical characteristics). Finally, two interstitial pressure/temperature/electrical resistivity sensors were installed at S1, one open and one confined into this particular horizon. The time series (not presented here) shows that there is little change in pore pressure and electrical resistivity in the confined horizon, suggesting that the water is contained in a semi-captive, low-permeability aquifer. The results also show a decreasing annual recharge of the water table since 2018. This particular horizon could thus correspond to the development of a retrogressive surface in saturated to unsaturated clay. Periodic seismic and electrical (resistivity and induced polarization) measurements carried out as part of the Tellus 2019 project, located close to S1, did not reveal this variability, in particular, due to a sensor configuration that is poorly suited to monitoring such a horizon (low sensitivity).

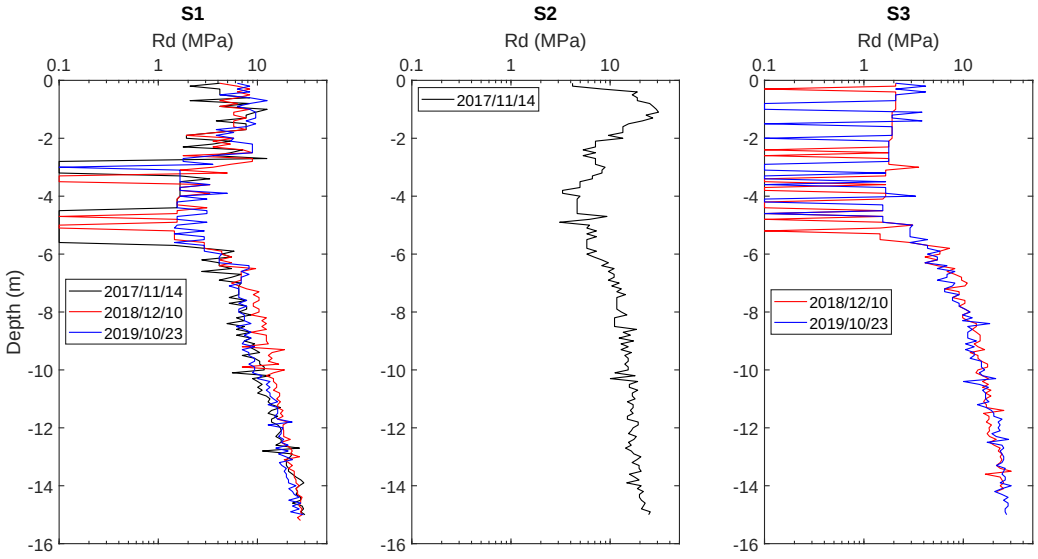

Figure 2.31 – Penetrometer tests at the rear of the Harmalière headscarp (location in Fig 2.30).

On the other hand, a major difficulty in the temporal monitoring of these unstable masses is the potential destruction of the measurement systems during the reactivation of the landslides or their evolution into a flow. One possibility is to use reliable and inexpensive systems, with remote data transmission, whose destruction would not prevent the site from being re-equipped. Such systems exist for geodetic measurements and have been successfully tested for landslide monitoring: displacement measurements with RFId tags (Le Breton *et al.*, 2019) or "low-cost" GNSS stations such as the GEOMON system developed by Infrasurvey in Switzerland (Fiolleau *et al.*, 2021). An electrical system (OhmPi) for measuring electrical resistivity, based on the concept of being low-cost and open source, has recently been proposed (Clément *et al.*, 2020). This resistivity meter with 32 to 128 electrodes, initially intended for laboratory use, will be adapted to be deployed on the landslide near S1 in the frame of a project granted by

LabEx OSUG and INSU. Technical developments will include energetic autonomy and wireless communication. Two rods containing the electrodes will be developed and set up in the field to allow for cross-borehole tomography. Finally, an algorithm to process Induced Polarization measurements "in the on-time" (Olsson *et al.*, 2015) from the full-waveform signals will be developed and integrated into the daily measurements.

The technical objective of the project is to develop a low-cost, autonomous resistivity meter adapted to the monitoring of horizons of weak mechanical characteristics at the rear of the Harmalière headscarp. The scientific objective is to understand the retrogression mechanism of the landslide and, more precisely, the development of shear surfaces at depth in relationship with cracks at surface at the rear of the headscarp (see "?" in Fig 2.13). What is the controlling factor of the initation and of the location of new shear surfaces at the rear of headscarps ? As the characteristics of these zones vary according to the seasonal and hydrogeological conditions, monitoring by high-resolution electrical tomography seems well suited to following fluctuations in the water content and possibly the porosity of the material. The results will be compared with displacements monitored by the GNSS and RFId networks. Complimentary, passive seismic monitoring will be conducted (HAR4 stations in Fig 2.30b) and will provide mechanical observation at the rear of the headscarp from the cross-correlation of continuous seismic measurements.

2.3.4.2 Dense seismic arrays: the RESOLVE-HAR experiment

The slow-moving Harmalière landslide presents multiple deformation mechanisms, with brittle deformation at the headscarp, ductile deformation along several shear surfaces in its upper part and, finally, a flow-like behaviour at the toe (Fiolleau *et al.*, 2021, Fig 2.32). The transition between solid (slide) and fluid (flow) behaviours is distributed along a several hectometres-long transition zone. The extension of this zone and the mechanism of the transition between slide and flow-like deformation remains difficult to assess.

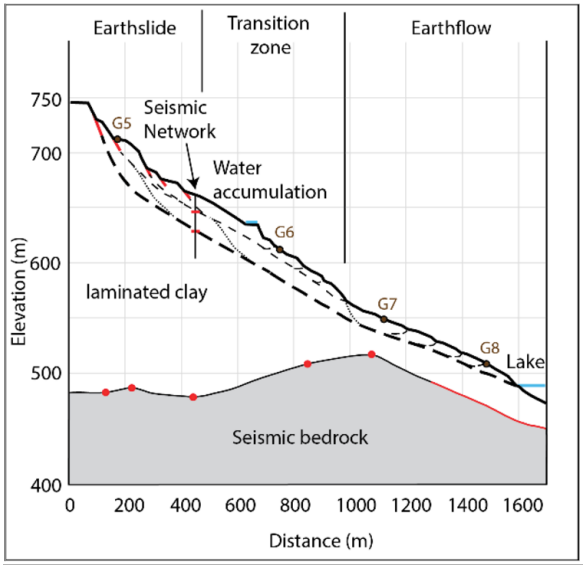

Figure 2.32 – Interpretative cross-section of the Harmalière landslide from the topography extracted from the LiDAR DEM acquired in November 2019 (Fiolleau *et al.*, 2021). Red dots: bedrock top (Jurassic carbonates plus cemented palaeoterrace) from H/V measurements refined from Bièvre *et al.* (2011). The red part of the bedrock corresponds to the 1950 topography. Red bars: constraints on the scarps and shear surface deduced from the seismic network. The shallow and deep slip surfaces are represented by fine and bold dotted lines, respectively. The connections between the two slip surfaces are schematic (dotted line).

The RESOLVE project (High-resolution imaging in subsurface geophysics: Development of a

multi-instrument platform for interdisciplinary research ; PI: P Roux, ISTerre) aims at developing 4D acquisition using a very dense array of autonomous and wireless sensors. These dense arrays have shown their ability to characterize seismic sources in fault zones (Gradon *et al.*, 2021), or the structure of earthflows (Thomas *et al.*, 2020). On the Harmalière landslide, 100 velocimeters were installed for 1 month over the transition zone in late spring 2021 (Fig 2.30). Several outcomes are attended. First, 3D images (both P and S wave velocity) of the most active zone will be built. The seismic contrast between the different clayey units and the seismic bedrock is large enough to allow distinguishing them (Renalier *et al.*, 2010b; Fiolleau *et al.*, 2021). Second, the 3D shear-wave velocity image will provide the continuous evolution of V_S in the transition zone and will give insight into the evolution from a slide to a flow. Third, catalogues of the micro-seismic activity will be built. They will provide the opportunity to potentially localize the (micro-)seismic activity in the landslide: is it localized along preferential paths (shear surfaces) which would correspond to a slide or is it distributed randomly in the landslide, which would suggest a flow mechanism? Numerous other approaches are also to investigate, such as the temporal and spatial evolution of the H/V ratio and its relevance for landslide monitoring. This last point will require a collaboration with members of team GRE, specialists of H/V measurements and processing.

3 Earth dams

The second research theme that I would like to expose here concerns the characterization of water flows in porous media using geophysical methods. More specifically, I am interested in the problem of locating and monitoring leaks in earth dams (or earth dykes). This is a theme I started to work on when I took up my position at the Centre d'Études Techniques de l'Équipement (CETE, now CEREMA) in the 2000s (Bièvre & Norgeot, 2005; Bièvre, 2007b) and that I have been pursuing ever since. Following my arrival at ISTerre, I was able to develop the use of advanced calculation, modelling and inversion methods that allowed obtaining original results (and to deepen results obtained when I was still working at CETE/CEREMA). This was achieved within the frame of an IFSTTAR/CEREMA research program labelled DOFEAS and also through a PhD (Maalouf, 2021).

Notably, on a canal earth dam located in the centre of France, it was possible to detect and locate a leak located a few meters below the surface using surface-guided background noise measurements and by adapting an initially developed algorithm for locating avalanches. On the same dam, it was also possible to develop a methodology for correcting the 3D geometric effects that affect the 2D electrically driven summer resistivity measurements. This methodology can be applied to any object and has been used to correct some 3D effects in the study of unstable rock cliffs on the shores of the Como lake in Italy (Arosio *et al.*, 2019). This work on earth dykes is ongoing and I am collaborating with other researchers and laboratories (e.g. Fargier *et al.*, 2019).

3.1 Introduction

Earth-filled canal embankments play several functions. Their role is to ensure shipping, water transport and water storage. Depending on their degree of impermeability, these dykes contain a more or less permanent hydraulic head. As such, they are prone to internal erosion phenomena, such as leakage and piping, which may lead to breaching (Foster *et al.*, 2000; Fell *et al.*, 2003).

The internal erosion and piping processes are described by different stages (further description from Maalouf *et al.*, 2022), the relative duration of which is unknown, as illustrated in figure 3.1. The first stage, called initiation, is either related to the development of a concentrated leak, suffusion or backward erosion (Van Beek *et al.*, 2013; ICOLD, 2017). The second stage of internal erosion is called continuation. In this stage, internal erosion can be stopped if the filters are properly designed to prevent the washout of fine materials ; otherwise, internal erosion will proceed to stage 3, called progression (Foster *et al.*, 2000). It corresponds to the formation of a pipe in the body of the dam. Once the pipe is created, the internal erosion process accelerates up to the failure (stage 4 ; Fell *et al.*, 2003). The potential loss of lives caused by the failure of a dam relies mostly on the warning time given to evacuate areas at risk at the downstream of the dam (Fell *et al.*, 2003). For example, around 20 years ago, the United States Bureau of Reclamation recommended that the warning time of failure be of a minimum of 60 minutes

in order to save lives (Graham, 1999). According to Fell *et al.* (2015), internal erosion is more likely to be detected in the advanced stages of progression and breach formation (i.e. late stage 3 and stage 4). Hence, it appears crucial to detect as early as possible an ongoing internal erosion process and identify its current stage (1,2 or 3).

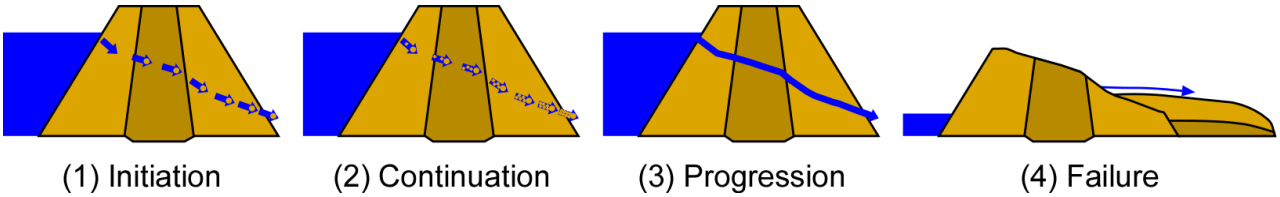

Figure 3.1 – The different stages of internal erosion in the backward erosion type (Maalouf *et al.*, 2022). (1) Initiation, when the first soil particle is driven downstream. (2) Continuation, when additional soil particles are washed away. (3) Progression is the formation of the pipe in the embankment. (4) The breach represents the complete failure of a part of the dam and allows the water to flow out of the reservoir.

Furthermore, these structures might be older than several tens (and sometimes hundreds) of years (Fig 3.2) with very few available geotechnical data.

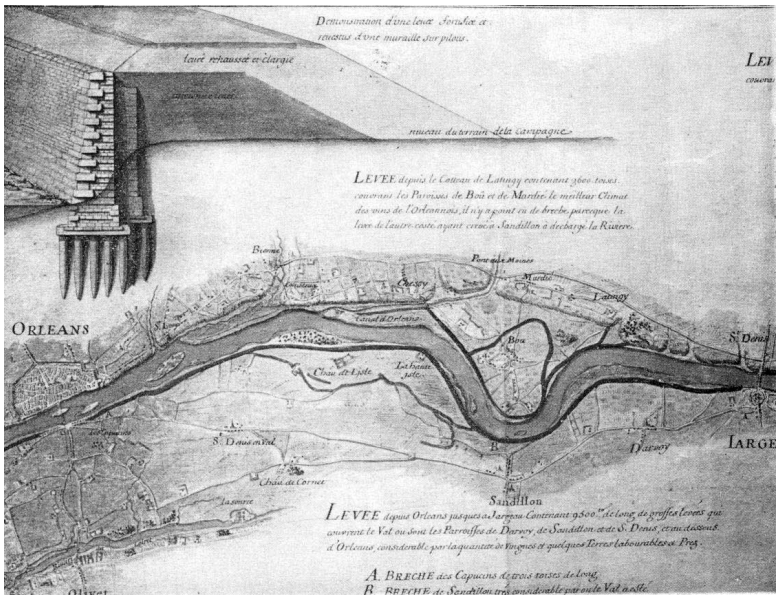

Figure 3.2 – Map and design of existing earth dams to be elevated in the early 1700s following a flood of the Loire river near Orléans, France, in 1709 (Dion, 1961).

Finally, these linear infrastructures may be stretched over up to several thousands of km per country (e.g. 9000 km of embankments in France according to the French Association of Embankments Managers; france-digues.fr). As such, rapid and cost-effective methods are needed to assess the geotechnical conditions of these structures, locate heterogeneous and/or weak zones, and optimize the location of geotechnical prospecting (drilling and in situ tests; Fig 3.3).

As in the case of landslides, the first geophysical works on earth dams and reservoirs were reported in the late 1960s and early 1970s (Ogilvy *et al.*, 1969; Bogoslovsky & Ogilvy, 1970a,b). Due to technological improvements in the past decades, geophysical methods have been increasingly used to assess the geotechnical and hydrogeological setting of earth dykes starting from the late 1990s/early 2000s. These methods were used to characterize both the internal architecture of dykes (geometry, lateral variations, etc.) and to try to localize specific anomalies such as internal erosion pipes and water leakage. To achieve first qualitative zoning, in terms of architecture and geometry, it is generally recommended to apply first rapid and high output/efficiency methods such as Slingram and/or Airborne ElectroMagnetic (AEM) induction

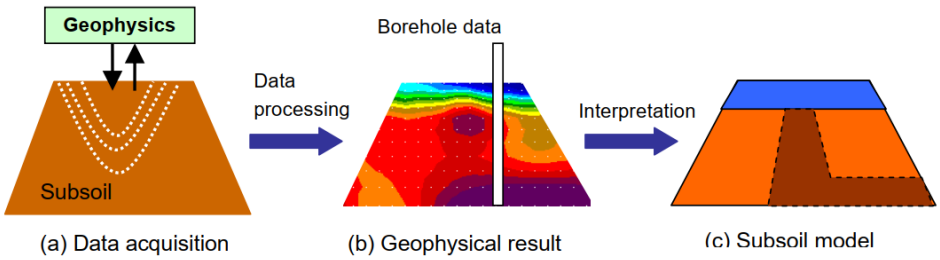

Figure 3.3 – General scheme of a geophysical investigation process of an earth dyke (Royet *et al.*, 2013). **a)** Geophysical data acquisition. **b)** geophysical parameter graph, map or cross-section with additional borehole data. **c)** subsoil structure model or geotechnical property distribution.

techniques (Fauchard & Mériaux, 2007; Royet *et al.*, 2013). When heterogeneous/anomalous zones are detected, quantitative (and more punctual) imaging techniques are then applied to try to locate in two dimensions (2D) defaults within the dyke (Fauchard & Mériaux, 2007; Niederleithinger *et al.*, 2012). These methods classically encompass electrical resistivity tomography (ERT), seismic refraction (SR), multi-channel analysis of surface waves (MASW) and ground-penetrating radar (GPR). Among all geophysical techniques, ERT is commonly used to characterize dykes. It has been applied to image the depth to the substratum and its lateral variation (Cardarelli *et al.*, 2010; Minsley *et al.*, 2011; Cardarelli *et al.*, 2014) as well as the internal variations or structures of dykes (Weller *et al.*, 2006; Cho & Yeom, 2007). Time-lapse ERT has also been successfully used to image the internal evolution of dykes and to detect leakage and seepage path (Sjödahl *et al.*, 2008, 2009; Weller *et al.*, 2014).

Seismic methods have been less used to characterize earth embankments. P-wave velocity (V_P) is highly sensitive to the water content and hence preferentially detects the water table within the dyke body (Ikard *et al.*, 2015). Using P-wave refraction over a non-saturated earth dam, Kim *et al.* (2007) were able to locate low-velocity zones, which they associated to previously identified seepage entry path zones. P-wave refraction and/or tomography was also found to be adapted to locate the depth to the bedrock (Cardarelli *et al.*, 2010). S-waves are less sensitive than P-waves to the presence of water. They also have the advantage of offering a better resolution than P-waves. S-wave velocity (V_S) imaging has however been poorly reported. This might be linked to the difficulty of generating energetic S-waves which results in a poor signal-to-noise ratio (SNR). Cardarelli *et al.* (2014) conducted both P- and S-waves tomography on an earth-filled dam which allowed them to evaluate the Poisson coefficient of the soil. Surface waves (SW) inversion has been recently applied for dyke characterization (Cardarelli *et al.*, 2010, 2014). It has been used preferentially to V_S imaging to retrieve vertical V_S profiles. Rayleigh waves offer the advantage of being recorded at the same time as P-waves, provided geophones with a sufficiently low cut-off frequency are used (Socco & Strobbia, 2004; Foti *et al.*, 2018). SW inversion provides 1D V_S profiles where V_S varies only as a function of depth. The gathering of several 1D profiles spread along the dyke might allow an interpretation in terms of pseudo-2D V_S image. However, the 1D assumption might not be respected on dykes, considering the complex surface morphology of these structures when compared with a flat half-space. Karl *et al.* (2011) studied numerically these effects using a 2.5D approach and concluded that they were insignificant for dykes with a base width-to-height ratio larger than four. One can note that, however, such geometries are rare in the case of small earth dams which generally have ratios of up to 4.

Recently, the application of seismic ambient noise monitoring to a controlled laboratory-scale experiment and an in situ experiment allowed Planès *et al.* (2016) to detect significant velocity variations (a drop by around 20 %) which they attributed to a piping process developing through a dam. Other techniques, such as acoustic emissions localization have been employed to localize

leakages, using hydrophones (Bolève *et al.*, 2012) or geophones on the dyke (Rittgers *et al.*, 2015).

3.2 Achievements

The works I conducted on earth dams were manifold. The first objective, exposed in section 3.2.1, was to evaluate and compare the results obtained with classical active geophysical methods (SR, first arrivals tomography and ERT) to characterize the geometry of a small (a few metres in height and width) earth-filled dyke with a permanent hydraulic head. Even if the combination of different geophysical parameters is generally recommended for site investigations, it is rarely done in the case of earth dykes. The combined interpretation of geophysical data along with numerous geotechnical data revealed that ERT and surface waves are strongly affected by 3D effects. A method was developed to correct artifacts affecting ERT measurements (section 3.2.1.1). For surface waves, artifacts were mainly evidenced (section 3.2.1.2) and works to better understand them are part of my perspectives.

The second objective was to test the ability of ambient vibration methods to localize leakage zones inside an existing earth dam. This test was not first designed to process ambient vibrations however, it provided promising results that allowed to localize the leakage zone at depth. These results are exposed in section 3.2.2. However, this localization was possible because of an energetic water flow in the dyke, highlighting an advanced stage of internal erosion.

The third objective of these works was to evaluate the ability of geophysical methods to detect early stages of internal erosion. For this, controlled laboratory experiments were developed and geophysical parameters (ambient vibrations and electrical resistivity) were monitored during internal erosion leading to failure. Results are exposed in section 3.2.3 and originate from Y Maalouf's PhD (Maalouf, 2021).

3.2.1 The complex geometry of earth dams leads to geophysical artifacts

This specific work aimed at investigating the combined use of extensive geotechnical, hydrogeological and geophysical techniques to assess a small earth dyke with a permanent hydraulic head, namely a canal embankment. The experimental site is the 56 km-long "Canal de Roanne à Digoin". It was built during the first half of the 19th century between 1830 and 1836. Its role is to ensure both shipping (freight and tourism) and water feeding to the "canal latéral à la Loire", a 200 km-long canal which allows skipping shipping on the Loire river, subject to floods and droughts (Fig 3.4a). In the study area, the dyke is made of a heterogeneous mixture of clays, silts, sands and gravels. It relies upon Jurassic marly limestones (Fig 3.4b), the top of which is supposedly more or less weathered and decalcified. The dyke imperviousness is ensured by a concrete facing at the base of the canal. From a geometrical point of view, the dyke is 4 m wide on top and 18 m wide at its base, with a maximum height of 10 m. This corresponds to a base width-to-height ratio of around 1.8. The lateral slopes are 33° (3 horizontal units per 2 vertical units). An intermediate berm, towards the east and located between 1.5 m and 3 m below the dyke crest, serves as a road.

The dyke was chosen because of known issues concerning m-long breach occurred in 2007 (Fig 3.4c) 1.5 km south of the study site, which supposedly originated from internal erosion phenomena. The study site was chosen because two leakages were visually observed at the toe of the dyke and also on the inside of the canal following its emptying before remediation works. Geotechnical prospecting was conducted using drilling, coring, permeability and penetrometer

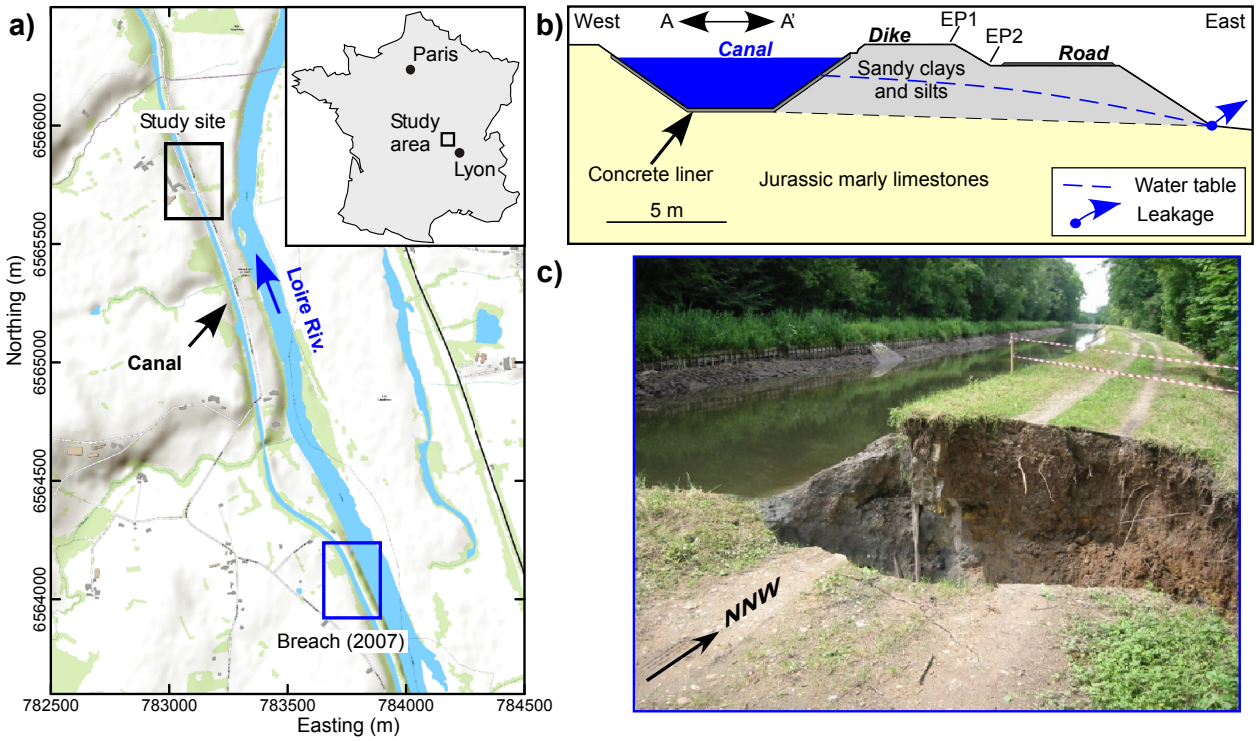

Figure 3.4 – Location and geotechnical context of the study area. **a)** Geographical location of the study site and of the breach which occurred in 2007. The topographic map comes from the ArcGis world imagery repository. Units are expressed in the Lambert93 French system. **b)** Schematic geotechnical cross-section of the dyke at the study site (location in Fig 3.4a). **c)** Photograph of the breach which occurred in 2007 (location in Fig 3.4a).

tests (Fig 3.5). Geophysical prospecting was conducted with ERT, SR tomography (P and SH waves) and MASW inversion.

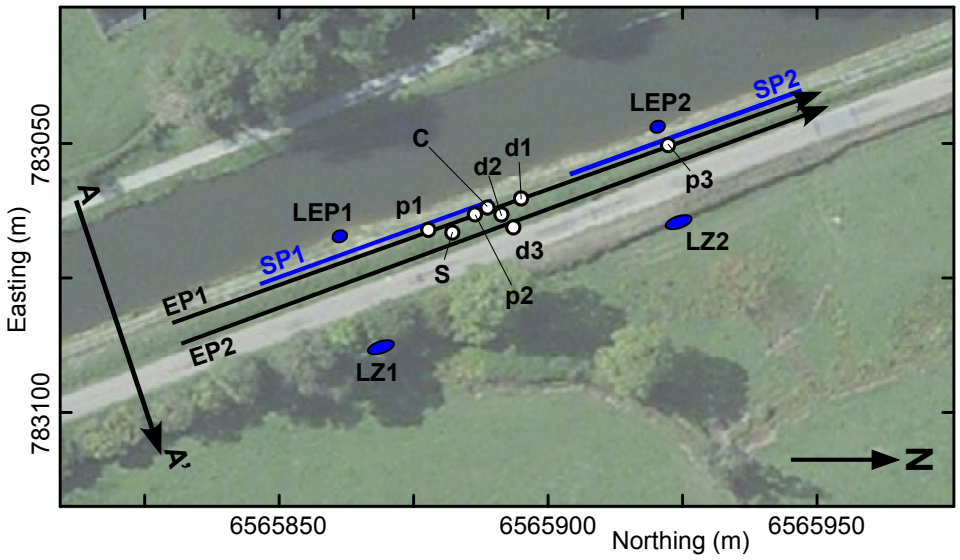

Figure 3.5 – Location of the geotechnical and geophysical experiments on the study site (Bièvre *et al.*, 2017). EP1 and EP2: electrical resistivity profiles; SP1 and SP2: seismic profiles; d1 to d3: drilling; p1 to p3: permeability and penetrometer test; C: coring. The position of the 2 seepage entry paths (SEP1, SEP2) within the canal and of the 2 corresponding leakage zones (LZ1, LZ2) at the bottom of the dyke is also indicated.

3.2.1.1 Electrical Resistivity Tomography

In the past decades, ERT has become one of the most popular geophysical techniques to investigate such structures. It allows imaging in high-resolution the depth to the bedrock and the lateral variation of the interface between the dyke and its substratum (Cardarelli *et al.*, 2010; Minsley *et al.*, 2011; Cardarelli *et al.*, 2014; Bièvre *et al.*, 2017). This technique can also provide information about the internal structure of the dykes (Weller *et al.*, 2006; Cho & Yeom, 2007; Niederleithinger *et al.*, 2012). Measurements can also be repeated to provide the evolution of resistivity with time. This time-lapse approach is used to derive the variation of a physical parameter to which resistivity is sensitive (temperature, clay content, moisture, etc.). This approach was used by several authors to locate seepage paths within earth dykes (Sjödahl *et al.*, 2008, 2009; Weller *et al.*, 2014).

However, for practical considerations such as cost-effectiveness and available space, electrodes are generally spread along the dyke crest. This configuration might appear very well suited to try to detect weak zones, where seepage paths could exist at depth and which are generally perpendicular to the dyke stretch and, consequently, to the electrode spread. Classically, dyke crests are considered as flat structures and analytical geometric factors, defined for infinite flat half-spaces, are used to compute apparent resistivity. Thus, data are processed using 2D inversion algorithms which do not take into account the 3D geometric effects caused by the topography, and the 3D geophysical effects caused by the subsurface resistivity distribution. The effect of topography was reported and evaluated numerically in 2D for more than forty years (Fox *et al.*, 1980). However, such effects remain little studied specifically in the context of earth dams and only very few studies were reported (Hennig *et al.*, 2005; Sjödahl *et al.*, 2006; Cho *et al.*, 2014). More recently, Fargier *et al.* (2014) studied numerically and experimentally such geometric effects on a smaller structure, namely an earth-filled dyke with a height of 6 m and a width of 28 m. They confirmed the existence of 3D geometric effects and proposed to correct them by using the computation of topographic (i.e. surface geometry) effects but also by using a priori information regarding the 3D resistivity distribution of the sub-surface. However, this approach requires a very good knowledge of the 3D distribution of resistivity which seems difficult to achieve in the case of earth dams.

In this work, it was chosen to account for topographic effects only, i.e. an easy-to-determine parameter with a high degree of confidence. First, 3D numerical modelling was used to evaluate quantitatively the topographic effects in the context of dykes. The direct current electrical diffusion problem was solved using 3D finite element synthetic models simulating the studied dyke. Computations were conducted using the Matlab F3DM package (Clément & Moreau, 2016) coupling Matlab and Comsol Multiphysics softwares. Increasing levels of complexity were considered to evaluate the effect of topography and 3D/4D resistivity distributions (e.g. a change in the water level in the canal). Such an approach allows computing custom geometric factors and assessing their benefit on the 2D inversion. Second, experimental static and time-lapse data were processed using these computed geometric factors before a classical 2D inversion. The variation of the water level in the canal induced time-varying topography and resistivity variations during the study. These corrected results were then compared with the results of a classic 2D time-lapse approach to put forward the ability of this approach to retrieve more realistic resistivity which can help to image and monitor earth dykes more accurately.

Some results of the numerical study are presented in figure 3.6, showing the distribution of the electrical current density for two quadrupoles spreadings along the crest of a dyke of a maximum height of 6 m over a bedrock. The resistivity of the dyke and the bedrock are 50 Ω.m and 400 Ω.m, respectively. Simulations were conducted for two water levels in the canal: 3.7 m and 0.3 m below the dyke crest, respectively. The resistivity of the water was set to 20 Ω.m after

in situ conductivity measurements. Calculations were also conducted for two current electrode spacings (AB = 3 m and 63 m) corresponding to the minimum and maximum AB spacing for a conventional Wenner configuration with 64 electrodes with a constant spacing of 1 m. The cross-sections in figure 3.6 are located at the mid-point between electrodes A and B. Results show that for a small AB spacing and no water into the canal, the electrical current mainly flows in the dyke below the electrodes (Fig 3.6a). When water is present (Fig 3.6b), the distribution of the current density does not fundamentally change but a part of the electrical current is flowing through the canal water. At depth, however, the bedrock is poorly investigated compared to the dyke. For a large AB spacing and no water in the canal, results show that most of the electrical current investigates a large width of the dyke (Fig 3.6c). On the contrary, when water is present in the canal, most of the electrical current flows in the water and the sub-surface is poorly investigated (Fig 3.6d). Furthermore, all these results show that the current is distributed not only below the electrodes, along the flat crest of the dyke, but along a section that exhibits laterally marked topographic variations.

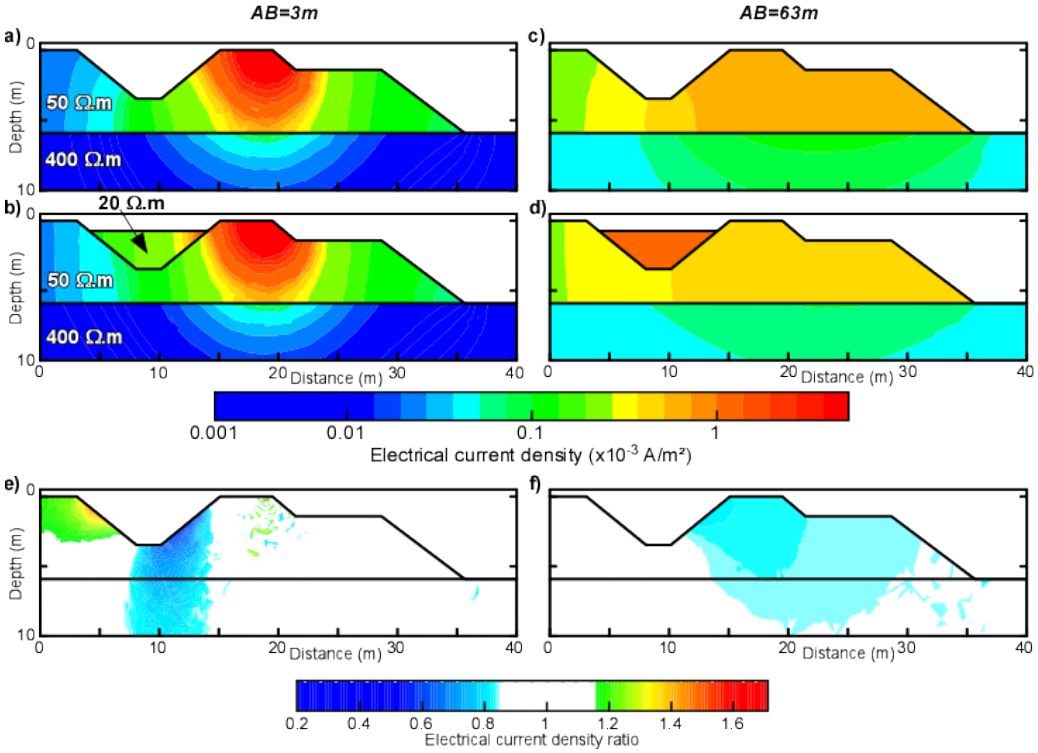

Figure 3.6 – Electrical current density distribution within the ground for two current electrode along the dyke crest and spacing AB of 3 m (**a** and **b**) and 63 m (c and d) and for two water heights into the canal: 0 m (**a** and **c**) and 3.4 m (**b** and **d**). The simulated transmitted current is 0.1 A. **e)** and **f)** present the electrical current density ratio between the canal filled with water and the empty canal, for a current electrode spacing AB of 3 m and 63 m, respectively. The white colour represents ratios between 0.85 and 1.15. Figure from (Bièvre *et al.*, 2017).

Figures 3.6e and 3.6f present the ratio of the electrical current density distribution with and without water in the canal for the two AB spacings 3 m (Fig 3.6e) and 63 m (Fig 3.6f). The white colour refers to a ratio arbitrarily chosen between 0.85 and 1.15. It reflects no major variation between the two models. The images reveal that for small AB spacing, the presence of water implies an important decrease of the current density (ratio as low as 0.2) in the dyke (and the bedrock) between 7 m and 14 m along the section. This is caused by the inlet of electrical current in the water in its upper-right part (see Fig 3.6b). The presence of water in the canal does not seem to have a major influence on the current distribution right below the electrodes. Figure 3.6f shows that for a large AB spacing, the presence of water in the canal induces a general decrease (around 20 %) of the current density below the dyke crest. The comparison of the two images (Figs 3.6e and 3.6f) indicates that when water is present in the canal, the

distribution of the current density is affected in a laterally varying way. This suggests that accompanying the topographical effect induced by the dyke geometry, the presence of water in the canal induces strong 3D effects on the current distribution when acquiring 2D measurements along the crest of the dyke.

To summarize the numerical study, the results indicate that it is possible to retrieve more realistic resistivity values by computing 3D topography effects which influence 2D inversion results. The proposed methodology consists of computing an a priori correction of geometric factors based on simple topographic measurements. It is particularly well adapted in the context of dyke survey since these data can be easily acquired in the field. However, it must be stressed that these topographic corrections do not allow to fully correct the measured resistivity from 3D effects (such as 3D resistivity distribution). Measurements are still conducted in 2D in a strongly 3D context. As such, the 2D assumption is not valid and the retrieved resistivities cannot be considered as true ones.

Results on experimental data are presented in figures 3.7a and 3.7b, which show the reference section of profile EP1 (location of the profiles in Fig 3.5) inverted with the analytic geometric factor Ka (Fig 3.7a) and with the computed one Kc obtained with the filled canal topography (Fig 3.7b), respectively. In the same way, Figures 3.7c and 3.7d expose the results for profile EP2. Figures 3.7a and 3.7c present the reference section of profiles EP1 and EP2, respectively, inverted with the analytic geometric factor Ka. Inversions provided good quality results for both profiles with $\chi^2 \approx 1$ and RRMS errors below 5 % after a few iterations. The resistivity distribution inverted with Ka on EP1 (Fig 3.7a) and on EP2 (Fig 3.7c) exhibit a significant discrepancy. To quantify these differences, statistics on the resistivity of these sections were computed for the dyke and the bedrock. 2 zones between 20 m and 107 m along the profile were selected to compute values: between 0 m and 2 m depth for the dyke and between 4 m and 7 m for the bedrock. In the dyke, the average value of resistivity for EP1 is higher than the one for EP2 with a relative difference of 31 % between the two profiles (29 % on the median value). A similar trend is observed at depth in the bedrock with a relative difference of 31.5 % on the average value (42 % on the median value).

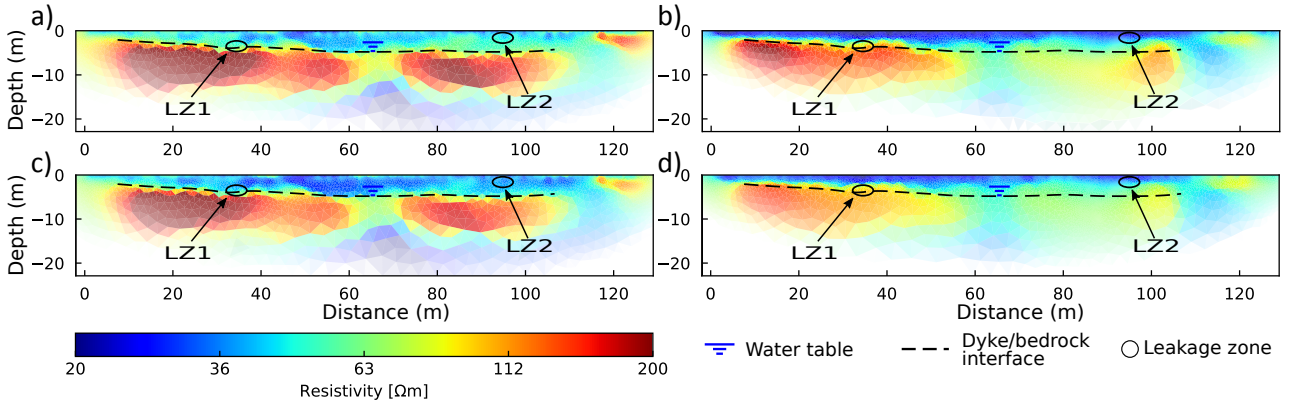

Figure 3.7 – Resistivity sections of profiles EP1 (location in Fig 3.5) **a)** using Ka and **b)** using Kc and of profile EP2 **c)** using Ka and **d)** using Kc. The black circles correspond to the localization of the two observed leakage zones LZ1 and LZ2. Figure from Bièvre *et al.* (2018c).

Given the vicinity of the two profiles, it seems very unlikely that these differences could be caused by a varying geotechnical context. Using the methodology proposed in this work, geometric factors Kc were computed for EP1 and EP2 with respect to its electrode locations for a topography corresponding to the filled canal. Results using Kc for EP1 and EP2 are presented in figures 3.7b and 3.7d, respectively. As observed with numerical modelling, both images using Ka and Kc exhibit the same geometry but show resistivity differences. Images show a global

decrease of resistivity for EP1 and an increase for EP2. The average relative difference for the dyke zone decreases down to 2.2 % using Kc. The correction of geometric factors thus provides a significant improvement of the agreement between the two profiles. However, for the bedrock, the inversion with Kc drives a decrease of resistivity for both EP1 and EP2 of about 10 % keeping the relative difference between the two profiles globally unchanged. This suggests that using computed geometric factors is efficient to retrieve more realistic resistivity at the surface while, at depth, the 3D distribution of resistivity may predominantly influence the data.

To conclude, the proposed methodology allows improving the analysis of dyke structure using ERT measurement. The four main steps of the approach can be described as **1)** ERT measurements along the structure using a classic methodology, **2)** topography measurement, **3)** numerical estimation of the geometric factor induced by the surface morphology and the water level and, finally, **4)** inversion of the apparent resistivity (static or time-lapse) recalculated using the geometric factor deduced in step 3. Based on a simple correction of geometric factors deduced from numerical computation, it could be easily applied to a practical situation since it only requires measuring the surface topography of the study site. Such an approach may also improve the quality of 2D ERT surveys performed on sites presenting a complex and strong 3D topography such as, among others, landslides, engineered slopes and mountainous areas.

3.2.1.2 Multichannel Analysis of Surface Waves

The results of the extensive prospecting conducted on the same dyke (not shown here ; details in Bièvre *et al.*, 2017) showed a good agreement between the geophysical imaging techniques (ERT, P- and SH-waves refraction tomography) and the geotechnical data to detect the depth to the bedrock and its lateral variations. On the contrary, surface waves failed to determine the depth of the bedrock. A close analysis of frequency-wavenumber (f-k) images for both Rayleigh and Love waves (Figs. 3.8a and 3.8b, respectively) reveals that only the fundamental mode of Love waves is energetic. The inversion of the experimental dispersion curve of Love waves (shown in Fig 3.8c) leads to the result shown in figure 3.8d as a grey stripe. The figure shows that the depth to the bedrock is underestimated (2.5 m) contrarily to the depth determined from SR tomography, ERT and boreholes (4 m). The velocity in the bedrock is also underestimated as well as very badly resolved (400-875 m/s instead of 1200 m/s). These results suggest that surface wave inversion might not be fully adapted for dyke investigation. This may originate from the particular geometry of dykes, non-respectful of the 1D assumption, and which induces depth and velocity discrepancies on inversion results. Relatively few studies reported the use of MASW for earth dam investigation so far (e.g. Cardarelli *et al.*, 2010, 2014) but none evidenced such pitfalls. However, one can quote the statement by Fell *et al.* (2015) regarding MASW applied to dyke investigation from the perspective of the geotechnical engineering community: it provides "relatively sophisticated analysis which may produce complex results which sometimes cannot be explained by other subsurface data".

To illustrate this statement, the experimental dispersion curves obtained on the site were compared with theoretical analytic dispersion curves assuming a 1D hypothesis (flat and infinite half-space). These theoretical curves were computed for both Love and Rayleigh waves and two heights: 2.5 m as deduced from Love waves inversion and 4 m as obtained from geotechnical data and other geophysical methods. Results are shown in figure 3.9a for Love waves and figure 3.9b for Rayleigh waves. In both figures, the fundamental and first higher modes are superimposed on the experimental *f-k* diagram. For Love waves, results suggest that the theoretical and experimental dispersion curves for the fundamental mode match well for a dyke thickness of 2.5 m and that it is the fundamental mode that propagates in the frequency range 12-25 Hz. On the contrary, with a dyke thickness of 4 m corresponding to the site condition, no

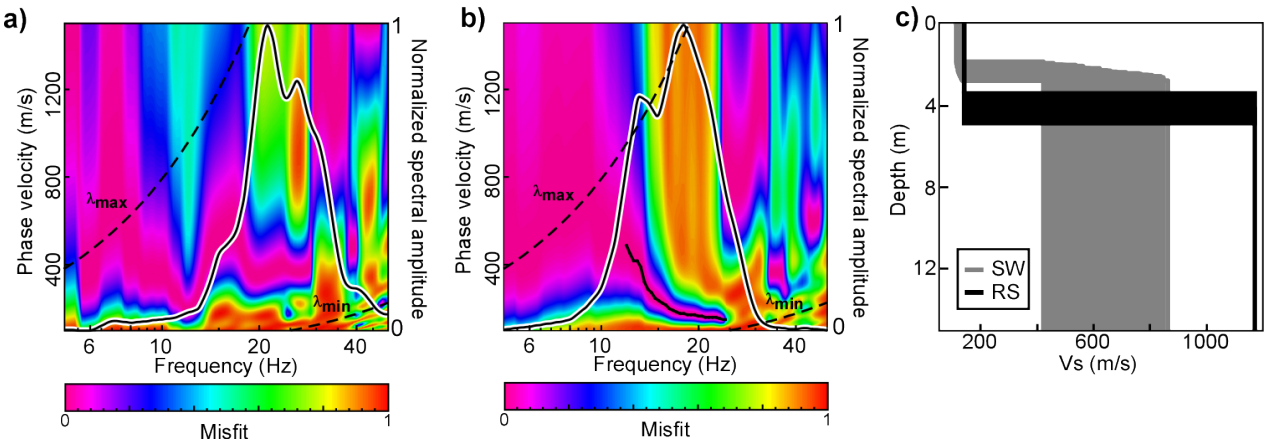

Figure 3.8 – surface waves analysis along profile SP1 (modified from Bièvre *et al.*, 2017). **a)** Rayleigh and **b)** Love waves phase velocity versus frequency for an endshot at 18 m along the profile and a group of 8 geophones between 34 and 48 m. The white line depicts the normalized spectral amplitude. The black line in Fig 3.8b corresponds to the picked experimental dispersion curve for Love waves. **c)** V_S profile (in grey) after inversion of the dispersion curve in Fig 3.8b. SW: surface wave inversion; RS: 1D V_S profile extracted from the 2D tomographic profile.

theoretical dispersion curve matches the experimental one. However, one can argue that, from the experimental *f-k* diagram, it is not clear whether it is the fundamental mode propagating between 12 and 25 Hz. 3D numerical modelling could help better assess the modes propagating in the structure (see section 3.3).

For Rayleigh waves, results suggest that the experimental and theoretical data do not fit satisfyingly (Fig 3.9b). This indicates that the experimental Rayleigh SW measurements might be perturbed by the particular surface morphological setting, below a width-to-height ratio of 4 according to Karl *et al.* (2011). However, this still does not explain why Love waves, contrarily to Rayleigh waves, and even if they provide an underestimation of both the depth to the bedrock and Vs in the dyke and the bedrock, do not appear as much perturbed. This effect still needs to be understood and, once again, 3D numerical modelling could provide insight into this issue.

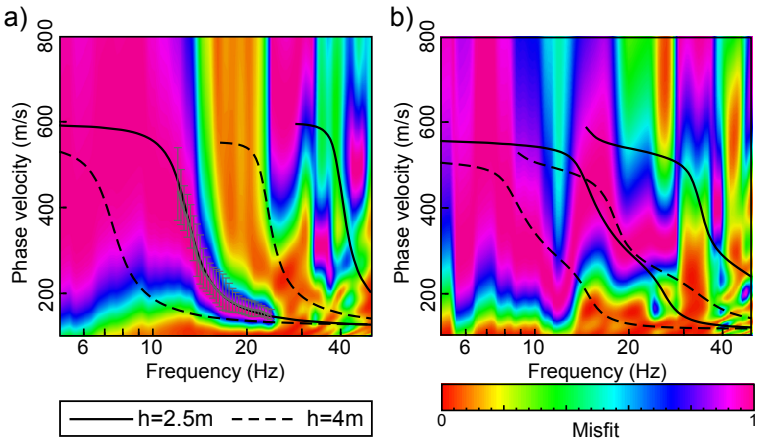

Figure 3.9 – Forward calculations of theoretical dispersion curves for the fundamental and the first higher mode of surface waves (black curves) for two heights of the dyke (2.5 m and 4 m). **a)** Love waves, with the experimental dispersion curve in grey. **b)** Rayleigh waves with the experimental f-k diagram for a shot at 0 m along profile SP1 (Fig 3.8a). Figure from Bièvre *et al.* (2017).

3.2.2 Localization of water leakage within an earth dam

The use of these classical prospecting techniques however did not allow to directly locate the two leakages within the studied earth dyke. The analysis of ambient vibration time series acquired before and after remediation works showed the ability of the technique to detect turbulent water leakage inside the dyke. Ambient seismic noise was recorded during one minute with 24, 4.5 Hz vertical geophones along profile SP1 in November 2010 before works and in May 2011, after works. These recordings (sampling frequency $Fs = 250$ Hz) were conducted for feasibility tests and were not intended to process ambient vibrations at first. The main objective was to evaluate the possible strong energetic content of the seismograms located just above the leakage path relative to the others. It was hypothesized that the possible strong seismic vibrations recorded during monitoring measurements would originate from the water circulating through the dam.

Figure 3.10a presents seismograms of ambient vibrations recorded along profile SP1 (location in Fig 3.5) in November 2010, before remediation works. It shows that four traces, located between 34 m and 40 m, have noise amplitudes much larger than the other ones. This location corresponds to the position of leakage SEP1 (35.5 m) and LZ1 (34.5 m) along the profile. This suggests that the leakages within the dam body generate significant vibrations which can be recorded at the surface of the dyke. Figure 3.10b presents the same recordings (with the same amplitude scale) conducted in May 2011. The striking feature is that every trace has the same noise level, and also that traces between 34 m and 40 m along the profile have a considerably reduced noise level after remediation works when compared to the recordings of November 2010. These results suggest that remediation works significantly reduced the leakages within the dam body such that induced vibrations can not be detected anymore. It also confirms that vibrations recorded in November 2010 between 34 m and 40 m originated from the water piping from LZ1 through the dam body.

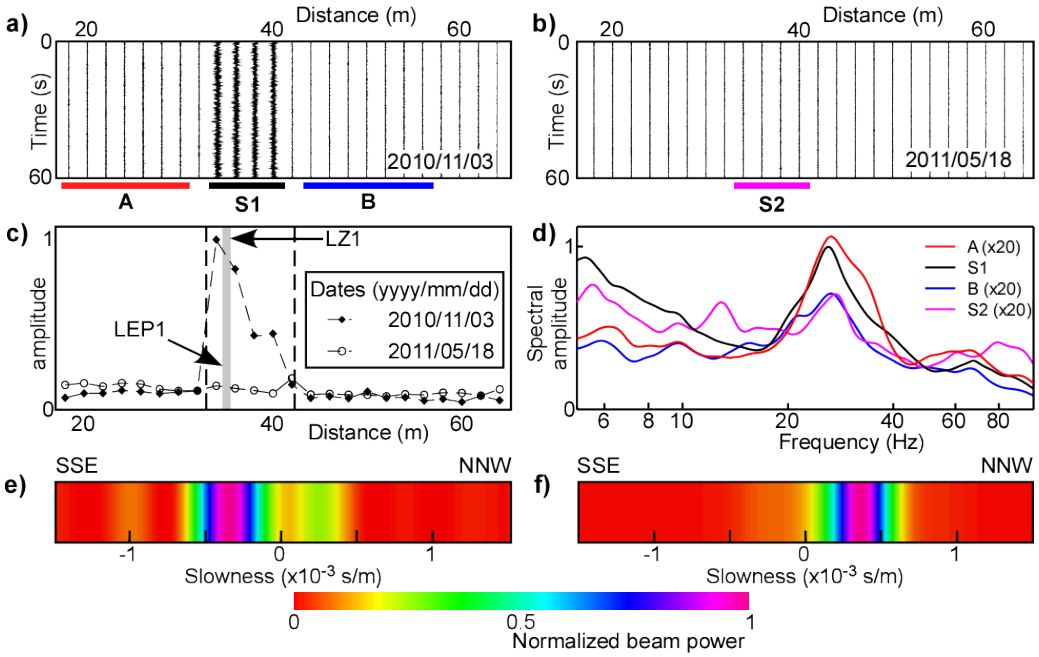

Figure 3.10 – seismic noise monitoring with 4.5 Hz vertical geophones along profile SP1 (Bièvre *et al.*, 2017). **a)** Seismograms recorded the 03rd of November 2010, before remediation works. A, S1 and B: see figure 3.10d. **b)** Seismograms recorded the 18th of May 2011 after works; S2: see figure 3.10d. **c)** Maximum absolute amplitude recorded at each geophone and expressed with a common amplitude scale. **d)** Fourier spectra of the 4 groups of geophones A, S1, B and S2. The position of the groups along profile SP1 is detailed in figures 3.10a-b. The spectral amplitude is expressed with a normalized scale and a factor of 20 for A, B and S2. **e)** and **f)** Wavenumber analysis (expressed in slowness) at a frequency of 25 Hz for A and B, respectively.

Figure 3.10c presents the superimposition of the maximum absolute amplitude of seismograms in figures 3.10a and 3.10b. It shows the lateral evolution of the maximum amplitude recorded at each geophone along profile SP1 during 1 min. It is expressed with a common normalized amplitude scale. The two most energetic traces are found at a distance of 34 m and 36 m. They are located immediately apart from the location of LZ1 (34.5 m) and SEP1 (35.5 m) along the profile. However, it is possible to observe energetic vibrations for a distance of up to around 42 m along the profile. This suggests that the path of the leakage within the dam body might not be straightforward between SEP1 and LZ1, but rather tortuous. This spatial coverage along the profile (33-34 m to around 42 m) is materialized in figure 3.10c by two vertical dashed lines. To assess that the water flowing through the dam body is the source of these energetic vibrations, their direction of propagation was analysed. The seismic profile was first cut into 3 groups of geophones, assuming that the source is located between abscissa 33-34 m and around 42 m (the four most energetic seismograms, labelled S1 in figure 3.10a). Assuming a wave propagation from S1, 7 geophones towards the beginning of the profile (A in Fig 3.10a) and 7 towards the end (B in Fig 3.10a) were selected. The spectral amplitude of each group is presented in figure 3.10d. S1 shows a pronounced peak at 25 Hz, which can be interpreted as the central frequency of the vibrating source. The 2 groups A and B also show a distinct peak at this central frequency (Fig 3.10d ; a factor of 20 was applied to both amplitudes of A and B). The spectral analysis was also conducted for group S after remediation works. The seismograms are shown in figure 3.10b (the group of geophones is labelled S2) and the spectral curve is presented in figure 3.10d with a factor of 20 for the amplitude. It shows the presence of a peak with a central frequency of around 25 Hz but with a magnitude 20 times lower than for S1. This suggests that water still flows at the interface between the dam body and the bedrock, but with a very reduced magnitude. This is in agreement with field observations where the flow at LZ1 was evaluated at around 250 l/min before works and at around a few tens of l/min after works. The corresponding Reynolds number Re is $\sim$ 20 000 and $\sim$ 4 000, respectively, indicating moderate but well-established turbulence before works and a much lower level (and potentially in the range of laminar or transition domain) after works. Groups A and B were then analysed in the *f-k* domain, for a central frequency of 25 Hz, deduced from the previous spectral analysis. The results are presented in figure 3.10e (A) and figure 3.10f (B) and are expressed in terms of slowness. For A, the slowness is negative and suggests a wave propagation towards the beginning of profile SP1 (i.e. from right to left in Fig 3.10e). On the contrary, the slowness is positive in the case of B (Fig 3.10f), which indicates a propagation directed towards the end of profile SP1. These results indicate that wave propagation originates from below the group of geophones S1. They suggest that the leakage path within the dyke is located below these geophones. This is supported by visual observation conducted after the emptying of the canal. However, the analysis of slowness reveals unrealistic values, corresponding to velocities of 300-800 m/s and 300-650 m/s for A and B, respectively. However, these values can only be considered as apparent velocities. The source is located at depth, below the water table, and close to the groups of geophones: this experimental setup is located in the near-field and hence does not respect the condition of incident plane waves.

From the previous section, it was shown that the water flow within the leakage path acts as a seismic source. Ambient vibrations recorded at the surface along profile SP1 might then contain information that could be used to track back the energy to its source. This was sought using a beam-forming algorithm modified from Lacroix & Helmstetter (2011) and that allowed to localize the most energetic water flow before remediation works. This method searches the source position and the wave velocity that maximizes the average intertrace correlation after shifting traces in time by their travel time, weighted as a function of their inter-distance. The algorithm searches for a continuous correlation over the whole seismic network (i.e. the 24 geophones). It was used on the 1 min-long signal for a wide set of initial parameter tests. The

results of the localization of the seismic source along profile SP1 and at depth, before and after works, are presented in figure 3.11. Figure 3.11 shows the location of the source at x = 37.1 m and z = 3 m for November 2011. These values are very close to the observed locations (x = 35.5 m and z = 3.4 m). The uncertainties were found to be 0.4 m both horizontally and vertically.

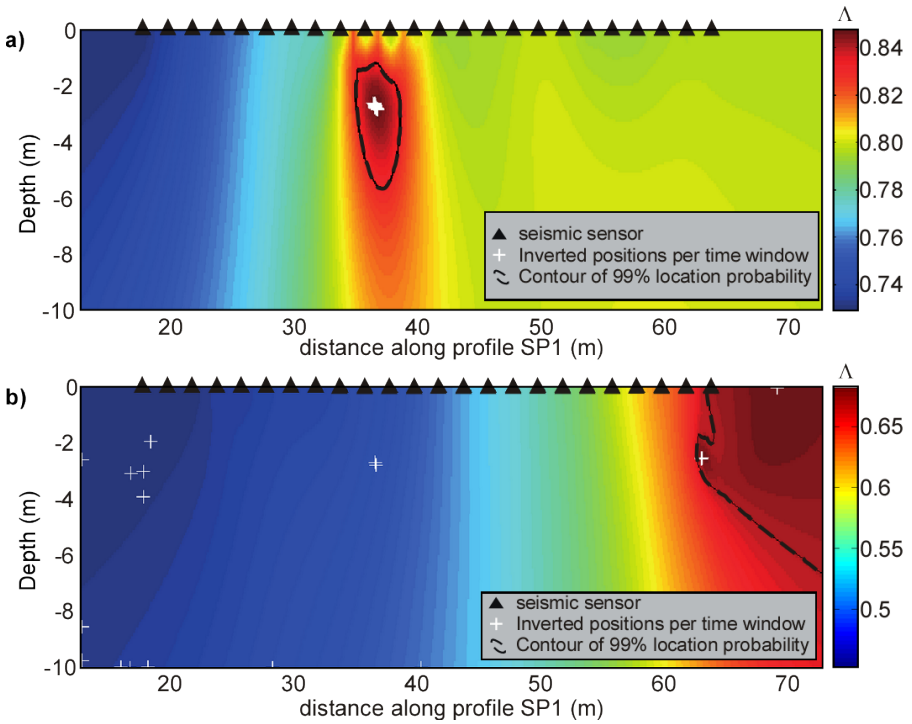

Figure 3.11 – Localization of the seismic source (modified from Bièvre *et al.*, 2017). **a)** and **b)** Probability Density Function (PDF) of the localization of the seismic source along profile SP1 in November 2010 (before remediation works) and in May 2011 (after remediation works), respectively. The white crosses represent the best locations inverted for each time window. The 99 % PDF is shown as a black ellipsoid. Please note that the colorscale is not the same for the two figures.

The same measurements were conducted along the same profile after remediation works, in May 2011. Results are presented in figure 3.11b. They show that no more seismic source can be located within the seismic network. Instead, the localization process shows a source coming from outside the network. Its precise localization is thus not possible, as shown by the large size of the 99 % maximum contour. Moreover, the maximum values of Λ are much lower than before remediation works (0.65 against 0.85). All these observations together show that the leakage does not produce detectable seismic signals anymore. It thus suggests that remediation works significantly reduced the water flow at this location.

These promising results allowed locating the main leakage with an uncertainty of 0.4 m. However, the method did not succeed to locate the second piping, because of a too-small signal-to-noise ratio. Further research must be performed to study the limits of this detection/localization method, in particular the flow limit of the detectable leakage. To achieve this goal, future works should focus on understanding the physical process linked with the generation of the seismic signal in the leakage zone. Longer time series might have allowed detecting the presence of this internal erosion zone. Further numerical and experimental works will help to evaluate the conditions necessary to detect water flows caused by internal erosion within dykes, and to monitor their evolution with time.

3.2.3 Detection of early stages of internal erosion

According to Fell *et al.* (2015), and in agreement with the results exposed previously, internal erosion is more likely to be detected in the advanced stages of progression and breach formation (i.e. late stage 3 and stage 4 in Fig 3.1). Hence, it appears crucial to detect as early as possible an ongoing internal erosion process and identify its current stage (1,2 or 3). The main objective of the following work was to capture the complete process of internal erosion, from the generation of water seepage until failure using a controlled laboratory experiment. These results were obtained during Y Maalouf's PhD (2017-2021) and recently published (Maalouf *et al.*, 2022).

An unconventional experimental design

Many laboratory experiments devoted to the study of internal erosion consist in building small-scale earth dams contained in tanks and encompassing artificial defects. However, in this configuration, water leakage may develop at the interface between the earth dam and the tank. These water leakages at the interfaces may be much more important than the one developing in the artificial weak zone. Furthermore, they prevent the detection of weak seismic signals that could correspond to the early stages of internal erosion. To avoid this issue, it was then decided to force a constant head of water to flow only in a weak zone, made here of a cylindrical soil sample 0.1 m in diameter and embedded into a concrete beam 1.5 m long (Fig 3.12). The system was then left to evolve naturally from progressive saturation up to failure.

Under the chosen experimental conditions, the time to failure of the soil sample is only controlled by the hydraulic gradient i (dimensionless) with respect to the critical hydraulic gradient i_c, and piping is initiated when i equals or is greater than i_c (Terzaghi *et al.*, 1996). Three preliminary feasibility tests were performed under all the chosen experimental conditions and soil sample properties. They showed an average time to failure of the soil samples of around 7.5 min.

Electrical resistivity was monitored using 14 electrodes linearly spread each 0.05 m. Despite intensive work on the data, the results were deceiving, notably because of too few measurements available with respect to the duration of the experiment. These results are not presented hereafter. Three cameras were also used to monitor the experiment (rate of 30 frames per second). One camera was placed on the tank to monitor the water level. The two others were placed apart from the soil sample (i.e. upstream and downstream) to timestamp the observed events.

Dynamics of seismic events

Data were acquired continuously during the experiment with a sampling frequency of 500 Hz. Since seismic velocities in concrete are elevated (P-wave velocity above 2000 m/s), data obtained by the 5 geophones showed to be redundant and only the results from the geophone placed above the soil zone will be further presented. Passive monitoring of the experiment was conducted by recording waves propagating inside the experiment and detecting small seismic events. The acoustic emission introduced by Koerner *et al.* (1981) on dams consists of counting seismic events with amplitudes larger than a certain threshold. This has been used to monitor earth dams and to detect changes occurring inside the structure (Rittgers *et al.*, 2015). In the present work, seismic signals were filtered in different frequency ranges and normalized to the maximum amplitude of a 5 min-long time window of the signal during the water flow in the soil sample. Following the normalization, different thresholds were set and the peaks exceeding the thresholds were cumulated and normalized by their maximum. These time series were then compared to events detected in the video monitoring to identify the different stages of internal erosion.

The dynamics of the number of seismic events as the experiment approaches the failure was

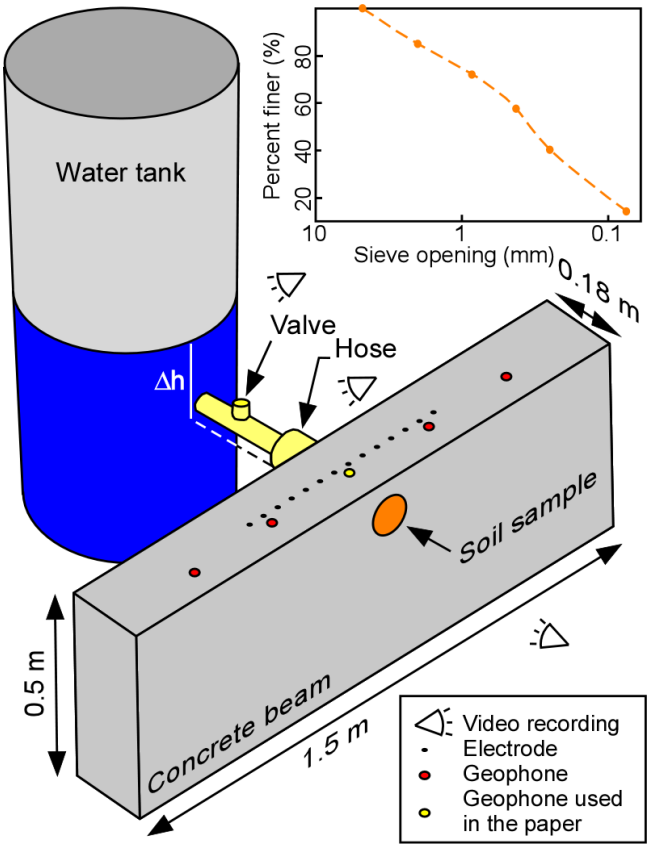

Figure 3.12 – Laboratory setup of the seepage experiment (Maalouf *et al.*, 2022). Δh represents the difference in water height between the water level in the tank and the bottom of the soil sample zone. The granulometric distribution of the soil sample is shown..

monitored by counting them. Figure 3.13 presents the filtered seismic data in three frequency bands that were defined from a spectral analysis of the spectrogram: 140-160 Hz (Fig 3.13a), 80-120 Hz (Fig 3.13c), and 5-20 Hz (Fig 3.13e). The associated right panels (Figs. 3.13b, 3.13d and 3.13f, respectively) show the normalized cumulative number of seismic events detected in the seismic time series and classified by classes of amplitude. In each frequency band, the amplitude of an event was defined with respect to the strongest event of the frequency band. This normalization reveals that the strongest event of each frequency band is associated with the final failure occurring at the end of the experiment. Then, in each class of amplitude, the cumulative number of events was normalized to the total number of events of the class. This two steps normalization allows comparing the dynamics of the experiment in the different frequency bands. Four amplitude classes were established to differentiate the dynamics of the experiment : 1) small events between 0.1 and 0.4 represented by the grey curve, 2) events between 0.4 and 0.6 represented by the blue curve, 3) events between 0.6 and 0.8 represented by the green curve and, finally, 4) events larger than 0.8 represented by the red curve.

Figures 3.13a and 3.13b present the seismograms and the cumulative number of seismic events, respectively, in the frequency range 140-160 Hz. Figure 3.13a shows that besides the period of valve opening, most of the seismic events (with large amplitude) occur at the time of MM2 and after. Small amplitude seismic events are visible from 2 to 4 min. One stronger series of events is recorded around time 5 min. Some of these events could be related to environmental noise and, if so, their occurrence should follow a random pattern. Figure 3.13b shows that for all classes of seismic detections the pattern is not random at all. Not considering the period of valve opening, the first three minutes reveal events with small amplitudes: the grey curve increases continuously and rather slowly. Slightly before 3 min, blue class seismic events are detected

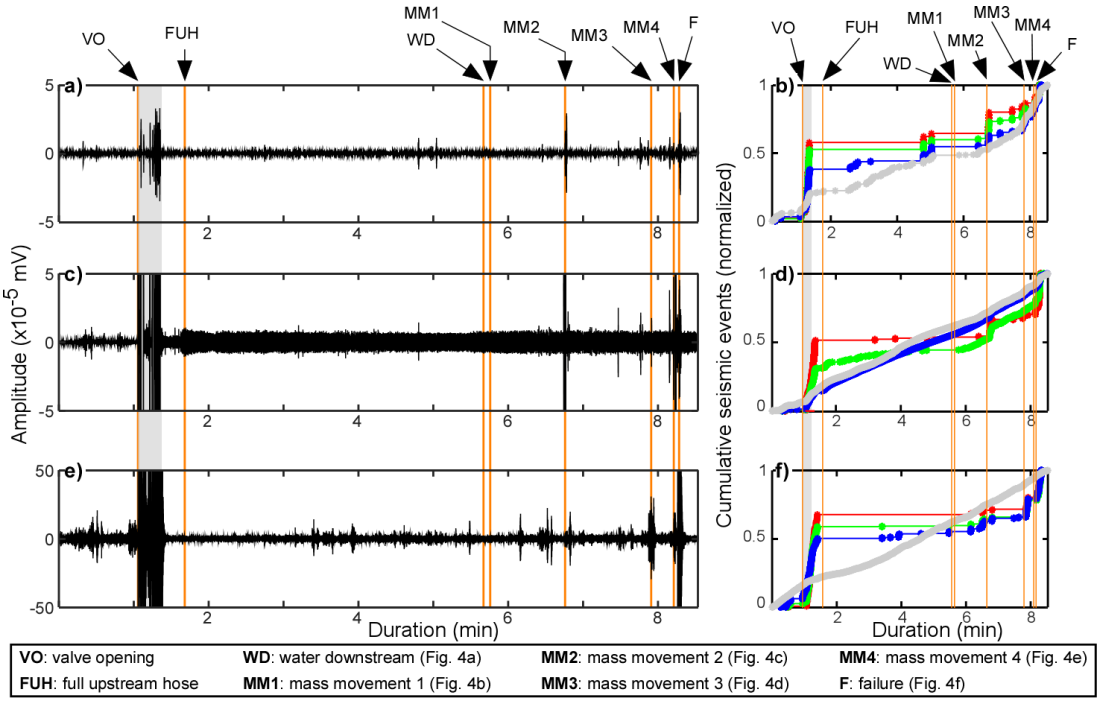

Figure 3.13 – Seismic event detection (Maalouf *et al.*, 2022). **a)**, **c)** and **e)** Seismic record of geophone 3 filtered in the 140-160, 80-120 and 5-20 Hz frequency range, respectively. Vertical orange lines indicate the different phases of the experiment (details at the bottom of the figure). The grey stripe corresponds to water movements in the tank following valve opening. **b)**, **d)** and **f)** Cumulative number of events per class of amplitude normalized to the strongest event. Grey: normalized amplitudes between 0.1 and 0.4; blue: normalized amplitudes between 0.4 and 0.6; green: normalized amplitudes between 0.6 and 0.8; red: normalized amplitudes between 0.8 and 1. Events observed visually or from camera monitoring are indicated.

and the rate of grey class events suddenly increases. A similar sequence occurs at 5 min, with detections in all the classes. It suggests that a large event occurred within the soil sample because no video recording correspond to this sequence. Then, the system remains extremely quiet with no detection in this band until time 6.5 min, despite the occurrence of MM1 within that period. With the water appearing downstream starts a new sequence of small grey class events at first, rapidly followed by blue and green seismic detection and a major cluster of strong events corresponding to MM2. Contrarily to the first sequence, the rate of small grey class events is sustained and even increases slightly before MM3 (7.78 to 7.91 min). Similarly, the rate of blue, green and red classes increase until the final failure of the soil sample. The changes of rate detection observed for the different classes of events strongly suggests that most of the detections of seismic events in the 140-160 Hz frequency band are related to the physics of the soil sample evolution rather than to environmental noise. These detections suggest that the evolution of the soil sample is complex with at least one unrecorded seismic sequence at time slightly before 5 min. This is followed by events MM1 to MM4 and, eventually, the complete failure, all time-stamped using video recording. These events show both an increase in the rate of detection and an increase in the amplitude of the events.

Figure 3.13c presents the seismogram in the 80-120 Hz frequency band. It is dominated by a small amplitude but sustained seismic activity throughout the experiment. Some stronger seismic events are visible that correspond to the unrecorded seismic sequence occurring before 5 min (see above), event MM2 and a short period preceding the failure. The small amplitude and sustained activity that dominates the record is formed by repetitions of very short duration events that will be discussed further. Figure 8d presents the cumulative number of detections per class of amplitude. The grey and blue curves are particularly linear, despite some deviations at the valve opening and during some mass movements. This linear behaviour suggests, first, a

nearly constant detection rate and, second, that the seismic events correspond to a background noise added to the signals. These classes of detections are much less sensitive to the soil sample evolution. Nonetheless, they will be further used to perform independent monitoring of the evolution of the soil sample. On the contrary, the green and red classes (intermediate and strong events, respectively) obey a different evolution. Shortly after the end of the valve opening phase, the number of detections in the red class is zero before increasing very weakly until event MM2. The rate of detection in the green class is slowly decreasing until the moment where water is observed downstream (5.67 min) along with event MM1 (between 5.7 and 5.76 min), where the rate increased suddenly. The occurrence of the second event MM2 (from 6.61 to 6.76 min) generated a bunch of strong and intermediate seismic events that are also recorded in the 140-160 Hz frequency band. Interestingly the green class shows a sustained rate that accelerates with the occurrence of the last sequences of events MM3 (7.78 to 7.91 min) and MM4 (8.15 to 8.21 min) before the failure (8.3 min).

Figure 3.13e presents the record of the seismic activity filtered in the 5-20 Hz frequency range. The background seismic noise is important because it captures the steps of the experimentalists before the valve opening. Shortly after, the seismic signal is of low amplitude, with barely any strong events. The situation changes at 3 min, with the first stronger events occurring. Some of them are apparently not related to the macroscopic events recorded by the video or detected in the 140-160 Hz band. Figure 3.13f presents the cumulative number of detections per class of amplitude. The grey curve shows a nearly linear behaviour, suggesting again that these small-amplitude events are related to the seismic background noise. On the contrary, the blue, green and red curves show strongly non-linear behaviours. The blue curve shows the first detection shortly after 3 min, rapidly followed by the green curve. Only very few events occur in these classes and none in the red class. Changes are observed between 6 and 7 min (i.e. between MM1 and MM2), with an increase in detection rate in blue, green and red classes. Interestingly the detections precede event MM1 and stop at the time of event MM2. Then, the curves increase again shortly before events MM3, MM3 and, eventually, the final failure.

Ambient noise monitoring

Ambient seismic noise monitoring is a technique that consists of correlating seismograms of different geophones to identify relative changes in velocity (dV/V) and/or in the correlation coefficient (cc) of the waves. Changes in velocity are related to changes in stiffness while changes in cc are related to geometrical or structural changes (Larose *et al.*, 2015a). However, considering the high velocity in the concrete with respect to the dimension of the experimental setup and the sampling frequency, cross-correlation between couples of geophones eventually resembles auto-correlation. It was then chosen to auto-correlate signals recorded on the geophone located above the soil sample. Seismic signals were first cut in 2 s-long windows. They were then standardized (subtraction of the mean and normalization by the standard deviation of the 2 s-long samples) and further auto-correlated. Classical ambient seismic noise studies imply a spectral whitening of the seismic recordings to avoid the correlation being dominated by a particular source. The cross-correlation of successive time windows gives insight into the evolution of the Green's functions and the changes in the medium. Contrarily to these studies (e.g. Planès *et al.*, 2016), an active and repetitive source was introduced, under the form of a controlled leak located upstream. That source was energetic enough to be recorded by the geophones and, hence, to monitor the evolution of the experiment.

The wave created by this source passes through the concrete beam and the soil sample. Any change in the medium (i.e. in the soil sample, since no change occurs in the concrete) should lead to a change in the arrival time of the seismic wave. Therefore, a correlogram was computed

from the autocorrelation of successive 2 s-long seismograms of geophone 3 placed on top of the seepage zone and filtered in the frequency range 80-120 Hz. Results are presented in figure 3.14a under the form of the evolution of time lags as a function of the duration of the experiment and with correlation coefficients cc represented by a colour scale. For the sake of visibility, this colour scale was intentionally limited to values ranging between -0.2 and 0.2. Before the valve opening (and the occurrence of water drop), no clear event is visible. After the valve opening, 4 main events are detected. The first one consists of the autocorrelation with its highest correlation coefficient at zero lag. Three further events are observed at average lags of around 0.5, 1 and 1.5 s with, however, time lags that tend to increase non-linearly as a function of the duration of the experiment. These three further events were extracted from figure 3.14a and are presented in figure 3.14b. The 3 curves show the same trends during the experiment. First, from 1.65 min to around 3 min, there is an increase in the arrival times (and, hence, a decrease of the apparent velocity). This is interpreted as originating from the progressive infill of water into the soil specimen, leading to a change in its structure and the subsequent rearrangement of soil particles. It is noticeable that the slopes of the 3 curves are not identical (this is more visible in Fig 3.14b). This is caused by the autocorrelation process itself, where the correlation of increasing arrival times (caused by the multiple probing of the medium by the same wave) leads to progressively increasing time lags. This also explains the decrease of the correlation coefficient with the increase of the lag time as illustrated in figure 3.14b (with genuine *cc* values): for later arrivals, the wavefront scanned the medium several times and its similarity with the first one is degraded.

Second, there is a slow increase of arrival times during the water seepage stage up to the moment when water appears at the downstream. Third, as water appears downstream at 5.67 min, followed by mass movement MM1, the time lag increases again. Fourth and finally, variable further increases of the time lag are evidenced which are related to the different mass movement events and the final failure. Interestingly, the increase in the time lag appears to be controlled by the different stages of this experiment that are detected in the video monitoring. This simple measure of autocorrelation reflects the changes in the water content of the soil sample and the structural changes induced by the mass movements. The only varying portion of the experiment is the soil sample. It is then considered here that the concrete beam is poorly altered and interacts very little with the water.

Interpretation

The continuous monitoring using passive seismic recordings permits interpretation of the evolution of the soil structure during the different stages of internal erosion, where no visual evidence was granted. The main events that were observed during the video monitoring were detected in the seismic signals in addition to multiple events preceding and following each snapshot. These events represent changes inside the structure of the soil sample such as the rearrangement of soil particles, the transport of soil particles and small mass movements that were not identified in the video. The curve of the cumulative seismic events in the frequency range 80-120 Hz and thresholds between 0.6 and 0.8 (Fig 3.13d) was selected to illustrate that changes in the slope of the curve highlight the changes corresponding to the different phases of internal erosion : 1) at 5.76 min where the initiation phase ends and the continuation phase starts; 2) at 6.76 min where high amplitude events highlighted by a jump take place indicating the end of the continuation and the start of the progression phase; 3) at 8.21 min, another jump takes place suggesting the end of the progression phase and the start of the breach which is represented by high amplitude events denoting the failure of the sample.

The autocorrelogram in figure 3.14 also shows the changes in slopes that highlight as well the

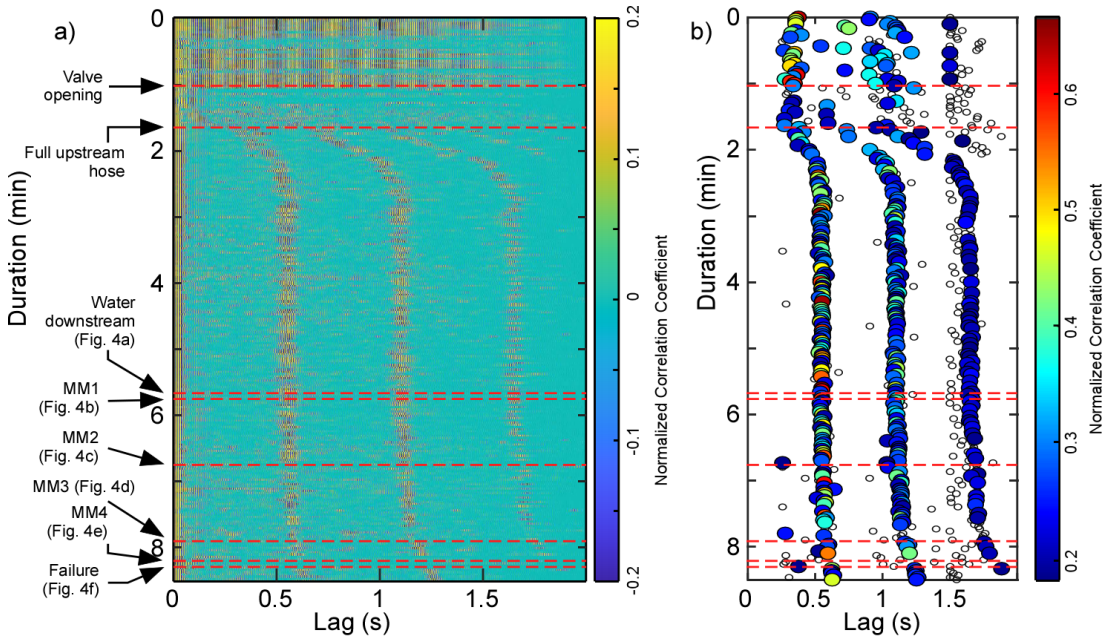

Figure 3.14 – Autocorrelation of seismic time series recorded by geophone 3 located immediately above the soil sample zone and filtered between 80 and 120 Hz (Maalouf *et al.*, 2022). a) Causal part of the autocorrelation (the acausal part is symmetric). b) Maximum cc values of each autocorrelation. *cc* values below 0.18 were discarded and are represented by small white-filled circles. Monitored and observed events are indicated by red dashed lines.

4 stages of internal erosion: 1) a change in slope is observed at 5.76 min indicating the end of the initiation phase and the start of the continuation phase; 2) at around 7.5 min, highlighting the end of the continuation phase and the start of the progression phase; 3) at 8.30 min, the end of the progression phase and the start of the breach.

Figure 3.15 summarizes the seismic activity in the soil sample and its relation to the different stages of internal erosion (i.e. initiation, continuation, progression and failure). The cumulative seismic events (black curve) correspond to the curve described above (frequency range 80-120 Hz and amplitude between 0.6 and 0.8) where the part before 2 min was removed. The autocorrelation curve (red curve) corresponds to the time lag greater than 1.5 s. It was chosen because it shows more pronounced slope changes. Also, the time lag, proportional to the apparent seismic velocity (the greater the lag, the lower the velocity and vice-versa) was expressed in terms of slowness (the inverse of the velocity) to present a trend similar to the cumulative number of seismic events. Once again, observations before 2 min were removed to highlight phenomena corresponding to the evolution of the soil sample during erosion only.

The two superimposed curves reveal globally similar trends with slope breaks corresponding to the identified stages of internal erosion. The change from continuation to progression shows, however, a slight discrepancy between the two geophysical parameters. Nevertheless, the two parameters are in good agreement and suggest they are both suitable to detect changes in soil samples subject to internal erosion in a laboratory experiment. Moreover, it appears that in this experiment seismic monitoring allows the detection of early stages of internal erosion, namely initiation and continuation.

Both visual observations and seismic interpretations of the data allowed the identification of the 4 different stages of internal erosion (i.e. initiation, continuation, progression and failure). The seismic data show high amplitude events preceding the progression phase identified in the snapshots. Hence this experiment suggests that seismic techniques are adapted to detect changes inside the structure of the soil that lead to failure. These preliminary and encouraging results pave the way for more realistic experiments on a larger scale.

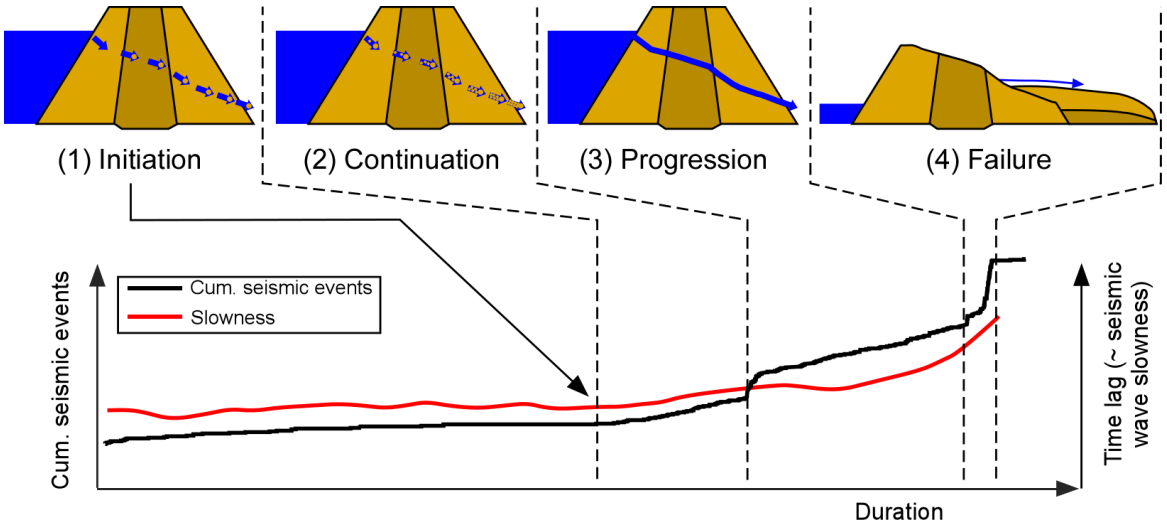

Figure 3.15 – The different stages of internal erosion interpreted from seismic monitoring (Maalouf *et al.*, 2022). The time lag (proportional to the apparent velocity) computed from autocorrelation is represented as a slowness (the inverse of velocity) to present a trend similar to the cumulative number of seismic events.

3.3 Perspectives

3.3.1 How do geometry and layering affect seismic wave propagation?

From section 3.2.1, it has been shown that surface wave inversion provides ground models in disagreement with geotechnical prospecting and geophysical imaging. It questions the way surface waves are affected by the propagation in such structures: how does the geometry (base-to-height ratio, slope angle, etc.) affect surface wave propagation? Why do Love waves appear less affected than Rayleigh waves (e.g. Bièvre *et al.*, 2017)? Is it possible to develop a simple methodology to correct, or at least evaluate, these geometric effects? What is the influence of the water table on these effects? Karl *et al.* (2011) worked on flood prevention dams, *i.e.* without a permanent water head, and the effect of the water table on seismic wave propagation in such structures remains unknown.

This can be evaluated using notably 3D numerical modelling. Some preliminary results of numerical simulations are exposed in figure 3.16. Figure 3.16a shows an example of the simulation domain and the mesh adopted for a dyke with a height of 10 m and a slope of 0.66, similar to the experimental site previously investigated. Dispersion curves of the fundamental mode of Rayleigh waves for different heights from 3 to 14 m are shown in figure 3.16b (thick lines) along with the corresponding theoretical analytical curves for 1D cases (thin lines).

The observation of the dispersion curves shows that, for all dyke heights, theoretical and computed dispersion curves are similar but are shifted in frequency. This shift towards higher frequency explains the underestimation of the thickness following surface wave inversion. Also, it is observed that the higher the dyke, the higher the frequency shift. This suggests that, consequently, the higher the dyke, the greater the underestimation of its thickness using classical surface wave inversion. These brief and very preliminary results show the ability of numerical modelling to evaluate the impact of this complex geometry on seismic wave propagation. This work will be carried out in collaboration with researchers from ISTerre.

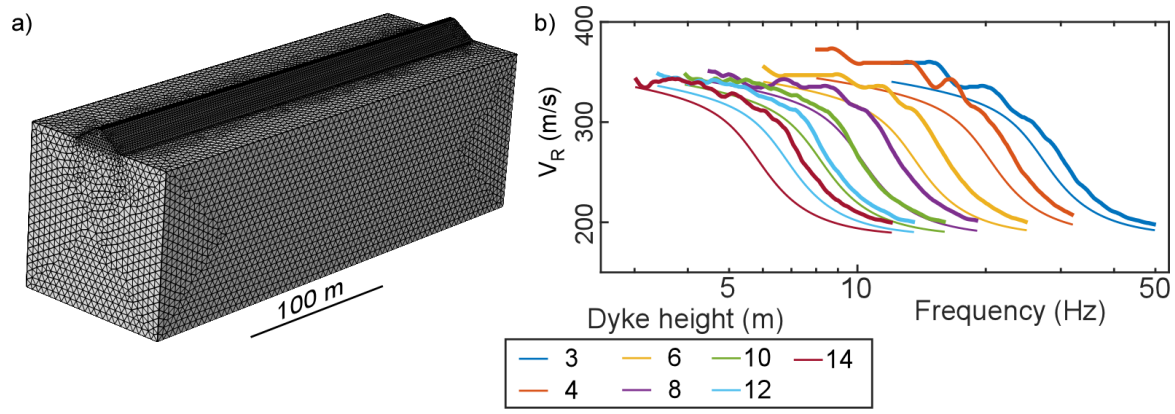

Figure 3.16 – Numerical modelling of seismic wave propagation along a dyke ($V_S = 200$ m/s, $V_P = 400$ m/s, $\rho = 2000$ kg/m^3) with a constant slope of 0.66, overlying a stiffer sub-surface($V_S = 400$ m/s, $V_P = 800$ m/s, $\rho = 2000$ kg/m^3). **a)** Example of the geometry and mesh for a dyke height of 10 m. **b)** Dispersion curves of the fundamental mode of Rayleigh waves for the numerical models (thick line) and the theoretical curves (thin line) for different dyke heights.

3.3.2 How to detect and monitor internal erosion in the field?

From the previous section, it has been shown that it is possible to detect the different stages of internal erosion from seismic measurements. However, the experiment was conducted in a controlled environment. Is it possible to use the same approach in the field?

At first, it seems that a real site would be subject to strong background noise that might prevent the detection of low-amplitude seismic events associated with early stages of internal erosion. However, an experiment conducted on a test site in Rouen (France) and consisting of a 3 m high earth dam encompassing pipes (10 cm in diameter) showed the ability to detect and monitor laminar water flow (Maalouf, 2021). The site is located close to a highway and, as such, subject to a high level of noise. However, it was possible to relate proportionnally the seismic energy to the water flow in a frequency range similar to the previously exposed laboratory experiment ($\sim$ 180-200 Hz).

This suggests that it could be possible to monitor the water flow in frequencies much higher than the anthropogenic background noise (up to a few tens of Hz). Also, this frequency range is much higher than what was observed on the "canal latéral à la Loire" in Fig 3.10d (25 Hz) despite the similar diameter of the pipe (10 cm). New experimental measurements on several sites subject to leakage could allow verifying in which frequency range it is possible to monitor the water flow.

It might be very difficult to find an experimental site subject to early stages of internal erosion. However, it would also generate very low amplitude seismic events comparable to the background noise. Like for landslides, machine learning and/or AI methods might help detect such tiny events and build time series of the seismic activity (number of events as a function of their amplitude but also the evolution of the frequency) in relation to the geotechnical evolution of earth dams during internal erosion.

It has been shown, both in the laboratory (Planès *et al.*, 2016) and on a real site (Olivier *et al.*, 2017), that monitoring dV/V provides insight into the evolution of earth dams. Unlike landslides, there are no seismic time-series available, several months to several years long, to analyze the long-term evolution of small earth dams subject to internal erosion. Such long-term time-series could help answer some questions: are small earth dams affected by seasonal effects (*i.e.* reversible deformations)? Is it possible to detect early stages of internal erosion using changes in dV/V (*i.e.* irreversible deformation)?

4 General conclusions and perspectives

Results exposed in this manuscript attempted to answer several scientific questions and, unsurprisingly, raised several issues. First, it was shown that the lithological heterogeneity originating from the sedimentary layering and the landslide activity explains the variable deformation patterns observed at the surface. However, this does not explain how new shear surfaces develop at the rear of headscarps. Second, it was shown that several seismic parameters are precursory to rupture (for both landslides and earth dams) but at different timings, suggesting that the development and propagation of rupture is a complex phenomenon. Furthermore, the analysis of several years-long various time series (geodetical, geophysical, hydrological, meteorological, etc.) revealed the existence of reversible (elastic) deformations apparently controlled by seasonal fluctuations. However, the effect of reversible deformation on the development of damaging, up to failure, remains an open question.

In the manuscript, I exposed some perspectives for the next few years which I started to work on recently. I hereafter synthesize them. Answering the new issues identified requires notably long term observatory data (several years to several decades) such as those provided by the OMIV observatory on landslides, in which I intend to remain involved. A similar approach needs to be developed for small earth dams. The emergence of low-cost and efficient devices provides the opportunity to supplement observatory data, either by increasing the number of long-term observations with cost-effective stations or with short-duration experiments using dense arrays. One can also note the current strong development of fibre-optic Distributed Acoustic Sensing (DAS), for which earth dams are particularly suited (Mateeva *et al.*, 2013) since they are linear infrastructures. The measured parameters using fibre-optics (temperature, deformation) along with the development of seismology from DAS monitoring also makes this technique suited for the monitoring of earth dams. Seismologists from ISTerre are presently participating in the evaluation of DAS for seismological purposes and we can consider applying it to the monitoring of earth dams in the very next few years.

Concerning dense arrays, I am involved in the RESOLVE-HAR experiment with a research and advising activity that started in early 2022 and the research activity on these data will last several months to tens of months. Notably, several deliverables (e.g. 3D images of both P-waves, S-waves and Poisson's ratio) might help better understand the transition between slide and flow within landslides. Also, it will be possible to analyse the susceptibility of landslides (through, e.g., the H/V ratio) to environmental forcing: are there significant variations after rainfall? Are these variations synchronous in space and time? What is the physical meaning of such spectral variations and can this parameter be relevant to monitor landslide evolution?

Retrieving low-amplitude impulsive events from dense array experiments and long-term time series is another challenging task to detect weak signals potentially associated with the initiation of damaging. Works conducted on several landslides during the past decade(s) allowed the proposition of classification for endogenous seismic sources in landslides (Provost *et al.*, 2018), and several applications to the detection of events with a sufficient signal-to-noise ratio have

been proposed to detect landslide activity (Poli, 2017; Hibert *et al.*, 2019) from continuous time-series. However, in the case of low amplitude events that could originate from the initiation of deformation or internal erosion, their identification remains difficult with classical tools such as, e.g., template matching. The current development of Artificial Intelligence (AI) methods might help enhance time-series related to landslides or earth dams by adding coherent seismological data related to early stages of deformation.

In this general frame, I will also continue participating in the OhmPi project (Clément *et al.*, 2020), to supplement seismic monitoring (mechanical observation) with electrical monitoring such as resistivity and induced polarization (hydrological observation). This last parameter has notably shown to provide valuable complementary observations to resistivity on water infiltration and flow within landslides (Gallistl *et al.*, 2018; Revil *et al.*, 2020). The combination of seismic and electrical parameters might provide insight into the initiation and development of shear surfaces at the rear of headscarps, the development of weak zones within earth dams, and the transition between reversible and irreversible deformations.

In the future, I would also like to develop the use of combined processing of data. Electrical and seismic parameters are classically acquired together to study landslides and earth dams but are still largely processed and interpreted separately since the 2000s (among many others, Bichler *et al.*, 2004; Cardarelli *et al.*, 2014). The joint processing of these parameters increased recently using various strategies such as geostatistical regularization (Jordi *et al.*, 2018), structurally joint (Jordi *et al.*, 2019) or coupled inversion (Wiese *et al.*, 2018; Skibbe *et al.*, 2021), or petrophysical inversion (Wagner *et al.*, 2019; Mollaret *et al.*, 2020). Notably, the petrophysical inversion would provide the evaluation of physical parameters such as stiffness or saturation, which are more easily handled by the engineering community than indirect geophysical parameters.

In parallel, I am convinced that numerical modelling conducted along with field observations and experiments is a key to better apprehending the physical processes at stake during the development of damaging. I developed some skills during the past years and I will continue using this approach in the next few years, notably to better understand the propagation of seismic waves in complex media such as earth dams. This is a work I started recently and that may help to better understand why and how surface waves are so strongly affected during their propagation in such media. The mid-to-long-term objective of this research is notably to be able to propose to the engineering community a better way to process surface wave data that remain widely used on structure exhibiting morphologic shapes far from the 1D hypothesis (such as earth dams) with few to no hindsight.

5 Bibliographic references

Al Hayari M, Antoine P, Biguenet G, Monnet J & Mora H (1990). Détermination des caractéristiques mécaniques au cisaillement des argiles litées. Cas du glissement de la combe d'Harmalière. *Revue Française de Géotechnique*. **50** : 71–77.

Aleotti P (2004). A warning system for rainfall-induced shallow failures. *Engineering Geology*. **73** : 247–265.

Ancey C (2007). Plasticity and geophysical flows : A review. *Journal of Non-Newtonian Fluid Mechanics*. **142**(1-3) : 4–35. doi: 10.1016/j.jnnfm.2006.05.005.

Antoine P, Giraud A & Montjuvent G (1981). Les argiles litées du Trièves (Isère) ; conditions de gisement et exemples de propriétés géotechniques. *Bulletin de la Société Géologique de France*. **7, XXIII**(2) : 117–127.

Archie GE (1942). The electrical resistivity log as an aid in determining some reservoir characteristics. *Transactions AIME*. **146** : 54–62.

Arosio D, Longoni L, Papini M, Bièvre G & Zanzi L (2019). Geological and geophysical investigations to analyse a lateral spreading phenomenon : the case study of Torrioni di Rialba, northern Italy. *Landslides*. **16**(7) : 1257–1271. doi: 10.1007/s10346-019-01176-w.

Bartetzko A & Kopf AJ (2007). The relationship of undrained shear strength and porosity with depth in shallow (< 50 m) marine sediments. *Sedimentary Geology*. **196**(1) : 235–249. doi: 10.1016/j.sedgeo.2006.04.005.

Berti M, Bertello L & Squarzoni G (2018). Surface-wave velocity measurements of shear stiffness of moving earthflows. *Landslides*. **16**(3) : 469–484. doi: 10.1007/s10346-018-1102-1.

Berti M, Castellaro S & Zuccarini A (2022). Field measurements, laboratory tests and empirical relations for investigating the solid-to-fluid transition of a rapid earthflow. *Engineering Geology*. **296** : 106486. doi: https://doi.org/10.1016/j.enggeo.2021.106486.

Bichler A, Bobrowsky P, Best M, Douma M, Hunter J, Calvert T & Burns R (2004). Three-dimensional mapping of a landslide using a multi-geophysical approach : the Quesnel Forks landslide. *Landslides*. **01** : 29–40.

Bièvre G (2007a). Élaboration d'un modèle géologique de structure anticlinale complexe : contribution aux études géotechniques d'un tracé routier et de ses ouvrages d'art (voie des Mercureaux, Besançon, Est de la France). *Bulletin des Laboratoires des Ponts et Chaussées*. **267** : 1–16.

Bièvre G (2007b). *Méthodes géophysiques pour la reconnaissance des digues des voies navigables*. Collection Les Repères. CETMEF Éditions, Compiègne, France. 82 pp.

Bièvre G & Crouzet C (2021). Multi-proxy analysis of boreholes in remolded Quaternary paraglacial deposits (Avignonet landslide, French Western Alps). *Engineering Geology*. **286** : 106073. doi: 10.1016/j.enggeo.2021.106073.

Bièvre G, Franz M, Larose E, Jongmans D, Jaboyedoff M & Carrière S (2018a). Influence of environmental parameters on seismic velocity variations in a clayey mudflow (Pont-Bourquin, Switzerland). *Engineering Geology*. **245** : 248–257. doi: 10.1016/j.enggeo.2018.08.013. Special issue : Characterizing and monitoring landslide processes using remote sensing and geophysics.

Bièvre G, Garambois S & Pondaven I (in prep). Localization of a small abandoned municipal solid waste landfill combining remote sensing and geophysics.

Bièvre G, Jongmans D, Goutaland D, Pathier E & Zumbo V (2016). Geophysical characterization of the lithological control on the kinematic pattern in a large clayey landslide (Avignonet, French Alps). *Landslides*. **13**(3) : 423–436. doi: 10.1007/s10346-015-0579-0.

Bièvre G, Jongmans D, Lebourg T & Carrière S (2021). Electrical resistivity monitoring of an earthslide with electrodes located outside the unstable zone (Pont-Bourquin landslide, Swiss Alps). *Near Surface Geophysics*. **19** : 225–239. doi: 10.1002/nsg.12145. Special issue : Near-surface geophysics for geohazard assessment.

Bièvre G, Jongmans D, Winiarski T & Zumbo V (2012). Application of geophysical measurements for assessing the role of fissures in water infiltration within a clay landslide (Trièves area, French Alps). *Hydrological Processes*. **26**(14) : 2128–2142. doi: 10.1002/hyp.7986.

Bièvre G, Joseph A & Bertrand C (2018b). Preferential water infiltration paths in a clayey earthslide evidenced by cross-correlation of hydrometeorological time series (Charlaix, French Western Alps). *Geofluids*. **2018**(9593267) : 20. doi: 10.1155/2018/9593267. Special issue : The role and impact of geofluids in geohazards.

Bièvre G, Knieß U, Jongmans D, Pathier E, Schwartz S, van Westen CJ, Villemin T & Zumbo V (2011). Paleotopographic control of landslides in lacustrine deposits (Trièves plateau, French western Alps). *Geomorphology*. **125**(1) : 214–224. doi: 10.1016/j.geomorph.2010.09.018.

Bièvre G, Lacroix P, Oxarango L, Goutaland D, Monnot G & Fargier Y (2017). Integration of geotechnical and geophysical techniques for the characterization of a small earth-filled canal dyke and the localization of water leakage. *Journal of Applied Geophysics*. **139** : 1–15. doi: 10.1016/j.jappgeo.2017.02.002.

Bièvre G & Norgeot C (2005). Utilisation des méthodes géophysiques pour l'auscultation des digues en eau : étude de cas sur le canal du Centre (France). *Bulletin des Laboratoires des Ponts et Chaussées*. **254** : 85–107.

Bièvre G, Oxarango L, Günther T, Goutaland D & Massardi M (2018c). Improvement of 2D ERT measurements conducted along a small earth-filled dyke using 3D topographic data and 3D computation of geometric factors. *Journal of Applied Geophysics*. **153** : 100–112. doi: 10.1016/j.jappgeo.2018.04.012.

Blanchet F (1988). *Étude géomécanique de glissements de terrain dans les argiles glaciolacustres de la vallée du Drac*. Phd thesis. Université Joseph Fourier, Grenoble, France.

Bogoslovsky VA & Ogilvy AA (1970a). Applications of geophysical methods for studying the technical status of earth dams. *Geophysical Prospecting*. **18** : 758–773.

Bogoslovsky VA & Ogilvy AA (1970b). Natural potential anomalies as a quantitative index of the rate of seepage from water reservoirs. *Geophysical Prospecting*. **18** : 261–268.

Bogoslovsky VA & Ogilvy AA (1973). Application of geophysical methods to investigation of landslides. *Geophysics*. **38**(6) : 1191–1192.

Bogoslovsky VA & Ogilvy AA (1977). Geophysical methods for the investigation of landslides. *Geophysics*. **42** : 562–571. doi: 10.1190/1.1440727.

Bolève A, Vandemeulebrouck J & Grangeon J (2012). Dyke leakage localization and hydraulic permeability estimation through self-potential and hydro-acoustic measurements : Self-potential 'abacus' diagram for hydraulic permeability estimation and uncertainty computation. *Journal of Applied Geophysics*. **86** : 17 – 28. doi: 10.1016/j.jappgeo.2012.07.007.

Brooke JP (1973). Geophysical investigations of a landslide near San Jose, California. *Geoexploration*. **11** : 61–73. doi: 10.1016/0016-7142(73)90049-5.

Cardarelli E, Cercato M & De Donno G (2014). Characterization of an earth-filled dam through the combined use of electrical resistivity tomography, P- and SH-wave seismic tomography and surface wave data. *Journal of Applied Geophysics*. **106** : 87–95. doi: 10.1016/j.jappgeo.2014.04.007.

Cardarelli E, Cercato M & Filippo G (2010). Geophysical investigation for the rehabilitation of a flood control embankment. *Near Surface Geophysics*. **8** : 287–296. doi: 10.3997/1873-0604.2010018.

Caris JPT & Van Asch TWJ (1991). Geophysical, geotechnical and hydrogeological investigations of a small landslide in the French Alps. *Engineering Geology*. **31** : 249–276.

Carrière S (2016). *Recherche de précurseurs géophysiques à la transition solide-fluide dans les glissements-coulées affectant les matériaux argileux*. Phd thesis. Université Grenoble-Alpes.

Carrière S, Bièvre G, Jongmans D, Chambon G, Bellot H & Lebourg T (2018a). Measurement of geophysical parameters on clay samples at the solid-fluid transition. *Near Surface Geophysics*. **16**(1) : 1–15. doi: 10.3997/1873-0604.2017039.

Carrière S, Jongmans D, Chambon G, Bièvre G, Lanson B, Bertello L, Berti M, Jaboyedoff M, Malet JP & Chambers J (2018b). Rheological properties of clayey soils originating from flow-like landslides. *Landslides*. **15**(8) : 1615–1630. doi: 10.1007/s10346-018-0972-6.

Chambers J, Wilkinson P, Kuras O, Ford JR, Gunn DA, Meldrum P, Pennington CVL, Weller AL, Hobbs PRN & Ogilvy RD (2011). Three-dimensional geophysical anatomy of an active landslide in Lias Group mudrocks, Cleveland basin, UK. *Geomorphology*. **125** : 472–484. doi: 10.1016/j.geomorph.2010.09.017.

Chambers JE, Gunn DA, Wilkinson PB, Meldrum PI, Haslam E, Holyoake S, Kirkham M, Kuras O, Merritt A & Wragg J (2014). 4D electrical resistivity tomography monitoring of soil moisture dynamics in an operational railway embankment. *Near Surface Geophysics*. **12**(1) : 61–72. doi: 10.3997/1873-0604.2013002.

Cho IK, Ha IS, Kim KS, Ahn HY, Lee S & Kang HJ (2014). 3D effects on 2D resistivity monitoring in earth-fill dams. *Near Surface Geophysics*. **12** : 73–81. doi: 10.3997/1873-0604.2013065.

Cho IK & Yeom JY (2007). Crossline resistivity tomography for the delineation of anomalous seepage pathways in an embankment dam. *Geophysics*. **72**(2) : G31–G38. doi: 10.1190/1.2435200.

Clément R, Fargier Y, Dubois V, Gance J, Gros E & Forquet N (2020). OhmPi : An open source data logger for dedicated applications of electrical resistivity imaging at the small and laboratory scale. *HardwareX*. p. e00122. doi: 10.1016/j.ohx.2020.e00122.

Clément R & Moreau S (2016). How should an electrical resistivity tomography laboratory test cell be designed ? numerical investigation of error on electrical resistivity measurement. *Journal of Applied Geophysics*. **127** : 45–55. doi: 10.1016/j.jappgeo.2016.02.008.

Coe JA, Ellis WL, Godt JW, Savage WZ, Savage JE, Michael JA, Kibler JD, Powers PS, Lidke DJ & Debray S (2003). Seasonal movement of the Slumgullion landslide determined from Global Positioning System surveys and field instrumentation, July 1998-March 2002. *Engineering Geology*. **68**(1-2) : 67–101. doi: 10.1016/S0013-7952(02)00199-0.

Coe JA, McKenna JP, Godt JW & Baum RL (2009). Basal-topographic control of stationary ponds on a continuously moving landslide. *Earth Surface Processes and Landforms*. **34**(2) : 264–279. doi: 10.1002/esp.1721.

Colombero C, Fiolleau S, Jongmans D, Valentin J, Baillet L, Larose E & Bièvre G (2021). Seismic noise parameters as indicators of reversible modifications in slope stability : a review. *Surveys in Geophysics*. **42** : 339–375. doi: 10.1007/s10712-021-09632-w.

Corsini A, Pasuto A, Soldati M & Zannoni A (2005). Field monitoring of the Corvara landslide (Dolomites, Italy) and its relevance for hazard assessment. *Geomorphology*. **66**(1-4) : 149–165. doi: 10.1016/j.geomorph.2004.09.012.

Coussot P & Ancey C (1999). Rheophysical classification of concentrated suspensions and granular pastes. *Physical Review E*. **59**(4) : 4445–4457. doi: 10.1103/PhysRevE.59.4445.

Coutterand S (2010). *Étude géomorphologique des flux glaciaires dans les Alpes nord-occidentales au Pléistocène récent : du maximum de la dernière glaciation aux premières étapes de la déglaciation*. Ph.D. thesis. Université de Savoie, France.

Crawford MM & Bryson LS (2018). Assessment of active landslides using field electrical measurements. *Engineering Geology*. **233** : 146–159. doi: 10.1016/j.enggeo.2017.11.012.

Dion R (1961). *Histoire des levées de la Loire*. CNRS Éditions, Paris, France.

Dumont G, Robert T, Marck N & Nguyen F (2017). Assessment of multiple geophysical techniques for the characterization of municipal waste deposit sites. *Journal of Applied Geophysics*. **145** : 74–83. doi: 10.1016/j.jappgeo.2017.07.013.

Evin J, Marechal J & Marien G (1985). Lyon Natural Radiocarbon Measurements X. *Radiocarbon*. **27**(2B) : 386–454. doi: 10.1017/S003382220000713X.

Fargier Y, Ananfouet Y, Palma-Lopes S, Saussaye L, Dore L, Jodry C, Fauchard C & Bièvre G (2019). Quality assessment of a cut-off wall dike reinforcement by 2D-ERI. *Journal of Environmental & Engineering Geophysics*. **24**(3) : 451–463. doi: 10.2113/JEEG24.3.451.

Fargier Y, Palma Lopes S, Fauchard C, Francois D & Côte P (2014). DC-Electrical Resistivity Imaging for embankment dike investigation : a 3D extended normalisation approach. *Journal of Applied Geophysics*. **103** : 245–256. doi: 10.1016/j.jappgeo.2014.02.007.

Fauchard C & Mériaux P (2007). *Geophysical and geotechnical methods for diagnosing flood protection dikes*. Éditions Quae, Paris, France.

Fell R, MacGregor P, Stapledon D, Bell G & Foster M (2015). *Geotechnical engineering of dams*. CRC Press/Balkema. second edn.

Fell R, Wan CF, Cyganiewicz J & Foster M (2003). Time for development of internal erosion and piping in embankment dams. *Journal of Geotechnical & Geoenvironmental Engineering*. **129**(4) : 307–314. doi: 10.1061/(ASCE)1090-0241(2003)129:4(307).

Fiolleau S (2020). *Étude des mécanismes de déformation et d'évolution d'un glissement-coulée - approche couplée géophysique-mécanique*. Ph.D. thesis. Université Grenoble Alpes.

Fiolleau S, Jongmans D, Bièvre G, Chambon G, Baillet L & Vial B (2020). Seismic characterization of a clay-block rupture in Harmalière landslide, French Western Alps. *Geophysical Journal International*. **221**(3) : 1777–1788. doi: 10.1093/gji/ggaa050.

Fiolleau S, Jongmans D, Bièvre G, Chambon G, Lacroix P, Helmstetter A, Wathelet M & Demierre M (2021). Multi-method investigation of mass transfer mechanisms in a retrogressive clayey landslide (Harmalière, French Alps). *Landslides*. **18** : 1981–2000. doi: 10.1007/s10346-021-01639-z.

Foster M, Fell R & Spannagle M (2000). The statistics of embankment dam failures and accidents. *Canadian Geotechnical Journal*. **37**(5) : 1000–1024. doi: 10.1139/t00-030.

Foti S, Hollender F, Garofalo F, Albarello D, Asten M, Bard PY, Comina C, Cornou C, Cox B, Di Giulio G, Forbriger T, Hayashi K, Lunedei E, Martin A, Mercerat D, Ohrnberger M, Poggi V, Renalier F, Sicilia D & Socco V (2018). Guidelines for the good practice of surface wave analysis : a product of the InterPACIFIC project. *Bulletin of Earthquake Engineering*. **16**(6) : 2367–2420. doi: 10.1007/s10518-017-0206-7.

Fox RC, Hohmann GW, Killpack TJ & Rijo L (1980). Topographic effects in resistivity and induced-polarization surveys. *Geophysics*. **45**(1) : 75–93. doi: 10.1190/1.1441041.

Gallistl J, Weigand M, Stumvoll M, Ottowitz D, Glade T & Flores Orozco A (2018). Delineation of subsurface variability in clay-rich landslides through spectral induced polarization imaging and electromagnetic methods. *Engineering Geology*. **245** : 292–308. doi: 10.1016/j.enggeo.2018.09.001.

Giraud A, Antoine P, Van Asch TWJ & Nieuwenhuis JD (1991). Geotechnical problems caused by glaciolacustrine clays in the French Alps. *Engineering Geology*. **31** : 185–195. doi: 10.1016/0013-7952(91)90005-6.

Giraud A, Gourc JP, Besson L & Fabre D (1981). Approche pluridisciplinaire des problèmes posés par un glissement de terrain sur faible pente. *Revue Française de Géotechnique*. **14** : 57–66.

Gradon C, Roux P, Moreau L, Lecointre A & Zion YB (2021). Characterization with dense array data of seismic sources in the shallow part of the san jacinto fault zone. *Geophysical Journal International*. **224**(2) : 1133–1140. doi: 10.1093/gji/ggaa411.

Graham WJ (1999). A procedure for estimating loss of life caused by dam failures. techreport DSO-99-06. Unite States Bureau of Reclamation, Washington DC, USA.

Guerriero L, Coe JA, Revellino P, Grelle G, Pinto F & Guadagno FM (2014). Influence of slip-surface geometry on earth-flow deformation, Montaguto earth flow, southern Italy. *Geomorphology*. **219** : 285–305. doi: 10.1016/j.geomorph.2014.04.039.

Handwerger AL, Roering JJ & Schmidt DA (2013). Controls on the seasonal deformation of slow-moving landslides. *Earth and Planetary Science Letters*. **377-378** : 239–247. doi: 10.1016/j.epsl.2013.06.047.

Helmstetter A & Garambois S (2010). Seismic monitoring of Séchilienne rockslide (French Alps) : Analysis of seismic signals and their correlation with rainfalls. *Journal of Geophysical Research*. **115** : F03016. doi: 10.1029/2009JF001532.

Hennig T, Weller A & Canh T (2005). The effect of dike geometry on different resistivity configurations. *Journal of Applied Geophysics*. **57**(4) : 278–292. doi: 10.1016/j.jappgeo.2005.03.001.

Hibert C, Michéa D, Provost F, Malet JP & Geertsema M (2019). Exploration of continuous seismic recordings with a machine learning approach to document 20 yr of landslide activity in Alaska. *Geophysical Journal International*. **219**(2) : 1138–1147. doi: 10.1093/gji/ggz354.

Hilloulin B, Zhang Y, Abraham O, Loukili A, Grondin F, Durand O & Tournat V (2014). Small crack detection in cementitious materials using nonlinear coda wave modulation. *NDT & E International*. **68** : 98–104. doi: 10.1016/j.ndteint.2014.08.010.

Hungr O, Leroueil S & Picarelli L (2014). The Varnes classification of landslide types, an update. *Landslides*. **11**(2) : 167–194. doi: 10.1007/s10346-013-0436-y.

ICOLD (2017). Internal erosion of existing dams, levees and dikes, and their foundations. in : *ICOLD Bulletin*. vol. 164 of *ICOLD Bulletin*. p. 342. International Commission on Large Dams, ICOLD, Paris, France.

Ikard S, Rittgers J, Revil A & Mooney M (2015). Geophysical investigation of seepage beneath an earthen dam. *Groundwater*. **53**(2) : 238–250. doi: 10.1111/gwat.12185.

Iverson R & Major J (1987). Rainfall, groundwater-flow, and seasonal movement at minor creek landslide, northwestern california - physical interpretation of empirical relations. *Geological Society of America Bulletin*. **99** : 579–594. doi: 10.1130/0016-7606(1987)99⟨579:RGFASM⟩2.0.CO;2.

Iverson RM (2005). Regulation of landslide motion by dilatancy and pore pressure feedback. *Journal of Geophysical Research : Earth Surface*. **110**(F2) : F02015. doi: 10.1029/2004JF000268.

Iverson RM & George DL (2016). Modelling landslide liquefaction, mobility bifurcation and the dynamics of the 2014 oso disaster. *Géotechnique*. **66**(3) : 175–187. doi: 10.1680/jgeot.15.LM.004.

Jaboyedoff M, Demers D, Locat J, Locat A, Locat P, Oppikofer T, Robitaille D & Turmel D (2009). Use of terrestrial laser scanning for the characterization of retrogressive landslides in sensitive clay and rotational landslides in river banks. *Canadian Geotechnical Journal*. **46**(12) : 1379–1390.

Jongmans D, Bièvre G, Schwartz S, Renalier F & Beaurez N (2009). Geophysical investigation of the large Avignonet landslide in glaciolacustrine clays in the Trièves area (French Alps). *Engineering Geology*. **109** : 45–56. doi: 10.1016/j.enggeo.2008.10.005.

Jongmans D, Fiolleau S, Bièvre G, Chambon G & Dano C (in prep.). Gravitational movements in the stiff clays of the Sinard plateau (western Alps) : monitoring, kinematics and rheology. *Engineering Geology*.

Jongmans D & Garambois S (2007). Geophysical investigation of landslides : a review. *Bulletin de la Société Géologique de France*. **178**(2) : 101–112. doi: 10.2113/gssgfbull.178.2.101.

Jordi C, Doetsch J, Günther T, Schmelzbach C, Maurer H & Robertsson JOA (2019). Structural joint inversion on irregular meshes. *Geophysical Journal International*. **220**(3) : 1995–2008. doi: 10.1093/gji/ggz550.

Jordi C, Doetsch J, Günther T, Schmelzbach C & Robertsson JOA (2018). Geostatistical regularization operators for geophysical inverse problems on irregular meshes. *Geophysical Journal International*. **213**(2) : 1374–1386. doi: 10.1093/gji/ggy055.

Jorry SJ & Bièvre G (2011). Integration of sedimentology and ground-penetrating radar for high-resolution imaging of a carbonate platform. *Sedimentology*. **58**(6) : 1370–1390. doi: 10.1111/j.1365-3091.2010.01213.x.

Karl L, Fechner T, Schevenels M, Francois S & Degrande G (2011). Geotechnical characterization of a river dyke by surface waves. *Near Surface Geophysics*. **9** : 515–527.

Keefer DK & Johnson AM (1983). Earth flows ; morphology, mobilization, and movement. Tech. Rep. 1264. USGS Publications Warehouse, USA. doi: 10.3133/pp1264. `http://pubs.er.usgs.gov/publication/pp1264`.

Keefer DK, Wilson RC, Mark RK, Brabb EE, Brown I W M, Ellen SD, Harp EL, Wieczorek GF, Alger CS & Zatkin RS (1987). Real-time landslide warning during heavy rainfall. *Science*. **238**(4829) : 921–925. doi: 10.1126/science.238.4829.921.

Kim JH, Yi MJ, Song Y, Jee Seol S & Kim KS (2007). Application of geophysical methods to the safety analysis of an earth dam. *Journal of Environmental & Engineering Geophysics*. **12**(2) : 221–235. doi: 10.2113/JEEG12.2.221.

Knieß U, Travelletti J, Daehne A, Krzeminska D, Bièvre G, Jongmans D, Corsini A, Bogaard T & Malet JP (2014). Innovative techniques for the characterization of the morphology, geometry and hydrological features of slow-moving landslides. in : Van Asch TJW, Corominas J, Greiving S, Malet JP & Sterlacchini S (Eds.), *Mountain Risks : From Prediction to Management and Governance*. vol. 34 of *Advances in Natural and Technological Hazards Research*. pp. 57–82. Springer, Netherlands. doi: 10.1007/978-94-007-6769-0$_3$.

Koerner RM, McCabe WM & Baldivieso LF (1981). Acoustic emission monitoring of seepage. *Journal of the Geotechnical Engineering Division*. **107**(4) : 521–526. doi: 10.1061/ajgeb6.0001414.

Krøgli IK, Devoli G, Colleuille H, Boje S, Sund M & Engen IK (2018). The norwegian forecasting and warning service for rainfall- and snowmelt-induced landslides. *Natural Hazards and Earth System Sciences*. **18**(5) : 1427–1450. doi: 10.5194/nhess-18-1427-2018.

Krzeminska DM, Bogaard TA, Debieche TH, Marc V, Ponton J & Malet JP (2009). Quantitative analysis of preferential flow during small scale infiltration tests on an active mudslide, Super-Sauze, South French Alps. in : *Proceedings of the International Conference "Landslide processes : from geomorphologic mapping to dynamic modelling", february 2009, Strasbourg, France*.

Lacroix P, Bièvre G, Pathier E, Knieß U & Jongmans D (2018). Use of Sentinel-2 images for the detection of precursory motions before landslide ruptures. *Remote Sensing of Environment*. **215** : 507–516. doi: 10.1016/j.rse.2018.03.042.

Lacroix P, Dehecq A & Taipe E (2020a). Irrigation-triggered landslides in a Peruvian desert caused by modern intensive farming. *Nature Geoscience*. **13**(1) : 1–5. doi: 10.1038/s41561-019-0500-x.

Lacroix P, Handwerger AL & Bièvre G (2020b). Life and death of slow-moving landslides. *Nature Reviews Earth & Environment*. **1** : 404–419. doi: 10.1038/s43017-020-0072-8.

Lacroix P & Helmstetter A (2011). Location of seismic signals associated with microearthquakes and rockfalls on the séchilienne landslide, french alps. *Bulletin of the Seismological Society of America*. **101**(1) : 341–353. doi: 10.1785/0120100110.

Lajaunie M, Gance J, Nevers P, Malet JP, Bertrand C, Garin T & Ferhat G (2019). Structure of the Séchilienne unstable slope from large-scale three-dimensional electrical tomography using a Resistivity Distributed Automated System (R-DAS). *Geophysical Journal International*. **219**(1) : 129–147. doi: 10.1093/gji/ggz259.

Lambert A & Monjuvent G (1968). Quelques vues nouvelles sur l'histoire quaternaire de la vallée du Drac (note préliminaire). *Géologie Alpine*. **44** : 117–138.

Larose E, Carrière S, Voisin C, Bottelin P, Baillet L, Guéguen P, Walter F, Jongmans D, Guillier B, Garambois S, Gimbert F & Massey C (2015a). Environmental seismology : what can we learn on earth surface processes with ambient noise ?. *Journal of Applied Geophysics*. **116** : 62–74. doi: 10.1016/j.jappgeo.2015.02.001.

Larose E, Obermann A, Digulescu A, Planès T, Chaix JF, Mazerolle F & Moreau G (2015b). Locating and characterizing a crack in concrete with diffuse ultrasound : a four-point bending test. *The Journal of the Acoustical Society of America*. **138**(1) : 232–241. doi: 10.1121/1.4922330.

Laudanski G, Reiffsteck P, Tacita JL, Desanneaux G & Benoît J (2013). Experimental study of drilling parameters using a test embankment. in : Coutinho RQ & Mayne PW (Eds.), *Geotechnical and Geophysical Site Characterization 4*. pp. 435–440. Taylor & Francis, London, England.

Le Breton M, Baillet L, Larose E, Rey E, Benech P, Jongmans D, Guyoton F & Jaboyedoff M (2019). Passive radio-frequency identification ranging, a dense and weather-robust technique for landslide displacement monitoring. *Engineering Geology*. **250** : 1–10. doi: 10.1016/j.enggeo.2018.12.027.

Le Breton M, Bontemps N, Guillemot A, Baillet L & Larose E (2021). Landslide monitoring using seismic ambient noise correlation : challenges and applications. *Earth-Science Reviews*. **216** : 103518. doi: 10.1016/j.earscirev.2021.103518.

Lofi J, Pezard P, Loggia D, Garel E, Gautier S, Merry C & Bondabou K (2012). Geological discontinuities, main flow path and chemical alteration in a marly hill prone to slope instability : Assessment from petrophysical measurements and borehole image analysis. *Hydrological Processes*. **26**(14) : 2071–2084. doi: 10.1002/hyp.7997.

Lévy C, Baillet L, Jongmans D, Mourot P & Hantz D (2010). Dynamic response of the Chamousset rock column (Western Alps, France). *Journal of Geophysical Research : Earth Surface*. **115**(F4). doi: 10.1029/2009JF001606. f04043.

Maalouf Y (2021). *Méthodes géophysiques pour la détection, le suivi temporel et la quantification d'écoulements dans les milieux poreux. Application aux digues en terre et aux réservoirs aquifères*. Ph.D. thesis. Université Grenoble Alpes.

Maalouf Y, Bièvre G, Voisin C & Khoury N (2022). Geophysical monitoring of a laboratory scale internal erosion experiment. *Near Surface Geophysics*. **20** : 365–383. doi: 10.1002/nsg.12215.

Mainsant G, Chambon G, Jongmans D, Larose E & Baillet L (2015). Shear-wave-velocity drop prior to clayey mass movement in laboratory flume experiments. *Engineering Geology*. **192** : 26–32. doi: 10.1016/j.enggeo.2015.03.019.

Mainsant G, Jongmans D, Chambon G, Larose E & Baillet L (2012a). Shear-wave velocity as an indicator for rheological changes in clay materials : Lessons from laboratory experiments. *Geophysical Research Letters*. **39** : L19301. doi: 10.1029/2012GL053159.

Mainsant G, Larose E, Brönnimann C, Jongmans D, Michoud C & Jaboyedoff M (2012b). Ambient seismic noise monitoring of a clay landslide : Toward failure prediction. *Journal of geophysical research*. **117**(F1) : F01030. doi: 10.1029/2011JF002159.

Mateeva A, Lopez J, Mestayer J, Wills P, Cox B, Kiyashchenko D, Yang Z, Berlang W, Detomo R & Grandi S (2013). Distributed acoustic sensing for reservoir monitoring with VSP. *The Leading Edge*. **32**(10) : 1278–1283. doi: 10.1190/tle32101278.1.

Meric O, Garambois S, Jongmans D, Wathelet M, Chatelain JL & Vengeon JM (2005). Application of geophysical methods for the investigation of the large gravitational mass movement of Séchilienne, France. *Canadian Geotechnical Journal*. **42** : 1105–1115.

Merritt AJ, Chambers JE, Murphy W, Wilkinson PB, West LJ, Uhlemann S, Meldrum PI & Gunn D (2018). Landslide activation behaviour illuminated by electrical resistance monitoring. *Earth Surface Processes and Landforms*. **43**(6) : 1321–1334. doi: 10.1002/esp.4316.

Minsley BJ, Burton BL, Ikard S & Powers MH (2011). Hydrogeophysical Investigations at Hidden Dam, Raymond, California. *Journal of Environmental & Engineering Geophysics*. **16**(4) : 145–164. doi: 10.2113/JEEG16.4.145.

Mollaret C, Wagner FM, Hilbich C, Scapozza C & Hauck C (2020). Petrophysical joint inversion applied to Alpine permafrost field sites to image subsurface ice, water, air, and rock contents. *Frontiers in Earth Science*. **8**. doi: 10.3389/feart.2020.00085.

Monjuvent G (1973). La transfluence Durance-Isère. Essai de synthèse du Quaternaire du bassin du Drac (Alpes françaises). *Géologie Alpine*. **49** : 57–118.

Monjuvent G (1978). *Le Drac. Morphologie, stratigraphie et chronologie quaternaires d'un bassin alpin*. Ph.D. thesis. Université Denis Diderot, Paris, France.

Niederleithinger E, Weller A & Lewis R (2012). Evaluation of geophysical techniques for dike inspection. *Journal of Environmental & Engineering Geophysics*. **17**(4) : 185–195. doi: 10.2113/JEEG17.4.185.

Nieuwenhuis JD (1991). *Variations in stability and displacements of a shallow seasonal landslide in varved clays*. Ph.D. thesis. Utrecht University, The Netherlands.

Ogilvy AA, Ayed MA & Bogoslovsky VA (1969). Geophysical studies of water leakages from reservoirs. *Geophysical Prospecting*. **17** : 36–62. doi: 10.1111/j.1365-2478.1969.tb02071.x.

Olivier G, Brenguier F, de Wit T & Lynch R (2017). Monitoring the stability of tailings dam walls with ambient seismic noise. *The Leading Edge*. **36**(4) : 350a1–350a6. doi: 10.1190/tle36040350a1.1.

Olsson PI, Dahlin T, Fiandaca G & Auken E (2015). Measuring time-domain spectral induced polarization in the on-time : decreasing acquisition time and increasing signal-to-noise ratio. *Journal of Applied Geophysics*. **123** : 316 – 321. doi: 10.1016/j.jappgeo.2015.08.009.

Petley DN, Higuchi T, Petley DJ, Bulmer MH & Carey J (2005). Development of progressive landslide failure in cohesive materials. *Geology*. **33**(3) : 201–204.

Picarelli L, Urciuoli G & Russo C (2004). Effect of groundwater regime on behaviour of clayey slopes. *Canadian Geotechnical Journal*. **41** : 467–484. doi: 10.1139/t04-009.

Planès T, Mooney MA, Rittgers JBR, Parekh ML, Behm M & Snieder R (2016). Time-lapse monitoring of internal erosion in earthen dams and levees using ambient seismic noise. *Géotechnique*. **66**(4) : 301–312. doi: 10.1680/jgeot.14.P.268.

Poisson J, Chouteau M, Aubertin M & Campos D (2009). Geophysical experiments to image the shallow internal structure and the moisture distribution of a mine waste rock pile. *Journal of Applied Geophysics*. **67**(2) : 179–192. doi: 10.1016/j.jappgeo.2008.10.011.

Poli P (2017). Creep and slip : Seismic precursors to the Nuugaatsiaq landslide (Greenland). *Geophysical Research Letters*. **44**(17) : 8832–8836. doi: 10.1002/2017GL075039.

Provost F, Hibert C & Malet JP (2017). Automatic classification of endogenous landslide seismicity using the Random Forest supervised classifier. *Geophysical Research Letters*. **44**(1) : 113–120. doi: 10.1002/2016GL070709.

Provost F, Malet JP, Hibert C, Helmstetter A, Radiguet M, Amitrano D, Langet N, Larose E, Abancó C, Hürlimann M, Lebourg T, Levy C, Le Roy G, Ulrich P, Vidal M & Vial B (2018). Towards a standard typology of endogenous landslide seismic sources. *Earth Surface Dynamics*. **6**(4) : 1059–1088. doi: 10.5194/esurf-6-1059-2018.

Renalier F, Bièvre G, Jongmans D, Campillo M & Bard PY (2010a). Characterization and monitoring of unstable clay slopes using active and passive shear wave velocity measurements. in : Miller RD, Bradford JD & Holliger K (Eds.), *Advances in near-surface seismology and ground-penetrating radar*. no. 15 in Geophysical Developments Series. pp. 397–414. Society of Exploration Geophysics, Tulsa, USA. doi: 10.1190/1.9781560802259.ch24.

Renalier F, Jongmans D, Campillo M & Bard PY (2010b). Shear wave velocity imaging of the Avignonet landslide (France) using ambient noise cross-correlation. *Journal of Geophysical Research*. **115** : F03032. doi: 10.1029/2009JF001538.

Revil A, Soueid Ahmed A, Coperey A, Ravanel L, Sharma R & Panwar N (2020). Induced polarization as a tool to characterize shallow landslides. *Journal of Hydrology*. **589** : 125369. doi: 10.1016/j.jhydrol.2020.125369.

Rittgers JB, Revil A, Planès T, Mooney MA & Koelewijn AR (2015). 4-D imaging of seepage in earthen embankments with time-lapse inversion of self-potential data constrained by acoustic emissions localization. *Geophysical Journal International*. **200**(2) : 758–772. doi: 10.1093/gji/ggu432.

Royet P, Palma-Lopes S, Fauchard C, Mériaux P & Auriau L (2013). Rapid and cost-effective dike condition assessment methods : geophysics and remote sensing. Tech. rep.. Deliverable 32, FP7-ENV-2009 FloodProBE project. `http://www.floodprobe.eu/partner/assets/documents/Floodprobe-D3.2_V1_4_April_2013.pdf`.

Rücker C, Günther T & Wagner FM (2017). pyGIMLi : An open-source library for modelling and inversion in geophysics. *Computers & Geosciences*. **109** : 106–123. doi: 10.1016/j.cageo.2017.07.011.

Schmutz M, Guérin R, Andrieux P & Maquaire O (2009). Determination of the 3D structure of an earthflow by geophysical methods : The case of Super Sauze, in the French southern Alps. *Journal of Applied Geophysics*. **68**(4) : 500–507. doi: DOI:10.1016/j.jappgeo.2008.12.004.

Seydoux L, Balestriero R, Poli P, de Hoop M, Campillo M & Baraniuk R (2020). Clustering earthquake signals and background noises in continuous seismic data with unsupervised deep learning. *Nature Communications*. **11**(1). doi: 10.1038/s41467-020-17841-x.

Sjödahl P, Dahlin T & Johansson S (2009). Embankment dam seepage evaluation from resistivity monitoring data. *Near Surface Geophysics*. **7** : 463–474. doi: 10.3997/1873-0604.2009023.

Sjödahl P, Dahlin T, Johansson S & Loke M (2008). Resistivity monitoring for leakage and internal erosion detection at Hällby embankment dam. *Journal of Applied Geophysics*. **65**(3-4) : 155–164. doi: 10.1016/j.jappgeo.2008.07.003.

Sjödahl P, Dahlin T & Zhou B (2006). 2.5D resistivity modeling of embankment dams to assess influence from geometry and material properties. *Geophysics*. **71**(3) : G107–G114. doi: 10.1190/1.2198217.

Skibbe N, Günther T & Müller-Petke M (2021). Improved hydrogeophysical imaging by structural coupling of 2D magnetic resonance and electrical resistivity tomography. *GEOPHYSICS*. **86**(5) : WB77–WB88. doi: 10.1190/geo2020-0593.1.

Socco LV & Strobbia C (2004). Surface-wave method for near-surface characterization : a tutorial. *Near Surface Geophysics*. **2** : 165–185.

Somerton WH (1959). A laboratory study of rock breakage by rotary drilling. *Petroleum Transaction, AIME*. **216** : 92–97.

van der Spek J, Bogaard T & Bakker M (2013). Characterization of groundwater dynamics in landslides in varved clays. *Hydrology and Earth System Sciences*. **10** : 295–324. doi: 10.5194/hessd-10-295-2013.

Telford WM, Geldart LP & Sheriff RE (1990). *Applied geophysics*. Cambridge University Press, Cambridge, UK. second edn.

Terzaghi K, Peck R & Gholamreza M (1996). *Soil mechanics in engineering practice*. John Wiley & Sons, New York, USA. third edn.

Thomas AM, Spica Z, Bodmer M, Schulz WH & Roering JJ (2020). Using a dense seismic array to determine structure and site effects of the Two Towers earthflow in Northern California. *Seismological Research Letters*. **91**(2A) : 913–920. doi: 10.1785/0220190206.

Travelletti J & Malet JP (2012). Characterization of the 3D geometry of flow-like landslides : a methodology based on the integration of heterogeneous multi-source data. *Engineering Geology*. **128** : 30–48. doi: 10.1016/j.enggeo.2011.05.003.

Travelletti J, Malet JP, Samyn K, Grandjean G & Jaboyedoff M (2013). Control of landslide retrogression by discontinuities : evidences by the integration of airbone- and ground-based geophysical information. *Landslides*. **10**(1) : 37–54. doi: 10.1007/s10346-011-0310-8.

Travelletti J, Sailhac P, Malet JP, Grandjean G & Ponton J (2012). Hydrological response of weathered clay-shale slopes : water infiltration monitoring with time-lapse electrical resistivity tomography. *Hydrological Processes*. **26**(14) : 2106–2119. doi: 10.1002/hyp.7983.

Udphuay S, Günther T, Everett ME, Warden RR & Briaud JL (2011). Three-dimensional resistivity tomography in extreme coastal terrain amidst dense cultural signals : application to cliff stability assessment at the historic d-day site. *Geophysical Journal International*. **185**(1) : 201–220. doi: 10.1111/j.1365-246X.2010.04915.x.

Uhlemann S, Chambers J, Wilkinson P, Maurer H, Merritt A, Meldrum P, Kuras O, Gunn D, Smith A & Dijkstra T (2017). Four-dimensional imaging of moisture dynamics during landslide reactivation. *Journal of Geophysical Research : Earth Surface*. **122**(1) : 398–418. doi: 10.1002/2016JF003983.

Uhlemann S, Wilkinson PB, Chambers JE, Maurer H, Merritt AJ, Gunn DA & Meldrum PI (2015). Interpolation of landslide movements to improve the accuracy of 4D geoelectrical monitoring. *Journal of Applied Geophysics*. **121** : 93–105. doi: 10.1016/j.jappgeo.2015.07.003.

Van Asch TWJ, Brinkhorst WH, Buist HJ & Vessem PV (1984). The development of landslides by retrogressive failure in varved clays. *Zeitschrift für Geomorphologie Supplementband*. **4** : 165–181.

Van Asch TWJ, Hendriks MR, Hessel R & Rappange FE (1996). Hydrological triggering conditions of landslides in varved clays in the French Alps. *Engineering Geology*. **42** : 239–251.

Van Asch TWJ, Malet JP & Bogaard TA (2009). The effect of groundwater fluctuations on the velocity pattern of slow-moving landslides. *Natural Hazards and Earth System Sciences*. **9**(3) : 739–749.

Van Asch TWJ, Malet JP & Van Beek LPH (2006). Influence of landslide geometry and kinematic deformation to describe the liquefaction of landslides : Some theoretical considerations. *Engineering Geology*. **88**(1-2) : 59–69. doi: 10.1016/j.enggeo.2006.08.002.

Van Beek VM, Bezuijen A & Sellmeijer H (2013). Backward erosion piping. in : Bonelli S & Nicot F (Eds.), *Erosion in geomechanics applied to dams and levees*. chap. 3, pp. 193–269. John Wiley & Sons. doi: 10.1002/9781118577165.ch3.

Van Genuchten PMB (1989). On the temporal and spatial variance in displacement velocity of a slide in varved clays in the French Alps. *Earth surface processes and landforms*. **14** : 565–576.

Vella MA, Bièvre G, Delaere C, Thiesson J, Guérin R, Heredia C & Guédron S (in prep). The hydraulic network of the pre-Inca city of Tiwanaku (Bolivia) : relating canal morphology with hydrogeological and paleoenvironmental change.

Voisin C, Garambois S, Massey C & Brossier R (2016). Seismic noise monitoring of the water table in a deep-seated, slow-moving landslide. *Interpretation*. **4**(3) : SJ67–SJ76. doi: 10.1190/INT-2016-0010.1.

Vuillermet E (1990). *Caractéristiques géotechniques des argiles glacio-lacustres du Trièves*. Phd thesis. Université Joseph Fourier, Grenoble, France.

Vuillermet E, Cordary D & Giraud A (1994). Caractéristiques hydrauliques des argiles litées du Trièves (Isère). *Bulletin of the International Association of Engineering Geology*. **49** : 85–90.

Wagner FM, Mollaret C, Günther T, Kemna A & Hauck C (2019). Quantitative imaging of water, ice and air in permafrost systems through petrophysical joint inversion of seismic refraction and electrical resistivity data. *Geophysical Journal International*. **219**(3) : 1866–1875. doi: 10.1093/gji/ggz402.

Waxman MH & Smits LJM (1968). Electrical conductivities in oil-bearing shaly sands. *Society of Petroleum Engineering Journal*. **8** : 107–122.

Weller A, Canh T, Breede K & Vu NT (2006). Multi-electrode measurements at Thai Binh dikes (Vietnam). *Near Surface Geophysics*. **4**(2) : 135–143. doi: 10.3997/1873-0604.2005039.

Weller A, Lewis R, Canh T, Möller M & Scholz B (2014). Geotechnical and Geophysical Long-term Monitoring at a Levee of Red River in Vietnam. *Journal of Environmental & Engineering Geophysics*. **19**(3) : 183–192. doi: 10.2113/JEEG19.3.183.

Wenner M, Hibert C, van Herwijnen A, Meier L & Walter F (2021). Near-real-time automated classification of seismic signals of slope failures with continuous random forests. *Natural Hazards and Earth System Sciences*. **21**(1) : 339–361. doi: 10.5194/nhess-21-339-2021.

Whiteley JS, Chambers JE, Uhlemann S, Boyd J, Cimpoiasu MO, Holmes JL, Inauen CM, Watlet A, Hawley-Sibbett LR, Sujitapan C, Swift RT & Kendall JM (2020). Landslide monitoring using seismic refraction tomography – The importance of incorporating topographic variations. *Engineering Geology*. **268** : 105525. doi: 10.1016/j.enggeo.2020.105525.

Whiteley JS, Chambers JE, Uhlemann S, Wilkinson PB & Kendall JM (2019). Geophysical monitoring of moisture-induced landslides : A review. *Reviews of Geophysics*. **57**(1) : 106–145. doi: 10.1029/2018RG000603.

Wiese BU, Wagner FM, Norden B, Maurer H & Schmidt-Hattenberger C (2018). Fully coupled inversion on a multi-physical reservoir model – part i : Theory and concept. *International Journal of Greenhouse Gas Control*. **75** : 262–272. doi: 10.1016/j.ijggc.2018.05.013.

Wilkinson P, Meldrum P, Kuras O, Chambers J, Holyoake S & Ogilvy R (2010). High-resolution electrical resistivity tomography monitoring of a tracer test in a confined aquifer. *Journal of Applied Geophysics*. **70**(4) : 268–276. doi: 10.1016/j.jappgeo.2009.08.001.

Wilkinson PB, Uhlemann S, Chambers JE, Meldrum PI & Loke MH (2015). Development and testing of displacement inversion to track electrode movements on 3-D electrical resistivity tomography monitoring grids. *Geophysical Journal International*. **200**(3) : 1566–1581. doi: 10.1093/gji/ggu483.

Yeh TCJ, Liu S, Glass RJ, Baker K, Brainard JR, Alumbaugh D & LaBrecque D (2002). A geostatistically based inverse model for electrical resistivity surveys and its applications to vadose zone hydrology. *Water Resources Research*. **38**(12) : 1278. doi: 10.1029/2001WR001204.

Zhou C, Yin K, Cao Y & Ahmed B (2016). Application of time series analysis and PSO–SVM model in predicting the Bazimen landslide in the Three Gorges Reservoir, China. *Engineering Geology*. **204** : 108–120. doi: 10.1016/j.enggeo.2016.02.009.